UNIVERSITY OF OKLAHOMAGRADUATE COLLEGE

# NANOSCALE MINERAL CHEMISTRY AT A MODERN EUXINIC SPRING AND ITS IMPACT ON TRACE METAL MOBILITY

A DISSERTATION

SUBMITTED TO THE GRADUATE FACULTY

in partial fulfillment of the requirements for the

Degree of

DOCTOR OF PHILOSPOHY

By

ITUNU TEMIDAYO APALARA

Norman, Oklahoma

2025

NANOSCALE MINERAL CHEMISTRY AT A MODERN EUXINIC SPRING AND ITS IMPACT ON TRACE METAL MOBILITY

A DISSERTATION APPROVED FOR THE

SCHOOL OF GEOSCIENCES

BY THE COMMITTEE CONSISTING OF

Dr. Andrew S. Elwood Madden, Chair

Dr. Megan E. Elwood Madden

Dr. Caitlin Hodges

Dr. Elizabeth Butler

# Table of Contents

## Acknowledgement

I would like to appreciate the almighty God who gave me life and supplied strength throughout this academic journey. Surely a single tree does not make a forest. I have immense gratitude to my advisor, Dr. Andy Elwood Madden for giving me the opportunity, mentoring me and seeing to it at every opportunity that I do good science. I also want to thank Dr. Megan Elwood Madden for her unwavering support, advise and feedback all the time. I would also like to say thank you to Dr. Caitlin Hodges for her support, unrestricted access to her laboratory and help with some aspects of the fieldwork in this project. And to Dr. Butler, thank you for your support and understanding.

I want to specially thank Dr. Preston Larson and Dr. Julian Sabisch for their help and the trainings they gave me on microscopy instruments. A special thanks also to the OU support staff, particularly Rebecca Fay, Ginger Leivas, Moser Leah and Steve Holloway for always been available to help and answer my many questions.

To my colleagues, Katherine Sluder, Tiffany Leg, Kaydra Babre and Dani Storms, thank you for the plenty hugs that always come at the much-needed times, and most importantly scientific discussions and feedback on research, I am grateful for the gift of friendship. I am also grateful to my local church family, RCCG Praise center, Norman, the student body; Redeem On Campus (ROC), my awesome choir group, the support from you all cannot be over emphasized, I am grateful for the gift of community away from home.

My special appreciation goes to my mom; Mrs. Lola Apalara, my siblings; Bolu Apalara, Paul Apalara, Bolade Apalara, Grace Apalara and Silas Apalara, thank you all for all your sacrifices, prayers and encouragements. To my late Dad, Late Pastor T. O Apalara, I really appreciate how you loved me and sacrificed so much for me. In life, some pains never heal but we develop a

mechanism of living with them, your death is one of those pains but even in death I honor you and your legacy.

My sincere appreciation goes to all my in-laws for their support, and friends who kept encouraging me; Adebola Kolade, Akposibruke Busola, Sandra Abogunrin, Itunu Ajayi, thank you all.

And most importantly, I would like to appreciate my husband; Olawale Alo and my daughter; Toluwanimi Alo. Thank you both for been a strong pillar of support, for praying for me and with me, for uncountable sacrifices and patience with me at moments when I get cranky. Thank you for being the reason I keep staying strong at those times when I felt tired.

**Financial support statement:** The initial field work of this study was funded by Lewis and Clark astrobiology fund. This study was funded by the Joe and Robert Klabzuba Chair and additional support from NASA grant 22-HW22_2-0005.

## Dissertation Abstract

Euxinic environments, defined by the absence of oxygen and the presence of elevated concentration of sulfide ($H_2S$), are some of the most extreme yet ecologically significant habitats on Earth. These systems occur in diverse settings, from the depths of the Black Sea to some hydrothermal environments. Their study provides critical insights into solid and aqueous phase mineral biogeochemical cycling on early Earth, and even the potential for life on extra-terrestrial bodies such as Mars[1–7].

In marine systems, restricted oxygen availability coupled with high organic input leads to microbial sulfate reduction. This is a process where sulfate-reducing bacteria (SRB) convert sulfate into sulfide[8–10], leading to the formation of euxinic environments such as the permanently stratified Black Sea. The sharp transition from oxygenated surface waters to sulfidic and anoxic conditions at depth creates a unique ecosystem where anaerobic microorganisms dominate[11]. Similarly, hydrothermal vents produce sulfide-rich fluids that sustain chemosynthetic communities, that rely on symbiotic sulfur-oxidizing bacteria[12]. Also, terrestrial habitats where sulfide migrates upward from buried hydrocarbon rich formations can generate euxinic conditions when sulfide mixes with groundwater in the subsurface[13]. This study specifically explores nanoscale mineral chemistry at Zodletone spring, one such modern terrestrial environment with an oxic-euxinic interface.

One of the importance of modern euxinic environments is that they serve as windows into the early Earth. Before the Great Oxidation Event (~2.4 billion years ago), most especially early Proterozoic, euxinic conditions dominated the earth's oceans and lasted for about 1 Ga[14,15]. These early oceans hosted microbial communities similar to those found in modern analogs such as the black sea and the Cariaco basin[16]. Modern euxinic systems are natural laboratories that broadens

our understanding of ancient biogeochemical processes, habitability on Mars, the evolution of early life, metal mobility and mineral reactivity under these extreme conditions.

Mineral reactivity is one of the driving forces of geochemical processes in euxinic environments. Apart from bulk minerals, another major contributor to the geochemical processes in euxinic environments are nanoparticles. Nanoparticles and mineral phases at the nanoscale (1–100 nm) exhibit properties that differ markedly from their bulk counterparts, including increased surface area, enhanced reactivity, and unique electronic configurations[17]. In euxinic environments, such nanoscale minerals play a pivotal role in controlling the speciation and mobility of iron, sulfur, and metals. Smectite clays falls into the category of such nanoscale minerals that are important for controlling the fate of metals in the environment.

Smectite clays play critical roles in regulating elemental cycling, contaminant mobility, and geochemical processes in subsurface environment[18]. Their reactivity under anoxic, sulfidic conditions is of particular importance for understanding natural biogeochemical cycles in reducing environments such as marine sediments and euxinic basins[19]. Although many studies explored the reactivity of clays with sulfide in laboratory environments, few have directly investigated the evolution of clay mineral chemistry as a function of exposure to sulfide-rich waters in low-temperature field environments.

Therefore, this dissertation investigates mineral reactivity in a modern euxinic spring system from bulk to nanoscale level. Field and laboratory-based investigations were used including X-ray diffraction (XRD), Transmission and Scanning Transmission Electron Microcopy coupled with energy dispersive spectroscopy (S/TEM-EDX), Inductively Coupled Plasma Atomic Emission Spectroscopy (ICP-AES) and Inductively Coupled Plasma Mass Spectrometry (ICP-MS).

Chapter 1 focuses on understanding the impact of modern euxinic conditions on bulk sediment and clay fractions. The study demonstrates that (1) XRD-detectable sulfur bearing minerals in a soil profile exposed to euxinic groundwater are present outside the zone with visible sediment iron reduction and (2) Al-smectite nanoparticles primarily respond to euxinic conditions by immobilizing cations via adsorption or inter-layer cation exchange rather than significantly changing their octahedral sheet cation composition. Chapter 1 has been published in The American Chemical Society (ACS) journal *ACS Earth and Space Chemistry* (Apalara et al., 2025).

Chapter 2 investigates how smectite clay octahedral sheet composition influences smectite interaction with a modern euxinic spring in terms of morphological changes and secondary mineral formation. Two different smectites with differing octahedral sheet compositions; SWa-1 (Fe-rich) and SAz-1 (Al-rich) were reacted at Zodletone spring for 504 hours. The study shows that SWa-1 underwent progressive reductive dissolution of Fe, accompanied by color change from yellow to black. The dissolution was followed by secondary Fe-sulfide and $S^0$ precipitation. However, SAz-1 showed remarkable stability of its aluminosilicate framework despite minor Fe loss. In addition, the interlayer of both clays responded differently to the euxinic condition, in that Ca dominated the interlayer of SWa-1 while Na dominated the interlayer of SAz-1 by the end of the experiment.

In Chapter 3, trace element mobility in a modern euxinic environment was studied in the presence of smectites with differing octahedral sheet composition. The Fe-rich and Al-rich clays from chapter 2 were studied, with three samples collected over the 504 hours total reaction time in the euxinic spring. The study demonstrates that, after 504 hours, reduced SWa-1 showed the highest trace element enrichment, particularly Ba, Rb, Sr and Cs, correlating with increasing Fe(III)-reduction, while SAz-1 showed similar trend but the enrichment of Ba, Rb, Sr and Cs are not as high as seen in SWa-1. Also, a reverse trend in the accumulation of chalcophilic trace elements,

lithophilic trace elements and REEs in SWa-1 was seen in SAz-1. In the reacted Fe-rich SWa-1, chalcophiles are enriched at the start of the experiment but depleted after 8 hours, whereas in the reacted Al-rich SAz-1, chalcophiles are only enriched after 504 hours in the spring. Furthermore, In SWa-1, lithophiles are enriched after 504 hours in the spring while in SAz-1, only Cr, Ta, Ga and Th show short term enrichment after 120 hours followed by depletion after 504 hours in the spring. The enrichment of REEs was seen in reacted SWa-1 while no REE enrichment was observed in SAz-1 throughout the reaction time. Overall, this dissertation demonstrated new findings regarding the interactions between Fe- versus Al-rich smectites that reacted with euxinic spring waters for thousands of years, and their nanoscale interactions with iron and sulfur, major elements, and trace elements.

## References


(1) Jørgensen, B. B.; Findlay, A. J.; Pellerin, A. The Biogeochemical Sulfur Cycle of Marine Sediments. *Front. Microbiol.* **2019**, *Volume 10-2019*. https://doi.org/10.3389/fmicb.2019.00849.

(2) Sperling, E. A.; Melchin, M. J.; Fraser, T.; Stockey, R. G.; Farrell, U. C.; Bhajan, L.; Brunoir, T. N.; Cole, D. B.; Gill, B. C.; Lenz, A.; Loydell, D. K.; Malinowski, J.; Miller, A. J.; Plaza-Torres, S.; Bock, B.; Rooney, A. D.; Tecklenburg, S. A.; Vogel, J. M.; Planavsky, N. J.; Strauss, J. V. A Long-Term Record of Early to Mid-Paleozoic Marine Redox Change. *Sci. Adv.* **2021**, *7* (28), eabf4382. https://doi.org/10.1126/sciadv.abf4382.

(3) Lyons, T. W.; Anbar, A. D.; Severmann, S.; Scott, C.; Gill, B. C. Tracking Euxinia in the Ancient Ocean: A Multiproxy Perspective and Proterozoic Case Study. *Annu. Rev. Earth Planet. Sci.* **2009**, *37* (1), 507–534. https://doi.org/10.1146/annurev.earth.36.031207.124233.

(4) Tribovillard, N.; Algeo, T. J.; Lyons, T.; Riboulleau, A. Trace Metals as Paleoredox and Paleoproductivity Proxies: An Update. *Chem. Geol.* **2006**, *232* (1–2), 12–32. https://doi.org/10.1016/j.chemgeo.2006.02.012.

(5) Jenkyns, H. C. Geochemistry of Oceanic Anoxic Events: REVIEW. *Geochem. Geophys. Geosystems* **2010**, *11* (3), n/a-n/a. https://doi.org/10.1029/2009GC002788.

(6) Bristow, T. F.; Milliken, R. E. Terrestrial Perspective on Authigenic Clay Mineral Production in Ancient Martian Lakes. *Clays Clay Miner.* **2011**, *59* (4), 339–358. https://doi.org/10.1346/CCMN.2011.0590401.

(7) Lyons, T. W.; Severmann, S. A Critical Look at Iron Paleoredox Proxies: New Insights from Modern Euxinic Marine Basins. *Geochim. Cosmochim. Acta* **2006**, *70* (23), 5698–5722. https://doi.org/10.1016/j.gca.2006.08.021.

(8) Canfield, D. E.; Erik Kristensen; Bo Thamdrup. The Sulfur Cycle. In *Aquatic Geomicrobiology*; Canfield, D. E., Kristensen, E., Thamdrup, B., Eds.; Advances in Marine Biology; Academic Press, 2005; Vol. 48, pp 313–381. https://doi.org/10.1016/S0065-2881(05)48009-8.

(9) Rickard, D.; Luther, G. W. Chemistry of Iron Sulfides. *Chem. Rev.* **2007**, *107* (2), 514–562. https://doi.org/10.1021/cr0503658.

(10) Rickard, D. Sulfur Chemistry in Aqueous Solutions. In *Developments in Sedimentology*; Elsevier, 2012; Vol. 65, pp 31–83. https://doi.org/10.1016/B978-0-444-52989-3.00002-7.

(11) Wakeham, S. G.; Amann, R.; Freeman, K. H.; Hopmans, E. C.; Jørgensen, B. B.; Putnam, I. F.; Schouten, S.; Damsté, J. S. S.; Talbot, H. M.; Woebken, D. Microbial Ecology of the Stratified Water Column of the Black Sea as Revealed by a Comprehensive Biomarker Study. *Org. Geochem.* **2007**, *38* (12), 2070–2097. https://doi.org/10.1016/j.orggeochem.2007.08.003.

(12) Dubilier, N.; Bergin, C.; Lott, C. Symbiotic Diversity in Marine Animals: The Art of Harnessing Chemosynthesis. *Nat. Rev. Microbiol.* **2008**, *6* (10), 725–740. https://doi.org/10.1038/nrmicro1992.

(13) Sanders, W. E. Rate and Mechanism of Barite Mineralization at Zodletone Mountain, Southwestern Oklahoma. PhD Thesis, University of Oklahoma, 1998.

(14) Gilleaudeau, G. J.; Sahoo, S. K.; Ostrander, C. M.; Owens, J. D.; Poulton, S. W.; Lyons, T. W.; Anbar, A. D. Molybdenum Isotope and Trace Metal Signals in an Iron-Rich Mesoproterozoic Ocean: A Snapshot from the Vindhyan Basin, India. *Precambrian Res.* **2020**, *343*, 105718. https://doi.org/10.1016/j.precamres.2020.105718.

(15) Johnston, D. T.; Wolfe-Simon, F.; Pearson, A.; Knoll, A. H. Anoxygenic Photosynthesis Modulated Proterozoic Oxygen and Sustained Earth's Middle Age. *Proc. Natl. Acad. Sci.* **2009**, *106* (40), 16925–16929. https://doi.org/10.1073/pnas.0909248106.

(16) Lyons, T. W.; Reinhard, C. T.; Planavsky, N. J. The Rise of Oxygen in Earth's Early Ocean and Atmosphere. *Nature* **2014**, *506* (7488), 307–315. https://doi.org/10.1038/nature13068.

(17) Hochella, M. F.; Mogk, D. W.; Ranville, J.; Allen, I. C.; Luther, G. W.; Marr, L. C.; McGrail, B. P.; Murayama, M.; Qafoku, N. P.; Rosso, K. M.; Sahai, N.; Schroeder, P. A.; Vikesland, P.; Westerhoff, P.; Yang, Y. Natural, Incidental, and Engineered Nanomaterials and Their Impacts on the Earth System. *Science* **2019**, *363* (6434), eaau8299. https://doi.org/10.1126/science.aau8299.

(18) *Clays*; Meunier, A., Ed.; SpringerLink Bücher; Springer-Verlag Berlin Heidelberg: Berlin, Heidelberg, 2005. https://doi.org/10.1007/b138672.

(19) Rickard, D. Euxinic Systems. In *Developments in Sedimentology*; Elsevier, 2012; Vol. 65, pp 495–542. https://doi.org/10.1016/B978-0-444-52989-3.00013-1.

# Chapter 1: Understanding the impact of a modern euxinic spring on sediment using bulk sediment and smectite clay-preserved proxies

Itunu T. Apalara[1*], Caitlin Hodges[1], Julian E. C. Sabisch[2], Megan E. Elwood Madden[1], Preston R. Larson[2], Andrew S. Elwood Madden[1,2]

[1]School of Geosciences, University of Oklahoma, Norman, OK 73019, USA

[2]Samuel Roberts Noble Microscopy Laboratory, University of Oklahoma, Norman, OK 73019, USA

Keywords: Euxinic, Smectite, TEM, S/TEM, EDX, XRD

Citation:

Apalara, I. T.; Hodges, C.; Sabisch, J. E. C.; Elwood Madden, M. E.; Larson, P. R.; Elwood Madden, A. S. Understanding the Impact of a Modern Euxinic Spring on Sediment Using Bulk Sediment and Smectite Clay-Preserved Proxies. *ACS Earth Space Chem.* **2025**, *9* (2), 265–276. https://doi.org/10.1021/acsearthspacechem.4c00269.

## Abstract

Modern euxinic environments are useful proxies for early Earth. We investigated the morphological and chemical properties preserved in sediments impacted by a modern euxinic spring, an early Earth proxy, as compared to adjacent unimpacted sediments. We used X-ray diffraction (XRD) to analyze the mineralogy of bulk sediment and isolated clay fractions. We further examined morphology and chemistry of smectite clay nanoparticles using scanning/transmission electron microscopy (S/TEM) and energy-dispersive X-ray spectroscopy (EDX). XRD results show pyrite and barite are present in all the impacted sediments but absent in the unimpacted sediments. Although grain size analysis shows the impacted samples have more clay-sized particles, the mineralogy of impacted and unimpacted clay fractions are both comprised of smectite, chlorite, kaolinite, and illite clays. We further focused on smectite clay nanoparticles as they are known to be sensitive proxies for redox conditions. Smectites with platy and cornflake texture were prevalent in all samples. However, EDX results reveal differences between the smectites in the impacted and unimpacted samples: impacted smectites additionally incorporate S, Ba, and Sr. Furthermore, STEM-EDX shows evidence of nanoscale barite and pyrite precipitation on the impacted smectites. Ultimately, this study demonstrates that (1) XRD-detectable sulfur bearing minerals in a soil profile exposed to euxinic groundwater are present outside the zone with visible sediment iron reduction and (2) Al-smectite nanoparticles primarily respond to euxinic conditions by immobilizing cations via adsorption or inter-layer cation exchange rather than significantly changing their octahedral sheet cation composition.

## 1.0 Introduction

Modern euxinic (sulfidic and anoxic) environments are natural laboratories with the potential to shed light on the early ages of Earth and the habitability of extra-terrestrial bodies such as Mars. Euxinic conditions dominated the Earth's oceans in the early Proterozoic, lasting about 1 Ga[1,2]; euxinic conditions returned in the later Cambrian[3], the end Ordovician[4] and were prevalent up to the mid – early Devonian[5]. These periods of euxinia influenced the evolution of life on Earth due to the complex interplay between redox conditions and trace metal mobility. For example, the productivity of some phytoplankton depends upon the availability of redox-active essential trace elements[6,7]. As Earth became oxygenated, sharp redox interfaces were created where sulfidic waters and an oxygenated atmosphere interacted, providing the energy needed to support life in the form of electron transfers between redox couples.

Most studies focused on understanding euxinic conditions and sediment interactions have analyzed ancient euxinic sediments or used laboratory experiments designed to mimic field conditions[8–12], both of which lack the ability to correlate directly observable physical and biogeochemical groundwater processes with sediment characteristics. Instead, concentrations and isotopic fractionation measurements of trace metals are frequently used to interpret the dominant biogeochemical redox processes recorded in ancient sedimentary rocks. Moreover, bulk mineralogy in euxinic sediments have been widely studied. Most of these studies use bulk methods which do not show nanoscale materials and their associated processes. Minerals at the nanoscale react differently from the macroscale due to a combination of size-dependent properties[13,14]. One of the minerals that naturally fits into this nanoscale group is smectite.

Smectite clay, especially Fe-bearing smectite is redox – sensitive[15–17]. Small size (0.02 – 0.2 micrometer), large surface area[18], and layer charge are some of the properties that make smectite

a reactive clay mineral[15,17]. Biologically and abiologically-induced redox conditions alter the structure of smectites, which in turn change the mineral's physical and chemical properties[15,19–22]. For instance, a change in the oxidation state of Fe in Fe-rich smectites leads to the rearrangement of the crystal structure. This rearrangement occurs mostly in their octahedral sheet. A good example is the reduction of Fe(III) to Fe(II) in the octahedral sheet. This transfer of electrons is often accompanied by dehydroxylation leading to structural modifications, changes in hydration properties and ultimately coloration[15–17,20,23]. The physical shrink-swell behavior of smectites also responds to redox-induced changes to the octahedral sheet, which in turn affect the bonding strength between layers. This swelling property is also influenced by relative humidity and the ionic properties of the interlayer metals present[24–26].

Previous studies on the evolution of continental clay and marine oxygenation on the early earth have suggested that smectites do not preserve their inherent chemical composition after long term continental weathering and marine authigenesis[27]. Montmorillonite is not expected to be prevalent in the anoxic, $CO_2$ rich Hadean ocean, but likely became more abundant from weathering of granitic rocks starting at ~3.5 Ga. The relative increase in the abundance of smectite starting near the end of the Proterozoic has been correlated with decreasing $CO_2$ levels in the atmosphere[28]. This implies that smectites are not expected to be persistent under extremely reducing conditions. However, studies have shown that under anaerobic conditions, aqueous alteration of basalt and authigenesis in hydrothermally active zones can produce ferrous smectite both on earth and Mars[19,29]. Ferrous smectite can also be formed through laboratory experiments under anaerobic conditions[30]. While unaltered smectites from the Hadean are expected to be compositionally different from what we have today, ferric iron is expected to have replaced ferrous iron in the

smectite structure as a response to the great oxidation event[28]. Ultimately, few studies have directly addressed the persistence and authigenesis of smectite minerals under modern euxinic conditions.

Fe-Mg smectite, Al-rich smectites and sulphate minerals occur on Mars, which some have interpreted to be signatures of the paleo-activity of water and micro-organisms on early Mars[31–33]. The sulfur cycle is believed to have a significant influence on the paleoenvironmental conditions on Mars[31,34]. Studies on Martian meteorites, remote sensing data and in situ analysis on Mars have shown the presence of sulfur-rich minerals, mostly as sulfates, on Mars. Although martian meteorites reveal the presence of sulfide minerals, no *in situ* study has detected sulfide species on Mars[31,34,35]. Since sulfate minerals can be formed due to the oxidation of sulfide to sulfate in the presence of some cations, the study of modern euxinic environments on Earth is pivotal to the exploration of habitability on Mars.

In view of the redox sensitivity of Fe-bearing smectite, we hypothesized that interaction of sediment with an actively flowing modern euxinic spring will alter the chemical composition and morphology of existing smectite clay in the sediment and lead to authigenic clay with potentially distinctive characteristics. We also expect formation of sulfur-bearing minerals in the bulk sediments that have been impacted by the euxinic condition. We aim to explore the effect of modern euxinic conditions on the bulk sediment composition, and chemical and morphological properties of smectite at the nanoscale using X-ray diffraction analysis and electron microscopy. This study will give insights on possible processes related to the formation and preservation of smectite on Mars, and its potential for habitability. Also, this study will further add to our understanding of how geochemical processes affected sediments and smectite clay on early euxinic-Earth, especially during the Proterozoic widespread euxinia[36–38].

## 1.1 Study Area

Zodletone spring, located in southwest Oklahoma, is a deeply sourced, sulfide-rich (8-10 mM) spring in the Cambrian-Ordovician Slick Hills of the Anadarko Basin in SW Oklahoma[39]. The spring originates from the oil brines in the basin, which have migrated through faults and mixed with groundwater[40] before discharging at the surface (Figure 1). The Zodletone spring water is a brine with high major-ion concentrations[40] and a pH of 7.1 (Table 1). Methane gas bubbles out of the spring, which is believed to have also been sourced from the deeply buried hydrocarbons[41]. Also, this spring water has journeyed through carbonate formation at the subsurface, which makes it rich in dissolved inorganic carbon that degasses as $CO_2$ at the surface[42]. The spring discharges into the Saddle Mountain creek, also known as 'Stinking Creek' ~ 20 m from the spring[39–41,43,44]. At the bank of the creek, the euxinic-spring can be seen discharging out of the sediment at approximately 2 m below land surface, causing a dark-greyish coloration of the sediment.

This field site has drawn the attention of researchers over the years because of the high concentrations of methane and sulfur in the spring water and the corresponding rapid biogeochemical cycling of carbon and sulfur that occurs as the spring water interacts with the atmosphere. One of such complex biogeochemical processes is the precipitation of barite, facilitated by bacteria as the spring discharges to the surface. Significant biotic activity has been reported, including the presence of photosynthetic green and purple sulfur-oxidizers and sulfate-reducing bacteria[39,45]. The activities of phototrophic bacteria were established through the noticed increase in sulfate concentration in the spring during the day as compared to the night[39]. The spring water does not contain detectable oxygen, with the highest concentration of sulfide at the source. As the concentration of sulfide reduces with distance away from the spring, elemental sulfur and sulphate concentrations increase with distance from the spring. The varying concentration of

different sulfur species with distance from the spring source is related at least in part to the presence of purple and green photosynthetic sulfur-oxidizing bacteria[39,44,45].

Table 1: Major ion concentrations in Zodletone spring water[40]

| Element | Concentration (ppm) | Concentration (mmol / kg) |
|---|---|---|
| $Na^{+}$ | 2800 | 121.8 |
| $Ca^{2+}$ | 320 | 7.98 |
| $Mg^{2+}$ | 150 | 6.17 |
| $Ba^{2+}$ | 67 | 0.49 |
| $K^{+}$ | 27 | 0.69 |
| $Sr^{2+}$ | 19 | 0.22 |
| $S^{2-}$ | 139 | 4.02 |
| $Cl^{-}$ | 6160 | 173.8 |
| $HCO_3^{-}$ | 481 | 7.88[42] |

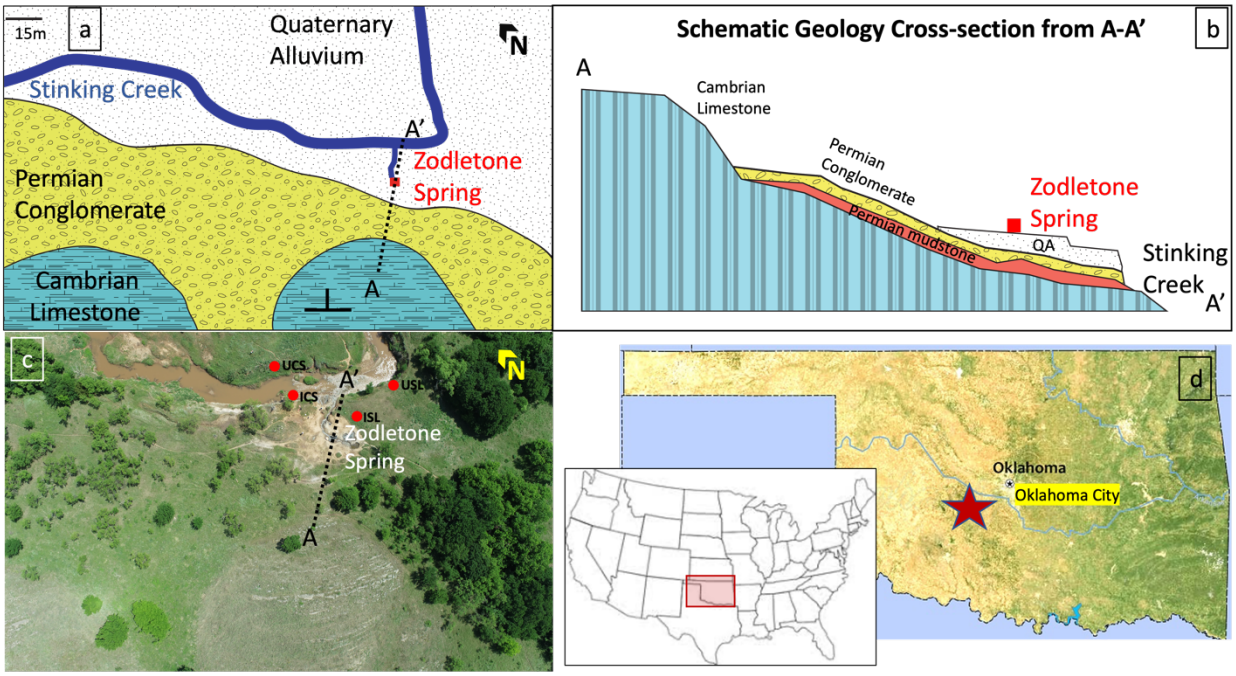

Figure 1: Geologic context for Zodletone Spring. (a) Geological map of the study area showing the surficial geologic units in the study area; (b) Conceptual geological cross-section across the euxinic-spring; (c) Drone-collected arial photograph of the study area showing the sampling points and location of cross-section in (b); (d) Star on map of Oklahoma indicates the study area location.

## 1.2 Sampling and Methods

### 1.2.1 Field Sampling

We present data from four sediment samples collected from the study area. One set of sediments were studied to understand the effect of euxinic condition on sediment that are directly exposed to the atmosphere (creek sediments) while another set of samples were studied to investigate the impact of euxinic condition on sediments that are not directly exposed to the atmosphere (soil profile sediments). Generally, the sediments are reddish-brown siliciclastic Quaternary alluvium deposits with gravel- to cobble-sized limestone. The sediment on the southern, spring-impacted side of Saddle Mountain Creek ('Stinking Creek') is generally more consolidated than the sediment on the northern spring-unimpacted side. The more consolidated soil on the euxinic-spring impacted side could be due to the precipitation of minerals that act as cements due to interaction with the spring brine. At the creek bank, we collected one sediment sample from the obviously euxinic-spring-impacted-bank (Figure 2a) (Impacted Creek Sediment - ICS) and another sample from the unimpacted opposite bank (Unimpacted Creek Sediment - UCS). At a location about 20 m to the west of the euxinic spring source, we collected a depth profile from the surface down to an obvious euxinic-spring-impacted soil layer. We used a sampling auger, taking soil samples at 30 cm depth intervals. A grey-colored horizon that has obviously been impacted by the euxinic spring was encountered at about 220 cm depth (Figure 2b) (Impacted Soil Layer - ISL). Figure 1c shows the locations sampling points overlain on a site map. Euxinic-spring impacted sediments were selected where an abrupt change in coloration from brown to greyish color distinguishes them

from overlying unimpacted sediments. As a result, we collected another depth profile at a location about 20 m east of the euxinic spring, which serves as a background sample. In this case, we reached 220 cm soil depth without encountering any color changes or obvious interaction with the euxinic spring (Unimpacted Soil Layer - USL). All samples were kept in sealed plastic bags and transported with ice packs to the laboratory where they were frozen to prevent further reactions.

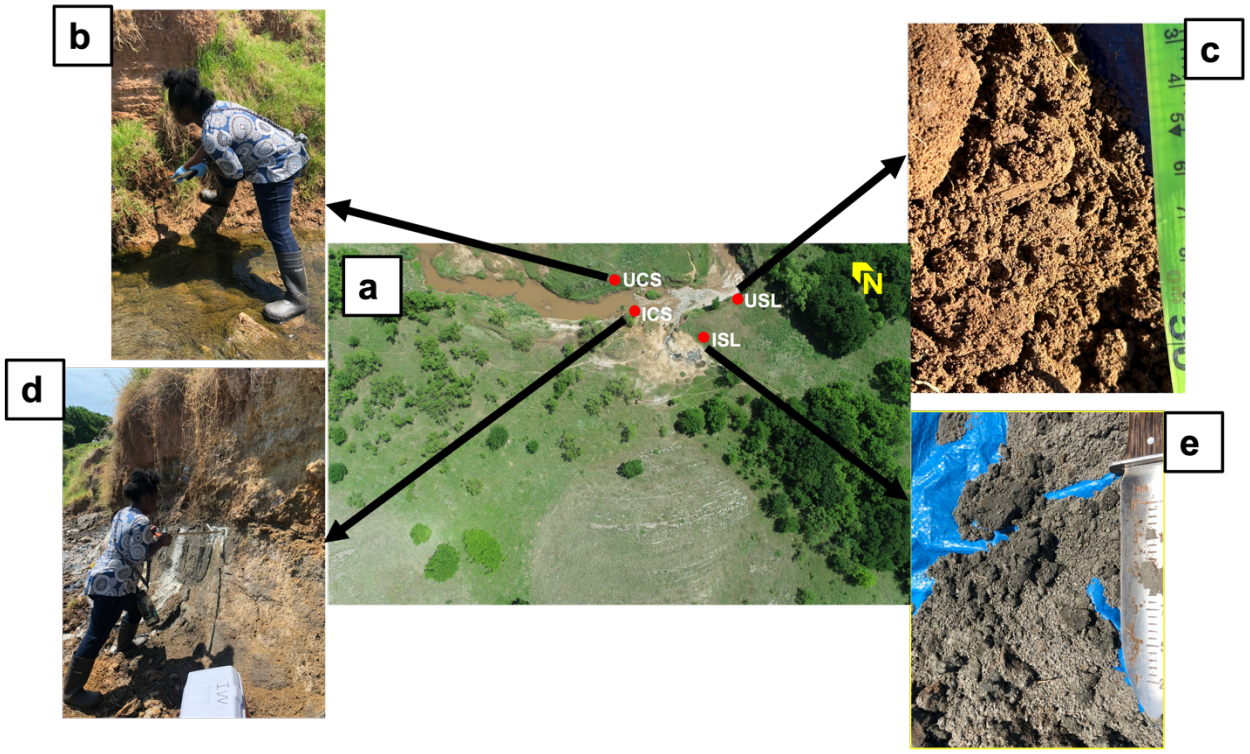


Figure 2: Pictures (a) Drone-collected arial photograph of the study area showing the sampling points (b) Unimpacted creek sediment (UCS) (c) Unimpacted soil layer at 220 cm depth (USL) (d) Impacted creek sediment (ICS) (e) Impacted soil layer at 220 cm depth (ISL).

### 1.2.2 Laboratory study

#### 1.2.2.1 Grain size analysis

We measured grain size using wet sieving on splits reserved only for this purpose. We dispersed the sediment by adding 35 ml of 0.05 M sodium hexametaphosphate solution to 5 g of soil sample. The mixture was placed on a shaker for at least 2 hours. Tubes were allowed to settle for another 2 hrs. 2.5 mL of suspension containing the clay fraction was carefully removed using a micropipette. The remaining soil slurry was sieved through a 53-micron mesh to separate the silt from sand. All separated portions were oven dried in pre-weighed aluminum weigh pans at 105 $^0$C for 24 hours. Percentage grain sizes were calculated as described in Kettler et. al., 2001[46].

#### 1.2.2.2 X-ray diffraction

About 2 mL of each bulk sediment sample was micronized using a McCrone Micronizing mill with the addition of 5 mL of methanol. The micronized samples were air-dried and bulk mineralogical analysis with powder X-ray diffraction (XRD) was done using a Rigaku Ultima IV diffractometer using Cu-K-alpha radiation (40 kV, 44 mA) with a scintillation detector and diffracted beam curved graphite monochromator. Data analysis was completed using Jade Pro software with the ICDD (International Centre for Diffraction Data) PDF4+ database.

For each sediment sample, the clay size fraction (<2 microns) was also analyzed separately. We mixed approximately 5 g of sample in ~200 mL of deionized water with ~0.5 g of Na-hexametaphosphate, then dispersed the suspension using a sonicating dismembrator for 10 minutes with a pulse and rest time interval of 10 s. The dispersed sample was then centrifuged for 5 minutes at 800 rpm. The supernatant was decanted, and a subset of the remaining clay fraction was Ca-saturated by adding $CaCl_2$. The separated clay was oriented on fused silica slides using the filter-peel method[47]. We also created an oriented clay sample from the subsample that had not been saturated with $CaCl_2$ to investigate smectite composition in their naturally occurring state in the

field. Both oriented clay samples were analyzed using a Rigaku SmartLab 9 kW diffractometer using Cu-K-alpha radiation (45 kV, 250 mA). The separated clays were analyzed air-dried, later solvated with ethylene glycol for about 22 hours and analyzed and finally heated at 550 °C for 1 hour and analyzed with 2 theta ranging from 2° to 32°.

#### 1.2.2.3 Electron microscopy

A portion of the separated clay samples from both impacted and unimpacted sediments were centrifuged again at 4500 rpm for 15 minutes to concentrate the smectite clay fraction. The isolated smectite was prepared for electron microscopy by dispersion in methanol and pipetting directly onto a lacey carbon copper grid. Samples were analyzed for morphology and semi-quantitative chemical composition using Transmission Electron Microscopy (TEM) and Scanning/ Transmission Electron Microscopy coupled with energy dispersive spectroscopy (STEM-EDX). Analysis was done using a JEOL 2010F TEM with a Schottky field-emission source at 200 kV. A JEOL 2000FX TEM with a tungsten filament source, operated at 200 kV, was used to analyze electron diffraction patterns of smectite particles. Smectite nanoparticles are identified based on their elemental composition, morphology, and electron diffraction pattern.

#### 1.2.2.4 Safety statement

No unexpected or unusually high safety hazards were encountered.

## 1.3 Results

### 1.3.1 Grain size distribution

The bulk sediment grain size analysis (Table 2) shows that compared to the unimpacted background sites, both impacted sites show a large increase in the clay size fraction, a large decrease in the silt fraction, and a small decrease in sand size fraction. The result of the grain size

analysis is consistent with textures observed in the field, where impacted layers exhibit greater plasticity.

Table 2. Grain size distribution of soil samples labeled as Unimpacted soil layer (USL), Impacted soil layer (ISL), Unimpacted creek sediment (UCS), and Impacted creek sediment (ICS). Reported values are in weight %.

| **size fraction** | **USL** | **ISL** | **UCS** | **ICS** |
|---|---|---|---|---|
| clay | 5.1 | 46.6 | 35.9 | 45.9 |
| silt | 49.9 | 12.3 | 15.1 | 7.5 |
| sand | 45.0 | 41.0 | 49.0 | 46.6 |

### 1.3.2 Bulk sediment mineralogy

The bulk mineralogy of both background unimpacted samples (USL and UCS) includes plagioclase, quartz, calcite, K-feldspar, and dolomite (Figure 3). The impacted soil layer (ISL) contains the same minerals, but with the addition of ankerite, pyrite, barite, and gypsum. The impacted creek sediment (ICS) also contains plagioclase, quartz, calcite, K-feldspar, pyrite and barite but dolomite is absent (Figure 3). Quartz made up more than 50% of the bulk composition of all the samples. USL and UCS samples contain more calcite than the ISL and ICS samples. The ISL sample contained significantly less plagioclase than the concentrations observed in the other samples . It is noteworthy that, while the ISL is obviously impacted by the euxinic spring at a soil layer of 220 cm, through XRD analysis, we noticed sulfur-bearing minerals at shallower depth above it. At a depth of about 90 – 122 cm, without visible color change, we have higher concentration of pyrite, than in the ISL. Also, at a greater depth of 163 – 200 cm of the same soil

profile, just above the ISL, we have an accumulation of more barite and a little less pyrite than in the ISL (Figure S1).

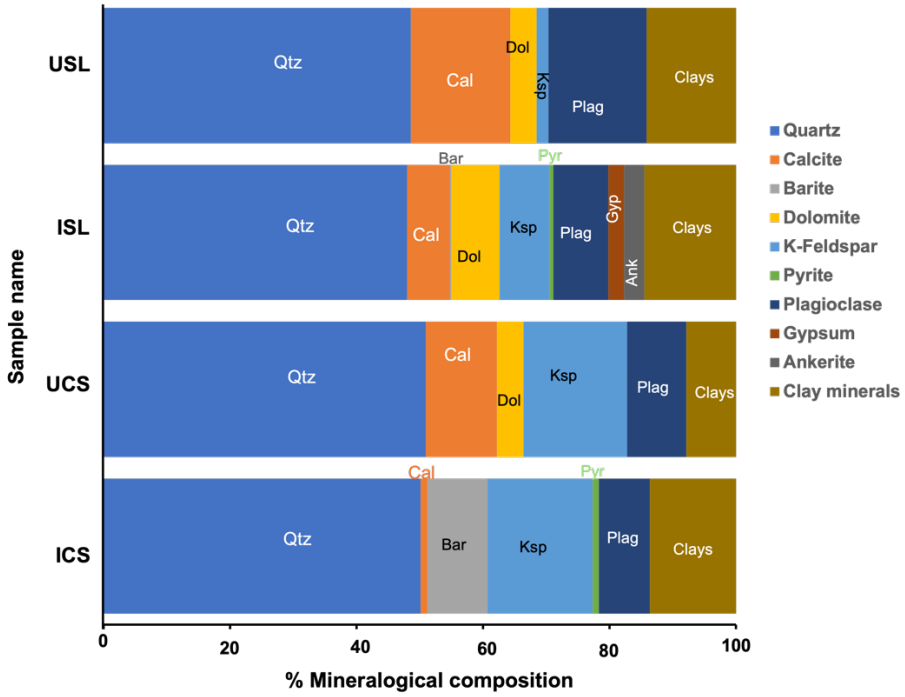


Figure 3: Bulk mineralogy of unimpacted and impacted soil layers and creek sediments, reported as weight percent.

### 1.3.3 Clay mineralogy

Oriented clay was analyzed air-dried, later treated with ethylene-glycol and lastly heat-treated. All clay minerals were identified based on their peak positions following each treatment, which were directly proportional to their interplanar spacings. In the air-dried samples, the smectite 001 peak in ICS, UCS, ISL, USL samples are at 14.3 Å, 14.4 Å, 14.2 Å, and 14.4 Å respectively. However, these smectite 001 peak positions shifted to 17-18 Å when solvated with ethylene glycol (Figure 4) and all collapse to 10 Å during heat treatment. A small feature at 13-14 Å after heating (Figure S2 – S5) is indicative of an extra octahedral layer from chlorite.

Although overlapping peaks present challenges and uncertainties in the unequivocal identification of mixtures of chlorite and kaolinite (e.g., ref. 47), the evidence is consistent with the presence of both. The peak at 7.1 Å completely disappeared in all heat-treated samples. This peak could be indicative of either kaolinite or chlorite. However, the peak at 4.76 Å is only indicative of chlorite. Also, the shape of the 3.5 Å peak shows it has multiple components that can be attributed to kaolinite (~3.57 Å and chlorite ~3.53-3.55 Å). The disappearance of the peak at 7.1 Å, while a small portion of the 3.5 Å peak survives in the heat-treatment (Figure S2 – S5) is also consistent with the presence of both phases. Corresponding peaks for illite (001, 002 and 003) and quartz 101 remained unchanged in the air dried, ethylene glycol solvated and heat-treated scans. The unusually tall and sharp peak at 3.5 Å in the ICS sample is due to the presence of barite in the clay-size extract.

Furthermore, a set of aliquots of all the samples was analyzed without $Ca^{2+}$ saturation. This was done to investigate the effect of smectite interlayer cations on smectite 001 peak position. We saw a slight difference in the smectite 001 d-spacing of the impacted samples and unimpacted samples. Without $Ca^{2+}$ saturation, air dried impacted samples, ICS and ISL, have smectite 001 d-spacings of 14.3 Å and 14.3 Å, respectively. Air dried unimpacted samples, UCS and USL, have smectite 001 d-spacings of 14.5 Å and 14.4 Å, respectively.

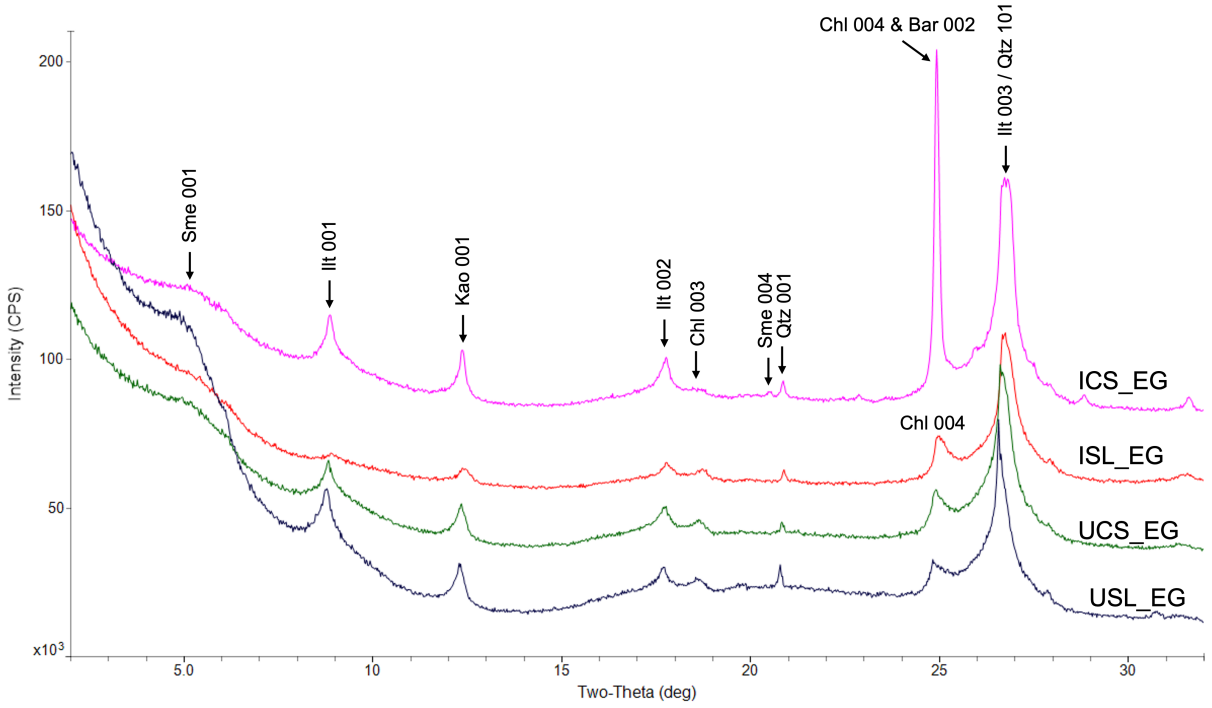


Figure 4: Clay mineralogy of clay fraction of ICS, UCS, ISL and USL treated with ethylene glycol (spectra were offset for clarity)

### 1.3.4 Smectite morphology

TEM bright field imaging was used to investigate the morphology of smectite nanoparticles in the samples. The smectite nanoparticles in all the samples show a flat, platy, corn flake texture. The microstructures on the smectite nanoparticles show a few curled edges (shown with red arrows) and dark spots. Individual smectite crystallites can also be seen as they offset from one another (Figures 5a – 5d). Further analysis in S/TEM shows different degrees of aggregation from single individual crystallites to aggregated structures. These variations in aggregation are not particular to any of the samples.

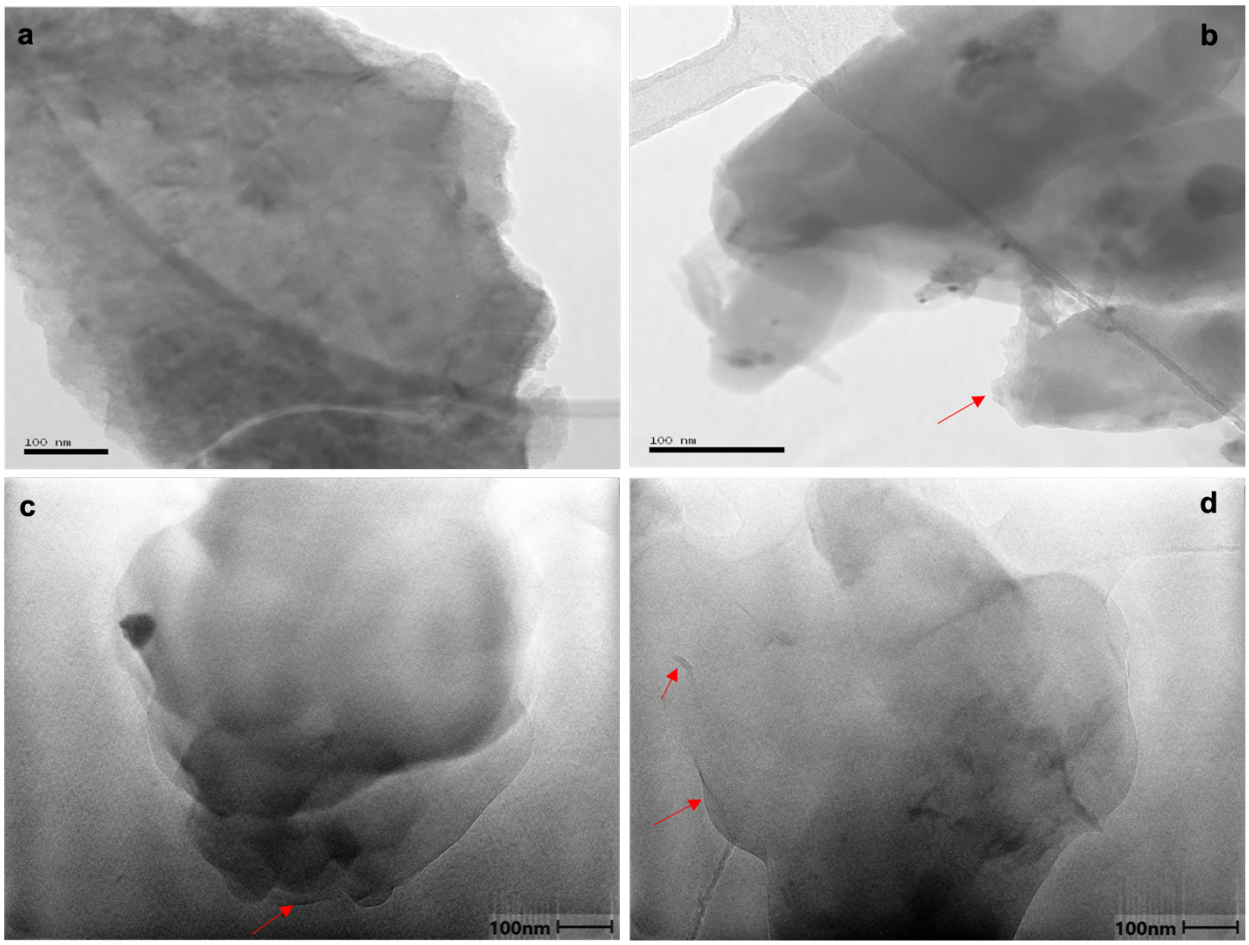


Figure 5: TEM images showing flat, cornflake morphology of smectite clay in (a) UCS (b) ICS (c) USL (d) ISL. Scale bars are all 100 nm.

### 1.3.5 Smectite chemical composition

S/TEM-EDX revealed the elemental composition of smectite nanoparticles. The unimpacted smectites in the UCS and USL samples contain Al, Si, Fe, Mg, Ti, K and Ca, and Na, while impacted smectite nanoparticles from ICS and ISL contain the same elements, as well as S, Ba and Sr as a signal of the impact of the euxinic-spring (Table S1 – S4). Smectite nanoparticles from all the samples are composed primarily of Si followed by Al . Fe and Mg are also present in all the samples, but at lower concentrations compared to Al and Si. Na, K and Ca are present at much lower concentrations and are believed to be in the interlayers of the smectites, while Si is allocated

to the tetrahedral sheet, and Al, Fe, and Mg are allocated to the octahedral sheet. S/TEM-EDX analysis shows that brighter regions observed on ICS and ISL smectite nanoparticles contain S, Ba, and a little more Fe than darker regions (Figures 6a – 6d). Also, brighter regions in USL and UCS contain more Fe (Figures 6e – 6h).

.

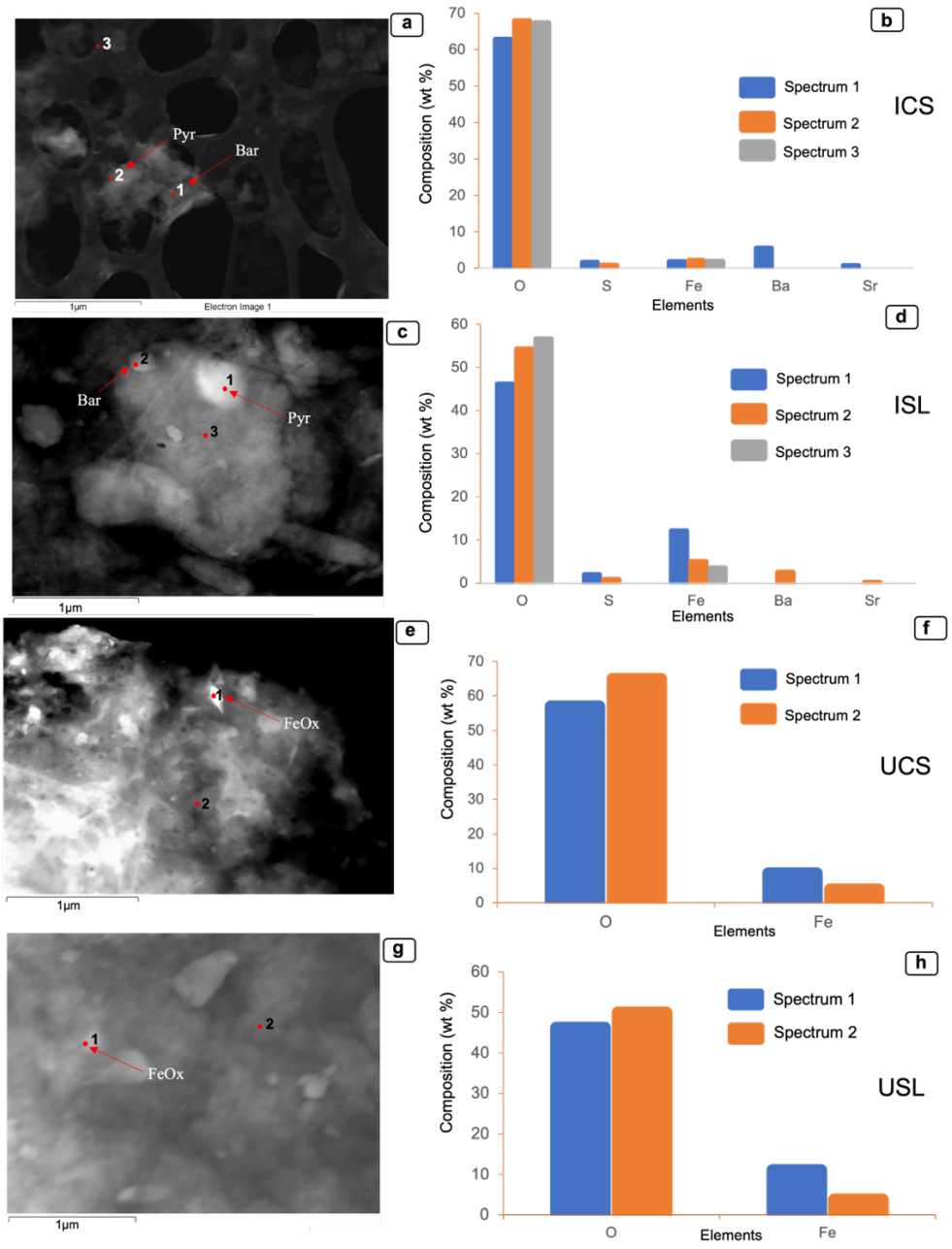

Figure 6: STEM images and corresponding element abundances of nanoscale domains within ICS (a-b), ISL (c-d), UCS (e-f) and USL (g-h) smectite respectively; (b) and (d) show EDX spectra of selected elements corresponding to indicated points on the adjacent image demonstrating the presence of surficial pyrite and barite on smectite clay; (f) and (h) show EDX spectra of selected elements from indicated points showing only surficial adsorption of iron oxide on smectite clay. No Ba or S were detected in unimpacted samples.

## 1.4 Discussion

### 1.4.1 Effect of modern euxinic conditions on bulk sediment and clay mineral composition

The impact of the modern euxinic spring is not only visible in the color of the impacted sediments but also in its mineral composition (Figure 2). The presence of sulfur bearing minerals in the impacted sediments and their absence in the unimpacted sediments show a direct influence of the euxinic spring (Figure 3). We observed pyrite and barite in the impacted samples. At our study site and others, formation of these two minerals is strongly linked to the activity of phototrophic sulfur oxidizing bacteria at the interface between euxinic and oxygenated conditions [39,43,44,48]. Higher concentration of barite in ICS is linked to a combination of biotic and abiotic oxidation of sulfide at the spring and sediment surface. Senko et. al. (2004) studied the effect of the activities of the phototrophic microorganisms on the diel variation of sulfate in the spring and demonstrated there is higher concentration of sulfate during the daytime. Insufficient oxygen to facilitate abiotic sulfide oxidation at the 220 cm soil depth and absence of light to increase the rate of biotic sulfide oxidation limited the precipitation of barite at the 220 cm depth. Sulfide oxidation at this depth is less pronounced than as it is in the impacted creek sediment at the surface. This is attributed to either the slower kinetics of abiotic sulfide oxidation over biotic sulfide oxidation or mediation by organisms who do not require light for metabolism which resulted in lower concentration of barite in the ISL.

The presence of sulfide and dissolved iron in the spring waters favors the precipitation of iron sulfides, including pyrite[49–53]; therefore, pyrite is indicative of sulfidic environments. However, our observations of lower pyrite concentrations in the impacted creek sediments, compared to the impacted soil layer are likely due to pyrite oxidation at the creek bank surface which led to the formation of surficial jarosite at the study area[41,54–57].

In general, we believe depth, insufficient oxygen and activity of microorganisms play a role in the crystallization of barite and pyrite in the soil profile. We suspect that the crystallinity of pyrite and barite could be responsible for their higher concentrations at shallower depths in the soil profile, since poorly crystalline minerals cannot be detected on XRD. The co-occurrence of pyrite and barite in the ISL demonstrates that sulfate and sulfide minerals can co-exist in modern euxinic sediments even when the fluid has no direct contact with the atmosphere.

Gypsum on the other hand, is only present in the ISL in a trace amount. The presence of gypsum in this euxinic-spring-impacted soil layer is believed to be directly related to contact with the euxinic spring, which contains nearly as much Ca as modern seawater (Table 1). Gypsum can be precipitated through evaporative precipitation, cation exchange, or mineral dissolution and reprecipitation in the presence of sulfate and free ions in the euxinic brine[58,59]. It is noteworthy that the ISL also has the lowest concentration of plagioclase feldspar (Figure 3). Dissolution of plagioclase feldspar could supply Ca ions for the precipitation of gypsum in the ISL, as the plagioclase concentration in the impacted layer (2.3 wt%) is much lower than the unimpacted (16.4 wt%). Ca ion could also have been sourced from the euxinic spring due to the interaction of the spring with the underlying Cambrian limestone. Non-evaporative precipitation of gypsum is also possible at this soil depth[60]. The low concentration of gypsum in ISL could also be related to its relatively high solubility and competition reactions between gypsum and other Ca-bearing

minerals such as calcite, dolomite and ankerite in the soil. However, the occurrence of gypsum in the ISL and its absence in ICS needs to be further studied.

The presence of calcite and dolomite in both euxinic-spring impacted and unimpacted sediments shows they are at least partly derived as detrital deposits, made more likely by the presence of abundant dolomite-bearing limestone in the Zodletone mountain that sits uphill from the spring site and elsewhere in the upstream Saddle Mountain Creek drainage area. Bachman et. al. (2018) showed that calcite can directly precipitate from the spring water in areas that are impacted by the euxinic spring, as calcite is observed in tufa-like precipitates in the spring sediment, floating on the surface of the euxinic spring, and along the impacted banks. Thus, carbonates in ISL and ICS are linked to both authigenic precipitation from the euxinic-spring and detrital deposition. The authigenic precipitation may be biologically-mediated or abiotic due to outgassing of $CO_2$ at the spring-air interface, Furthermore, biological activity may also contribute to the presence of dolomite in ISL, as studies have shown that the presence of sulfate reducing bacteria reduces the surface energy needed to nucleate dolomite, thereby enhancing the precipitation of dolomite under anoxic conditions [61–65]., However, trace concentration of calcite and the absence of dolomite in the ICS may be indicative of acidic conditions in ICS. Surficial jarosite is observed above the transect where the ICS was sampled, likely precipitating due to the transition from anoxic to oxic environment (Figure S6), leading to acidic conditions[41]. This acidic condition is likely driving carbonate dissolution in ICS. Previous studies have also shown that the presence of a brine under acidic conditions can drive the dissolution of dolomite[66–68]. This is in agreement with previous study which shows little to no traces of calcite in sediments that are exposed to the atmosphere and in contact with the euxinic spring [41].

The grain size analysis shows that ISL and ICS are enriched in clay-sized particles compared to the unimpacted sediments. This decrease in particle size is likely partly or wholly to mineral weathering coupled to authigenic mineral precipitation in these sediments due to their contact with the euxinic spring. Anoxic weathering of feldspars and other Al-rich deposits may have been one of the main sources of clay genesis on the early Earth[28]. In addition to the marked decrease in plagioclase concentrations in the impacted sediments, K-feldspar concentrations are slightly higher in the impacted samples when compared to the unimpacted sediments (ISL compared to the USL, as ICS compared to the UCS) (Figure 3). This suggests plagioclase feldspar may also form additional clays in the impacted samples.

Oriented-clay mount analysis for all the samples shows the presence of smectite, illite, kaolinite, chlorite and chlorite-smectite (C-S) mixed layer. The clay mineralogy of all samples is similar, but the high, sharp chlorite peak at 3.5 Å implies the presence of more chlorite and some clay sized barite in ICS. Small differences in the impacted and unimpacted smectite 001 d-spacings without saturation with $Ca^{2+}$, also shows there is a difference in the composition of interlayer cations and their hydration properties. Studies have shown that ionic properties of metals, such as hydration energy has a direct influence on smectite 001 peak positions[24,26,69–71]. Hydrated cations are more likely to enter into interlayer regions in smectites, causing the clay to swell. This expansion leads to an increase in smectite 001 d-spacing ; however, upon loss of hydration due to heating or cation exchange with less hydrated cations (e.g. $Na^{+}$), the 001 d-spacing decreases. The 001 d-spacing of unimpacted smectite shifts to lower d- spacings (higher angles) in the impacted samples (Figure 4). This suggests the impacted smectites contain cations with lower hydration energy, which could include $K^{+}$ and $Na^{+}$. The S/TEM-EDX analyses also indicate higher concentrations of these elements, especially Na in the impacted smectite particles (Figure 7).

### 1.4.2 Impact of modern euxinic conditions on smectite morphology and chemical composition

Dioctahedral Al-rich smectites were observed in all the samples (Figure 7a). The euxinic condition that impacted the ISL and ICS samples did not change the octahedral sheet composition of the smectite particles. In addition, the morphology of smectites in both impacted and unimpacted sediments are also the same. Previous studies investigating redox reactions in smectite have shown that octahedral sheet composition plays an important role in both physical and chemical properties, such as morphology [15]. Because the octahedra sheet compositions are the same, the morphology of smectite nanoparticles in all the samples is the same. The cornflake and platy textures from these smectites are typical of montmorillonites [72,73]. The morphology of the smectite nanoparticles in these samples are indicative of detrital origin due to their size and aluminum richness [73,74], In contrast, authigenic smectites mostly occur as grain coatings and usually possess the honeycomb surface structure. While our initial motivation for the study included an expectation that a silicate chemical weathering signatures under euxinic conditions would be recorded in the composition of the resultant authigenic clays, we did not observe any textures indicative of authigenic smectite precipitation in this study. However, the influence of the euxinic-spring is evident in the composition of the octahedra sheet in the ICS and interlayer composition of all the impacted smectites. In ICS, Al concentration increased when compared to the UCS which could be indicative of authigenesis. Impacted smectite nanoparticles contain $Na^+$ (Figure 7b) which was likely supplied by the euxinic $Na^+$-rich brine. The replacement of some of the $Ca^{2+}$ by $Na^+$ resulted in smaller interlayer d-spacing observed in the impacted smectites and larger interlayer d-spacing in the unimpacted-Ca-rich smectite. In addition, through S/TEM-EDX we observed evidence of adsorbed sulfur minerals on the surfaces of the impacted smectites, including pyrite and barite, which are absent in the unimpacted smectites. In comparison, unimpacted smectites have

indications of nano precipitates of iron oxide on their surfaces. Since the euxinic spring is rich in S, $Ba^{2+}$ and $Na^{+}$, we posit that S, $Ba^{2+}$ and $Na^{+}$ observed in the impacted smectites are sourced from the spring. Also, there is a co-precipitation of $Sr^{2+}$ with $Ba^{2+}$ in the nano-barite precipitates (Figure 6d). This is in agreement with previous studies of $Sr^{2+}$ incorporation into the structural framework of precipitated barite in the study area [43,44].

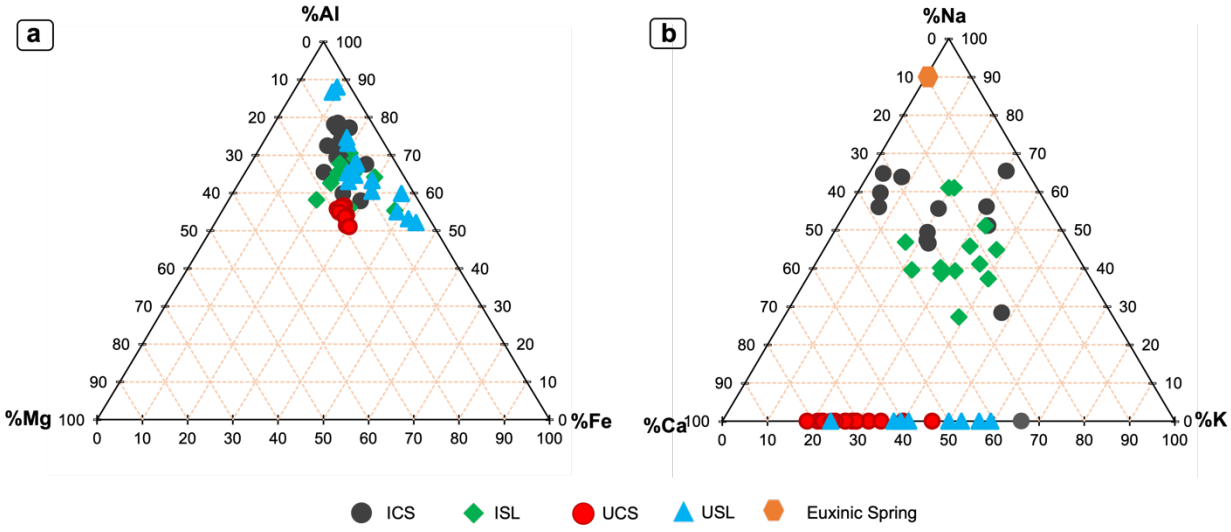


Figure 7: (a) Octahedral chemical composition (wt.%) of all smectites, (b) Interlayer chemical composition of all smectites (ICS: grey circle, ISL: green diamond, UCS: red circle, USL: blue triangle.). The chemical composition of the spring water is indicated by the orange hexagon in (b)

Smectite clay has been used to infer possible geochemical conditions in the past. In general, the smectite abundance in the clay fraction of marine sediments is low throughout the Proterozoic rock record, increasing dramatically for sedimentary rocks starting around 0.6 bya and continuing to rise to the present day [28]. For instance, the transition of the Proterozoic atmospheric condition from anoxic to oxic is recorded in the replacement of ferrous iron-rich smectite with more ferric

iron-rich smectite as a result of oxidative weathering[28]. In this study, smectites from both the impacted and unimpacted samples are Al-rich, therefore, we do not see any difference in their octahedral cation composition despite the ability of even low-Fe, Al-rich smectites to participate in redox reactions [75]. Current models of clay mineral [28] and Earth system evolution [27], suggest that Al-rich smectites and clay minerals produced through acidic silicate weathering are not expected to be prevalent under euxinic conditions, but only developed coincident with the 'clay mineral factory' [76] after 525 mya. However, our results suggest persistence and perhaps authigenesis of Al-rich, low Fe smectites in euxinic brine-impacted soils and sediments that are at least tens of thousands of years old[42].

## 1.5 Conclusions

This study shows that sulfate and sulfide minerals can form and coexist in a modern euxinic environment, whether the fluid is in direct contact with the atmosphere or not. However, exposure of the sediment to the atmosphere plays a role in the depth profile and concentration of sulfate and sulfide minerals present; for example, we noted an accumulation of pyrite far above the visibly reduced sediment layer, and barite precipitation deeper in the reduced layer. Furthermore, exposure of euxinic sediments to the atmosphere can facilitate oxidation of iron-sulfide minerals that create acidic conditions that negatively impact the carbonate minerals. Therefore, oxidation of euxinic sediments creates geochemical conditions that influence its bulk mineral composition. Euxinic conditions do not change the clay mineralogy of sediments, whether at the surface in contact with the atmosphere, on the time scale of 10's of thousands of years or at depth without direct contact with the atmosphere. Modern euxinic conditions do not change the octahedral chemical composition of smectite, thereby causing no change in its morphology. However, the interlayer chemical compositions of smectites are changed by modern euxinic conditions. Therefore,

smectite clay responds to a modern euxinic condition by interlayer cation exchange and immobilization of nanoprecipitates which reflect the chemistry of euxinic water. From this study it can be implied that Al-rich smectites would have responded to the widespread euxinia during the Proterozoic on early earth by cation exchange in their interlayer and by adsorption of available trace elements as sulfur minerals on their surface. However, the octahedral chemical compositions of smectite would have remained unchanged during ancient euxinic periods on Earth and possibly during the paleo-sulfidic period on Mars for 10's of thousands of years. Their stability for longer period requires further studies.

## Acknowledgements

We appreciate Lewis and Clark astrobiology fund for providing funds for the field work for this research, along with the Joe and Robert Klabzuba Chair and NASA grant 22-HW22_2-0005. We also thank Dani Storms for helping with the drone image of the study area.

## References


(1) Gilleaudeau, G. J.; Sahoo, S. K.; Ostrander, C. M.; Owens, J. D.; Poulton, S. W.; Lyons, T. W.; Anbar, A. D. Molybdenum Isotope and Trace Metal Signals in an Iron-Rich Mesoproterozoic Ocean: A Snapshot from the Vindhyan Basin, India. *Precambrian Res.* **2020**, *343*, 105718. https://doi.org/10.1016/j.precamres.2020.105718.

(2) Johnston, D. T.; Wolfe-Simon, F.; Pearson, A.; Knoll, A. H. Anoxygenic Photosynthesis Modulated Proterozoic Oxygen and Sustained Earth's Middle Age. *Proc. Natl. Acad. Sci.* **2009**, *106* (40), 16925–16929. https://doi.org/10.1073/pnas.0909248106.

(3) Gill, B. C.; Lyons, T. W.; Young, S. A.; Kump, L. R.; Knoll, A. H.; Saltzman, M. R. Geochemical Evidence for Widespread Euxinia in the Later Cambrian Ocean. *Nature* **2011**, *469* (7328), 80–83. https://doi.org/10.1038/nature09700.

(4) Hammarlund, E. U.; Dahl, T. W.; Harper, D. A. T.; Bond, D. P. G.; Nielsen, A. T.; Bjerrum, C. J.; Schovsbo, N. H.; Schönlaub, H. P.; Zalasiewicz, J. A.; Canfield, D. E. A Sulfidic Driver for the End-Ordovician Mass Extinction. *Earth Planet. Sci. Lett.* **2012**, *331–332*, 128–139. https://doi.org/10.1016/j.epsl.2012.02.024.

(5) Sperling, E. A.; Melchin, M. J.; Fraser, T.; Stockey, R. G.; Farrell, U. C.; Bhajan, L.; Brunoir, T. N.; Cole, D. B.; Gill, B. C.; Lenz, A.; Loydell, D. K.; Malinowski, J.; Miller, A. J.; Plaza-Torres, S.; Bock, B.; Rooney, A. D.; Tecklenburg, S. A.; Vogel, J. M.; Planavsky, N. J.; Strauss, J. V. A Long-Term Record of Early to Mid-Paleozoic Marine Redox Change. *Sci. Adv.* **2021**, *7* (28), eabf4382. https://doi.org/10.1126/sciadv.abf4382.

(6) Rickard, D. Euxinic Systems. In *Developments in Sedimentology*; Elsevier, 2012; Vol. 65, pp 495–542. https://doi.org/10.1016/B978-0-444-52989-3.00013-1.

(7) Robbins, L. J.; Lalonde, S. V.; Planavsky, N. J.; Partin, C. A.; Reinhard, C. T.; Kendall, B.; Scott, C.; Hardisty, D. S.; Gill, B. C.; Alessi, D. S.; Dupont, C. L.; Saito, M. A.; Crowe, S. A.; Poulton, S. W.; Bekker, A.; Lyons, T. W.; Konhauser, K. O. Trace Elements at the Intersection of Marine Biological and Geochemical Evolution. *Earth-Sci. Rev.* **2016**, *163*, 323–348. https://doi.org/10.1016/j.earscirev.2016.10.013.

(8) Catalano, J. G. Thermodynamic and Mass Balance Constraints on Iron-Bearing Phyllosilicate Formation and Alteration Pathways on Early Mars: Iron-Bearing Clay Formation Pathways. *J. Geophys. Res. Planets* **2013**, *118* (10), 2124–2136. https://doi.org/10.1002/jgre.20161.

(9) Cuadros, J.; Michalski, J. R. Investigation of Al-Rich Clays on Mars: Evidence for Kaolinite–Smectite Mixed-Layer versus Mixture of End-Member Phases. *Icarus* **2013**, *222* (1), 296–306. https://doi.org/10.1016/j.icarus.2012.11.006.

(10) DePasquale, B. M.; Jenkins, D. M. The Upper-Thermal Stability of an Iron-Rich Smectite: Implications for Smectite Formation on Mars. *Icarus* **2022**, *374*, 114816. https://doi.org/10.1016/j.icarus.2021.114816.

(11) Peretyazhko, T. S.; Sutter, B.; Morris, R. V.; Agresti, D. G.; Le, L.; Ming, D. W. Fe/Mg Smectite Formation under Acidic Conditions on Early Mars. *Geochim. Cosmochim. Acta* **2016**, *173*, 37–49. https://doi.org/10.1016/j.gca.2015.10.012.

(12) Peretyazhko, T. S.; Niles, P. B.; Sutter, B.; Morris, R. V.; Agresti, D. G.; Le, L.; Ming, D. W. Smectite Formation in the Presence of Sulfuric Acid: Implications for Acidic Smectite Formation on Early Mars. *Geochim. Cosmochim. Acta* **2018**, *220*, 248–260. https://doi.org/10.1016/j.gca.2017.10.004.

(13) Wang, Q.; Hu, Q.; Zhao, C.; Wang, Y.; Zhang, T.; Ilavsky, J.; Sun, M.; Zhang, L.; Shu, Y. Sample Size Effects on Petrophysical Characterization and Fluid-to-Pore Accessibility of Natural Rocks. *Nanomaterials* **2023**, *13* (10), 1651. https://doi.org/10.3390/nano13101651.

(14) Wang, Y. Nanogeochemistry: Nanostructures, Emergent Properties and Their Control on Geochemical Reactions and Mass Transfers. *Chem. Geol.* **2014**, *378–379*, 1–23. https://doi.org/10.1016/j.chemgeo.2014.04.007.

(15) Stucki, J. W. A Review of the Effects of Iron Redox Cycles on Smectite Properties. *Comptes Rendus Geosci.* **2011**, *343* (2–3), 199–209. https://doi.org/10.1016/j.crte.2010.10.008.

(16) Stucki, J. W. Properties and Behaviour of Iron in Clay Minerals. In *Developments in Clay Science*; Elsevier, 2013; Vol. 5, pp 559–611. https://doi.org/10.1016/B978-0-08-098258-8.00018-3.

(17) Stucki, J. W.; Lee, K.; Zhang, L.; Larson, R. A. Effects of Iron Oxidation State on the Surface and Structural Properties of Smectites. *Pure Appl. Chem.* **2002**.

(18) Nadeau, P. H. The Physical Dimensions of Fundamental Clay Particles. *Clay Miner.* **1985**, *20* (4), 499–514. https://doi.org/10.1180/claymin.1985.020.4.06.

(19) Kupper, R. J.; Zhou, N.; Chan, C. S.; Thompson, A.; Catalano, J. G. Oxidation Rates and Redox Stabilization of Ferrous Iron in Trioctahedral Smectites. *Geochim. Cosmochim. Acta* **2023**, *355*, 282–300. https://doi.org/10.1016/j.gca.2023.06.029.

(20) Lee, K.; Kostka, J. E.; Stucki, J. W. Comparisons of Structural Fe Reduction in Smectites by Bacteria and Dithionite: An Infrared Spectroscopic Study. *Clays Clay Miner.* **2006**, *54* (2), 195–208. https://doi.org/10.1346/CCMN.2006.0540205.

(21) Yang, S.; Liu, D.; Zheng, W.; Fan, Q.; Wang, H.; Zhao, L. Microbial Reduction and Alteration of Fe(III)-Containing Smectites in the Presence of Biochar-Derived Dissolved Organic Matter. *Appl. Geochem.* **2023**, *152*, 105661. https://doi.org/10.1016/j.apgeochem.2023.105661.

(22) Liu, D.; Wang, F.; Dong, H.; Wang, H.; Zhao, L.; Huang, L.; Wu, L. Biological Reduction of Structural Fe(III) in Smectites by a Marine Bacterium at 0.1 and 20MPa. *Chem. Geol.* **2016**, *438*, 1–10. https://doi.org/10.1016/j.chemgeo.2016.05.020.

(23) Wilson, J.; Cressey, G.; Cressey, B.; Cuadros, J.; Ragnarsdottir, K. V.; Savage, D.; Shibata, M. The Effect of Iron on Montmorillonite Stability. (II) Experimental Investigation. *Geochim. Cosmochim. Acta* **2006**, *70* (2), 323–336. https://doi.org/10.1016/j.gca.2005.09.023.

(24) Ferrage, E.; Lanson, B.; Sakharov, B. A.; Drits, V., A. Investigation of Smectite Hydration Properties by Modeling Experimental X-Ray Diffraction Patterns: Part I. Montmorillonite Hydration Properties. *Am. Mineral.* **2005**, *90* (8–9), 1358–1374. https://doi.org/10.2138/am.2005.1776.

(25) Laird, D. A. Influence of Layer Charge on Swelling of Smectites. *Appl. Clay Sci.* **2006**, *34* (1–4), 74–87. https://doi.org/10.1016/j.clay.2006.01.009.

(26) Morodome, S.; Kawamura, K. <I>In Situ</I> X-Ray Diffraction Study of the Swelling of Montmorillonite as Affected by Exchangeable Cations and Temperature. *Clays Clay Miner.* **2011**, *59* (2), 165–175. https://doi.org/10.1346/CCMN.2011.0590205.

(27) Wei, G.-Y.; Zhao, M.; Sperling, E. A.; Gaines, R. R.; Kalderon-Asael, B.; Shen, J.; Li, C.; Zhang, F.; Li, G.; Zhou, C.; Cai, C.; Chen, D.; Xiao, K.-Q.; Jiang, L.; Ling, H.-F.; Planavsky, N. J.; Tarhan, L. G. Lithium Isotopic Constraints on the Evolution of Continental Clay Mineral Factory and Marine Oxygenation in the Earliest Paleozoic Era. *Sci. Adv.* **2024**, *10* (13), eadk2152. https://doi.org/10.1126/sciadv.adk2152.

(28) Hazen, R. M.; Sverjensky, D. A.; Azzolini, D.; Bish, D. L.; Elmore, S. C.; Hinnov, L.; Milliken, R. E. Clay Mineral Evolution. *Am. Mineral.* **2013**, *98* (11–12), 2007–2029. https://doi.org/10.2138/am.2013.4425.

(29) Bishop, J. L.; Dobrea, E. Z. N.; McKeown, N. K.; Parente, M.; Ehlmann, B. L.; Michalski, J. R.; Milliken, R. E.; Poulet, F.; Swayze, G. A.; Mustard, J. F.; Murchie, S. L.; Bibring, J.-P. Phyllosilicate Diversity and Past Aqueous Activity Revealed at Mawrth Vallis, Mars. *Science* **2008**, *321* (5890), 830–833. https://doi.org/10.1126/science.1159699.

(30) Chemtob, S.; Nickerson, R.; Morris, R.; Agresti, D.; Catalano, J. Oxidative Alteration of Ferrous Smectites and Implications for the Redox Evolution of Early Mars: Oxidation Products of Ferrous Smectites. *J. Geophys. Res. Planets* **2017**, *122*. https://doi.org/10.1002/2017JE005331.

(31) Bibring, J.-P.; Langevin, Y.; Mustard, J. F.; Poulet, F.; Arvidson, R.; Gendrin, A.; Gondet, B.; Mangold, N.; Pinet, P.; Forget, F.; Berthé, M.; Bibring, J.-P.; Gendrin, A.; Gomez, C.; Gondet, B.; Jouglet, D.; Poulet, F.; Soufflot, A.; Vincendon, M.; Combes, M.; Drossart, P.; Encrenaz, T.; Fouchet, T.; Merchiorri, R.; Belluci, G.; Altieri, F.; Formisano, V.; Capaccioni, F.; Cerroni, P.; Coradini, A.; Fonti, S.; Korablev, O.; Kottsov, V.; Ignatiev, N.; Moroz, V.; Titov, D.; Zasova, L.; Loiseau, D.; Mangold, N.; Pinet, P.; Douté, S.; Schmitt, B.; Sotin, C.; Hauber, E.; Hoffmann, H.; Jaumann, R.; Keller, U.; Arvidson, R.; Mustard, J. F.; Duxbury, T.; Forget, F.; Neukum, G. Global Mineralogical and Aqueous Mars History Derived from OMEGA/Mars Express Data. *Science* **2006**, *312* (5772), 400–404. https://doi.org/10.1126/science.1122659.

(32) Bishop, J. L.; Loizeau, D.; McKeown, N. K.; Saper, L.; Dyar, M. D.; Des Marais, D. J.; Parente, M.; Murchie, S. L. What the Ancient Phyllosilicates at Mawrth Vallis Can Tell Us about Possible Habitability on Early Mars. *Planet. Space Sci.* **2013**, *86*, 130–149. https://doi.org/10.1016/j.pss.2013.05.006.

(33) Jain, N.; Chauhan, P. Study of Phyllosilicates and Carbonates from the Capri Chasma Region of Valles Marineris on Mars Based on Mars Reconnaissance Orbiter-Compact Reconnaissance Imaging Spectrometer for Mars (MRO-CRISM) Observations. *Icarus* **2015**, *250*, 7–17. https://doi.org/10.1016/j.icarus.2014.11.018.

(34) King, P. L.; McLennan, S. M. Sulfur on Mars. *Elements* **2010**, *6* (2), 107–112. https://doi.org/10.2113/gselements.6.2.107.

(35) Carter, J.; Poulet, F.; Bibring, J.-P.; Mangold, N.; Murchie, S. Hydrous Minerals on Mars as Seen by the CRISM and OMEGA Imaging Spectrometers: Updated Global View: Hydrous Minerals on Mars: Global View. *J. Geophys. Res. Planets* **2013**, *118* (4), 831–858. https://doi.org/10.1029/2012JE004145.

(36) Boyle, R. A.; Clark, J. R.; Poulton, S. W.; Shields-Zhou, G.; Canfield, D. E.; Lenton, T. M. Nitrogen Cycle Feedbacks as a Control on Euxinia in the Mid-Proterozoic Ocean. *Nat. Commun.* **2013**, *4* (1), 1533. https://doi.org/10.1038/ncomms2511.

(37) Koeksoy, E.; Sundman, A.; Byrne, J. M.; Lohmayer, R.; Planer-Friedrich, B.; Halevy, I.; Konhauser, K. O.; Kappler, A. Formation of Green Rust and Elemental Sulfur in an Analogue for Oxygenated Ferro-Euxinic Transition Zones of Precambrian Oceans. *Geology* **2019**, *47* (3), 211–214. https://doi.org/10.1130/G45501.1.

(38) Lyons, T. W. Ironing Out Ocean Chemistry at the Dawn of Animal Life. *Science* **2008**, *321* (5891), 923–924. https://doi.org/10.1126/science.1162870.

(39) Senko, J. M.; Campbell, B. S.; Henriksen, J. R.; Elshahed, M. S.; Dewers, T. A.; Krumholz, L. R. Barite Deposition Resulting from Phototrophic Sulfide-Oxidizing Bacterial Activity. *Geochim. Cosmochim. Acta* **2004**, *68* (4), 773–780. https://doi.org/10.1016/j.gca.2003.07.008.

(40) Sanders, W. E. Rate and Mechanism of Barite Mineralization at Zodletone Mountain, Southwestern Oklahoma. PhD Thesis, University of Oklahoma, 1998.

(41) Bachman, E. E.; Hullaster, D.; Krumholz, L. R.; Elwood Madden, A. S. Biotic and Abiotic Mineralogical Signatures Induced by Euxinic Methane-Rich Brine Spring Discharge; 2018; p 324175. https://doi.org/Geological Society of America Abstracts with Programs. Vol. 50, No. 6 10.1130/abs/2018AM-324175.

(42) Younger, P. L. Barite Travertine from Southwestern Oklahoma and West - Central Colorado. **1984**. https://doi.org/Unpublished Masters thesis.

(43) Widanagamage; Waldron, A.; Glamoclija, M. Controls on Barite Crystal Morphology during Abiotic Precipitation. *Minerals* **2018**, *8* (11), 480. https://doi.org/10.3390/min8110480.

(44) Widanagamage; Griffith, E. M.; Singer, D. M.; Scher, H. D.; Buckley, W. P.; Senko, J. M. Controls on Stable Sr-Isotope Fractionation in Continental Barite. *Chem. Geol.* **2015**, *411*, 215–227. https://doi.org/10.1016/j.chemgeo.2015.07.011.

(45) Savage, K. N.; Krumholz, L. R.; Gieg, L. M.; Parisi, V. A.; Suflita, J. M.; Allen, J.; Philp, R. P.; Elshahed, M. S. Biodegradation of Low-Molecular-Weight Alkanes under Mesophilic, Sulfate-Reducing Conditions: Metabolic Intermediates and Community Patterns: N-Propane and n-Pentane Degradation by Sulfate Reducers. *FEMS Microbiol. Ecol.* **2010**, *72* (3), 485–495. https://doi.org/10.1111/j.1574-6941.2010.00866.x.

(46) Kettler, T. A.; Doran, J. W.; Gilbert, T. L. Simplified Method for Soil Particle-Size Determination to Accompany Soil-Quality Analyses. *Soil Sci. Soc. Am. J.* **2001**, *65* (3), 849–852. https://doi.org/10.2136/sssaj2001.653849x.

(47) Moore, D. M.; Reynolds, R. C., Jr. *X-Ray Diffraction and the Identification and Analysis of Clay Minerals*, 2nd ed.; Oxford University Press, 1997.

(48) Bonny, S. M.; Jones, B. Controls on the Precipitation of Barite (BaSO4) Crystals in Calcite Travertine at Twitya Spring, a Warm Sulphur Spring in Canada's Northwest Territories. *Sediment. Geol.* **2008**, *203* (1–2). https://doi.org/10.1016/j.sedgeo.2007.10.003.

(49) Benning, L. G.; Wilkin, R. T.; Barnes, H. L. Reaction Pathways in the Fe–S System below 100°C. *Chem. Geol.* **2000**, *167* (1–2), 25–51. https://doi.org/10.1016/S0009-2541(99)00198-9.

(50) Peiffer, S.; Behrends, T.; Hellige, K.; Larese-Casanova, P.; Wan, M.; Pollok, K. Pyrite Formation and Mineral Transformation Pathways upon Sulfidation of Ferric Hydroxides Depend on Mineral Type and Sulfide Concentration. *Chem. Geol.* **2015**, *400*, 44–55. https://doi.org/10.1016/j.chemgeo.2015.01.023.

(51) Rickard, D. Sedimentary Pyrite. In *Developments in Sedimentology*; Elsevier, 2012; Vol. 65, pp 233–285. https://doi.org/10.1016/B978-0-444-52989-3.00006-4.

(52) Schoonen, M. A. A.; Barnes, H. L. Reactions Forming Pyrite and Marcasite from Solution: II. Via FeS Precursors below 100°C. *Geochim. Cosmochim. Acta* **1991**. https://doi.org/10.1016/0016-7037(91)90123-M.

(53) Wilkin, R.; Barnes, H. Pyrite Formation in an Anoxic Estuarine Basin. *Am. J. Sci.* **1997**, *297* (6), 620–650. https://doi.org/10.2475/ajs.297.6.620.

(54) Amils, R.; González-Toril, E.; Fernández-Remolar, D.; Gómez, F.; Aguilera, Á.; Rodríguez, N.; Malki, M.; García-Moyano, A.; Fairén, A. G.; de la Fuente, V.; Luis Sanz,

J. Extreme Environments as Mars Terrestrial Analogs: The Rio Tinto Case. *Planet. Space Sci.* **2007**, *55* (3), 370–381. https://doi.org/10.1016/j.pss.2006.02.006.

(55) Battler, M. M.; Osinski, G. R.; Lim, D.; Davila, A. F.; Michel, F. A.; Craig, M. A.; Izawa, M.; Leoni, L.; Slater, G. F.; Fairén, A. G.; Preston, L. J.; Banerjee, N. R. Characterization of the Acidic Cold Seep Emplaced Jarositic Golden Deposit, NWT, Canada, as an Analogue for Jarosite Deposition on Mars. *Icarus* **2013**, *224* (2). https://doi.org/10.1016/j.icarus.2012.05.015.

(56) Cruells, M.; Roca, A. Jarosites: Formation, Structure, Reactivity and Environmental. *Metals* **2022**, *12* (5), 802. https://doi.org/10.3390/met12050802.

(57) Zolotov, M. Y.; Shock, E. L. Formation of Jarosite-bearing Deposits through Aqueous Oxidation of Pyrite at Meridiani Planum, Mars. *Geophys. Res. Lett.* **2005**, *32* (21), 2005GL024253. https://doi.org/10.1029/2005GL024253.

(58) Benison, K. C.; Bowen, B. B. Extreme Sulfur-Cycling in Acid Brine Lake Environments of Western Australia. *Chem. Geol.* **2013**, *351*, 154–167. https://doi.org/10.1016/j.chemgeo.2013.05.018.

(59) Geyer, C.; Elwood Madden, A. S.; Rodriguez, A.; Bishop, J. L.; Mason, D.; Elwood Madden, M. The Role of Sulfate in Cation Exchange Reactions: Applications to Clay–Brine Interactions on Mars. *Planet. Sci. J.* **2023**, *4* (3), 48. https://doi.org/10.3847/PSJ/acba97.

(60) Liu, X.; Li, A.; Dong, J.; Zhuang, G.-C.; Xu, F.; Wan, S. Nonevaporative Origin for Gypsum in Mud Sediments from the East China Sea Shelf. *Mar. Chem.* **2018**, *205*, 90–97. https://doi.org/10.1016/j.marchem.2018.08.009.

(61) Zhang, F.; Xu, H.; Konishi, H.; Kemp, J. M.; Roden, E. E.; Shen, Z. Dissolved Sulfide-Catalyzed Precipitation of Disordered Dolomite: Implications for the Formation Mechanism of Sedimentary Dolomite. *Geochim. Cosmochim. Acta* **2012**, *97*, 148–165. https://doi.org/10.1016/j.gca.2012.09.008.

(62) Warthmann, R.; Van Lith, Y.; Vasconcelos, C.; McKenzie, J. A.; Karpoff, A. M. Bacterially Induced Dolomite Precipitation in Anoxic Culture Experiments. *Geology* **2000**, *28* (12), 1091. https://doi.org/10.1130/0091-7613(2000)28<1091:BIDPIA>2.0.CO;2.

(63) Deng, S.; Dong, H.; Lv, G.; Jiang, H.; Yu, B.; Bishop, M. E. Microbial Dolomite Precipitation Using Sulfate Reducing and Halophilic Bacteria: Results from Qinghai Lake,

Tibetan Plateau, NW China. *Chem. Geol.* **2010**, *278* (3–4), 151–159. https://doi.org/10.1016/j.chemgeo.2010.09.008.

(64) Roberts, J. A.; Kenward, P. A.; Fowle, D. A.; Goldstein, R. H.; González, L. A.; Moore, D. S. Surface Chemistry Allows for Abiotic Precipitation of Dolomite at Low Temperature. *Proc. Natl. Acad. Sci.* **2013**, *110* (36), 14540–14545. https://doi.org/10.1073/pnas.1305403110.

(65) Baldermann, A.; Deditius, A. P.; Dietzel, M.; Fichtner, V.; Fischer, C.; Hippler, D.; Leis, A.; Baldermann, C.; Mavromatis, V.; Stickler, C. P.; Strauss, H. The Role of Bacterial Sulfate Reduction during Dolomite Precipitation: Implications from Upper Jurassic Platform Carbonates. *Chem. Geol.* **2015**, *412*, 1–14. https://doi.org/10.1016/j.chemgeo.2015.07.020.

(66) Baritantonaki, A.; Bolourinejad, P.; Herber, R. Dolomite Dissolution Rates at Conditions Relevant to CO2 Sequestration in the Rotliegend Gas Fields in NE Netherlands; Celle, Germany, 2015. https://doi.org/10.3997/2214-4609.201414270.

(67) Debure, M.; Andreazza, P.; Canizarès, A.; Grangeon, S.; Lerouge, C.; Mack, P.; Madé, B.; Simon, P.; Veron, E.; Warmont, F.; Vayer, M. Study of Iron-Bearing Dolomite Dissolution at Various Temperatures: Evidence for the Formation of Secondary Nanocrystalline Iron-Rich Phases on the Dolomite Surface. *ACS Earth Space Chem.* **2017**, *1* (7), 442–454. https://doi.org/10.1021/acsearthspacechem.7b00073.

(68) Saldi, G. D.; Causserand, C.; Schott, J.; Jordan, G. Dolomite Dissolution Mechanisms at Acidic pH: New Insights from High Resolution pH-Stat and Mixed-Flow Reactor Experiments Associated to AFM and TEM Observations. *Chem. Geol.* **2021**, *584*, 120521. https://doi.org/10.1016/j.chemgeo.2021.120521.

(69) Dazas, B.; Lanson, B.; Delville, A.; Robert, J.-L.; Komarneni, S.; Michot, L. J.; Ferrage, E. Influence of Tetrahedral Layer Charge on the Organization of Interlayer Water and Ions in Synthetic Na-Saturated Smectites. *J. Phys. Chem. C* **2015**, *119* (8), 4158–4172. https://doi.org/10.1021/jp5123322.

(70) Marty, N. C. M.; Grangeon, S.; Lassin, A.; Madé, B.; Blanc, P.; Lanson, B. A Quantitative and Mechanistic Model for the Coupling between Chemistry and Clay Hydration. *Geochim. Cosmochim. Acta* **2020**, *283*, 124–135. https://doi.org/10.1016/j.gca.2020.05.029.

(71) Mohamed Salah, K.; Robert, J. L. Hydration Behaviour of Synthetic Saponite at Variable Relative Humidity. *Bull. Mater. Sci.* **2011**, *34* (6), 1263–1266. https://doi.org/10.1007/s12034-011-0244-8.

(72) Ehrmann, W.; Setti, Massimo; Marinoni, Luigi. Clay Minerals in Cenozoic Sediments off Cape Roberts (McMurdo Sound, Antarctica) Reveal Palaeoclimatic History, 2005.

(73) Setti, M.; Marinoni, L.; López-Galindo, A. Crystal-Chemistry of Smectites in Sediments of CRP-3 Drillcore (Victoria Land Basin, Antartica): Preliminary Results, Terra Antartica, Bremerhaven. *PANGAEA 2001 8 4 Pp 543-550 Hdl10013epic28222d001* **2001**, *PANGAEA, 2001, 8 (4)*, 543-550.

(74) Iacoviello, F.; Giorgetti, G.; Nieto, F.; Memmi, I. T. Evolution with Depth from Detrital to Authigenic Smectites in Sediments from AND-2A Drill Core (McMurdo Sound, Antarctica). *Clay Miner.* **2012**, *47* (4), 481–498. https://doi.org/10.1180/claymin.2012.047.4.07.

(75) Latta, D. E.; Neumann, A.; Premaratne, W. A. P. J.; Scherer, M. M. Fe(II)–Fe(III) Electron Transfer in a Clay Mineral with Low Fe Content. *ACS Earth Space Chem.* **2017**, *1* (4), 197–208. https://doi.org/10.1021/acsearthspacechem.7b00013.

(76) Kennedy, M.; Droser, M.; Mayer, L. M.; Pevear, D.; Mrofka, D. Late Precambrian Oxygenation; Inception of the Clay Mineral Factory. *Science* **2006**, *311* (5766), 1446–1449. https://doi.org/10.1126/science.1118929.

**Supporting Information for Chapter 1**

Table S1: STEM-EDX result of impacted creek sediment (ICS) smectite. Reported values for all EDX data in this manuscript are in weight percent.

| O | Na | Mg | Al | Si | S | K | Ca | Fe | Sr | Ba | Ti |
|---|---|---|---|---|---|---|---|---|---|---|---|
| 62.84 | 2.00 | 1.25 | 6.99 | 16.00 | 1.59 | 0.17 | 1.18 | 1.84 | 0.67 | 5.47 | 0.00 |
| 64.81 | 3.03 | 1.80 | 6.88 | 15.53 | 0.58 | 0.15 | 1.50 | 1.83 | 0.14 | 3.57 | 0.00 |
| 63.03 | 0.79 | 1.58 | 9.63 | 21.23 | 0.00 | 0.36 | 0.52 | 2.77 | 0.00 | 0.00 | 0.00 |
| 67.32 | 1.60 | 1.31 | 8.45 | 18.14 | 0.00 | 0.19 | 1.07 | 1.93 | 0.00 | 0.00 | 0.00 |
| 64.87 | 2.06 | 1.36 | 7.67 | 15.00 | 1.43 | 0.25 | 0.92 | 1.55 | 0.19 | 4.71 | 0.00 |
| 59.78 | 1.00 | 2.32 | 10.50 | 20.55 | 0.00 | 0.46 | 0.07 | 5.31 | 0.00 | 0.00 | 0.00 |
| 61.12 | 1.07 | 1.32 | 12.17 | 21.39 | 0.00 | 0.58 | 0.26 | 2.09 | 0.00 | 0.00 | 0.00 |
| 57.57 | 1.69 | 2.98 | 11.36 | 20.16 | 0.00 | 1.10 | 0.52 | 4.63 | 0.00 | 0.00 | 0.00 |
| 60.15 | 0.00 | 1.74 | 10.87 | 24.10 | 0.00 | 0.37 | 0.19 | 2.59 | 0.00 | 0.00 | 0.00 |
| 61.14 | 0.47 | 1.09 | 8.88 | 25.19 | 0.00 | 0.79 | 0.40 | 2.04 | 0.00 | 0.00 | 0.00 |
| 67.86 | 1.00 | 1.38 | 8.08 | 17.51 | 0.78 | 0.48 | 0.67 | 2.13 | 0.00 | 0.00 | 0.12 |

Table S2: STEM-EDX result of impacted soil layer sediment (ISL) smectite.

| **O** | **Na** | **Mg** | **Al** | **Si** | **S** | **K** | **Ca** | **Fe** | **Sr** | **Ba** | **Ti** | **Cr** | **Mn** |
|---|---|---|---|---|---|---|---|---|---|---|---|---|---|
| 26.84 | 1.55 | 1.64 | 13.94 | 43.53 | 0.67 | 0.65 | 0.94 | 9.60 | 0.00 | 0.00 | 0.20 | 0.00 | 0.00 |
| 35.46 | 1.10 | 1.55 | 15.43 | 37.06 | 0.72 | 0.89 | 0.81 | 5.86 | 0.00 | 0.00 | 0.23 | 0.00 | 0.00 |
| 36.49 | 0.75 | 1.66 | 15.46 | 41.42 | 0.00 | 0.27 | 0.33 | 2.90 | 0.00 | 0.00 | 0.26 | 0.00 | 0.00 |
| 28.01 | 1.00 | 1.74 | 18.11 | 37.00 | 1.24 | 0.56 | 0.97 | 3.22 | 0.36 | 7.79 | 0.00 | 0.00 | 0.00 |
| 34.11 | 1.40 | 1.22 | 16.61 | 40.2 | 0.70 | 0.51 | 1.08 | 3.68 | 0.00 | 0.00 | 0.00 | 0.00 | 0.00 |
| 48.70 | 0.60 | 1.66 | 13.1 | 30.79 | 0.00 | 0.53 | 0.33 | 3.84 | 0.00 | 0.00 | 0.19 | 0.00 | 0.00 |
| 50.19 | 0.57 | 2.58 | 15.74 | 25.75 | 0.14 | 0.4 | 0.45 | 4.18 | 0.00 | 0.00 | 0.00 | 0.00 | 0.00 |
| 50.65 | 0.12 | 3.97 | 14.53 | 25.56 | 0.00 | 0.17 | 0.15 | 4.72 | 0.00 | 0.00 | 0.12 | 0.05 | 0.07 |
| 54.21 | 1.08 | 3.17 | 10.49 | 21.86 | 0.47 | 0.92 | 0.41 | 4.97 | 0.12 | 2.18 | 0.10 | 0.00 | 0.00 |
| 48.91 | 1.00 | 2.55 | 15.53 | 28.62 | 0.00 | 0.32 | 0.32 | 5.74 | 0.00 | 0.00 | 0.00 | 0.00 | 0.00 |
| 50.55 | 0.50 | 1.42 | 13.9 | 25.93 | 0.00 | 0.17 | 0.15 | 6.32 | 0.00 | 0.00 | 0.06 | 0.00 | 0.00 |
| 58.18 | 0.69 | 2.44 | 11.29 | 22.67 | 0.00 | 0.52 | 0.58 | 3.57 | 0.00 | 0.00 | 0.03 | 0.00 | 0.00 |
| 56.59 | 1.12 | 2.21 | 12.05 | 22.59 | 0.00 | 0.78 | 0.55 | 3.52 | 0.00 | 0.00 | 0.13 | 0.00 | 0.00 |
| 54.25 | 1.02 | 2.93 | 10.15 | 21.26 | 0.75 | 1.1 | 0.62 | 5.01 | 0.13 | 2.50 | 0.11 | 0.00 | 0.00 |
| 45.81 | 0.72 | 5.93 | 15.39 | 25.72 | 0.00 | 0.46 | 0.23 | 5.12 | 0.00 | 0.00 | 0.12 | 0.00 | 0.00 |

Table S3: STEM-EDX result of unimpacted creek sediment (UCS) smectite.

| **O** | **Mg** | **Al** | **Si** | **K** | **Ca** | **Fe** | **Ti** |
|---|---|---|---|---|---|---|---|
| 67.08 | 2.25 | 6.77 | 17.41 | 0.93 | 2.25 | 3.31 | 0.00 |
| 66.83 | 2.20 | 7.29 | 16.55 | 1.10 | 2.61 | 3.41 | 0.00 |
| 66.44 | 2.32 | 7.02 | 17.06 | 1.13 | 2.36 | 3.66 | 0.00 |
| 67.29 | 2.38 | 6.97 | 16.84 | 0.96 | 2.40 | 3.16 | 0.00 |
| 66.97 | 2.21 | 7.00 | 17.10 | 1.00 | 2.38 | 3.33 | 0.00 |
| 68.65 | 2.36 | 6.30 | 15.23 | 1.05 | 2.80 | 3.62 | 0.00 |
| 68.93 | 2.15 | 6.18 | 15.16 | 1.02 | 3.61 | 2.94 | 0.00 |
| 68.18 | 2.14 | 6.73 | 16.12 | 1.31 | 2.42 | 3.10 | 0.00 |
| 69.34 | 2.12 | 6.12 | 14.72 | 1.01 | 3.77 | 2.92 | 0.00 |
| 67.59 | 2.32 | 6.77 | 16.02 | 1.11 | 2.64 | 3.55 | 0.00 |
| 66.85 | 2.45 | 6.66 | 16.26 | 1.04 | 2.78 | 3.95 | 0.00 |
| 66.85 | 2.45 | 6.66 | 16.26 | 1.04 | 2.78 | 3.95 | 0.00 |
| 68.20 | 2.11 | 6.29 | 15.22 | 1.08 | 3.21 | 3.89 | 0.00 |
| 69.67 | 2.16 | 6.63 | 15.73 | 0.83 | 1.85 | 3.12 | 0.00 |
| 69.11 | 2.28 | 6.38 | 15.44 | 0.86 | 2.62 | 3.29 | 0.00 |
| 69.01 | 2.32 | 6.35 | 15.99 | 1.07 | 2.02 | 3.16 | 0.09 |
| 68.29 | 2.22 | 6.39 | 15.58 | 1.07 | 3.20 | 3.24 | 0.00 |
| 68.22 | 2.23 | 6.57 | 16.16 | 1.15 | 2.19 | 3.38 | 0.10 |
| 67.28 | 2.21 | 6.61 | 16.48 | 1.15 | 2.90 | 3.26 | 0.11 |

Table S4: STEM-EDX result of unimpacted soil layer sediment (USL) smectite.

| **O** | **Mg** | **Al** | **Si** | **K** | **Ca** | **Fe** | **Ti** |
|---|---|---|---|---|---|---|---|
| 51.63 | 1.41 | 11.75 | 28.52 | 0.70 | 0.48 | 5.42 | 0.10 |
| 48.82 | 1.97 | 11.86 | 31.69 | 0.27 | 0.81 | 4.50 | 0.08 |
| 53.08 | 1.59 | 11.40 | 27.92 | 0.44 | 0.66 | 3.92 | 0.99 |
| 49.99 | 2.06 | 10.01 | 33.27 | 0.42 | 0.32 | 3.81 | 0.13 |
| 56.96 | 1.01 | 9.25 | 29.85 | 0.27 | 0.27 | 2.38 | 0.00 |
| 45.32 | 0.78 | 11.99 | 30.45 | 0.28 | 0.40 | 10.20 | 0.59 |
| 47.02 | 1.83 | 10.91 | 29.52 | 0.28 | 0.43 | 9.88 | 0.13 |
| 43.06 | 1.91 | 12.70 | 34.86 | 0.56 | 0.50 | 6.41 | 0.00 |
| 57.23 | 1.16 | 11.59 | 29.79 | 0.62 | 1.97 | 2.77 | 0.00 |
| 52.07 | 1.34 | 10.51 | 30.80 | 0.31 | 1.34 | 3.62 | 0.00 |
| 46.12 | 1.60 | 14.20 | 28.95 | 0.32 | 0.37 | 10.02 | 0.42 |
| 44.67 | 0.70 | 14.72 | 29.58 | 0.14 | 0.44 | 9.19 | 0.56 |
| 45.83 | 1.15 | 13.31 | 27.60 | 0.38 | 0.84 | 10.58 | 0.31 |

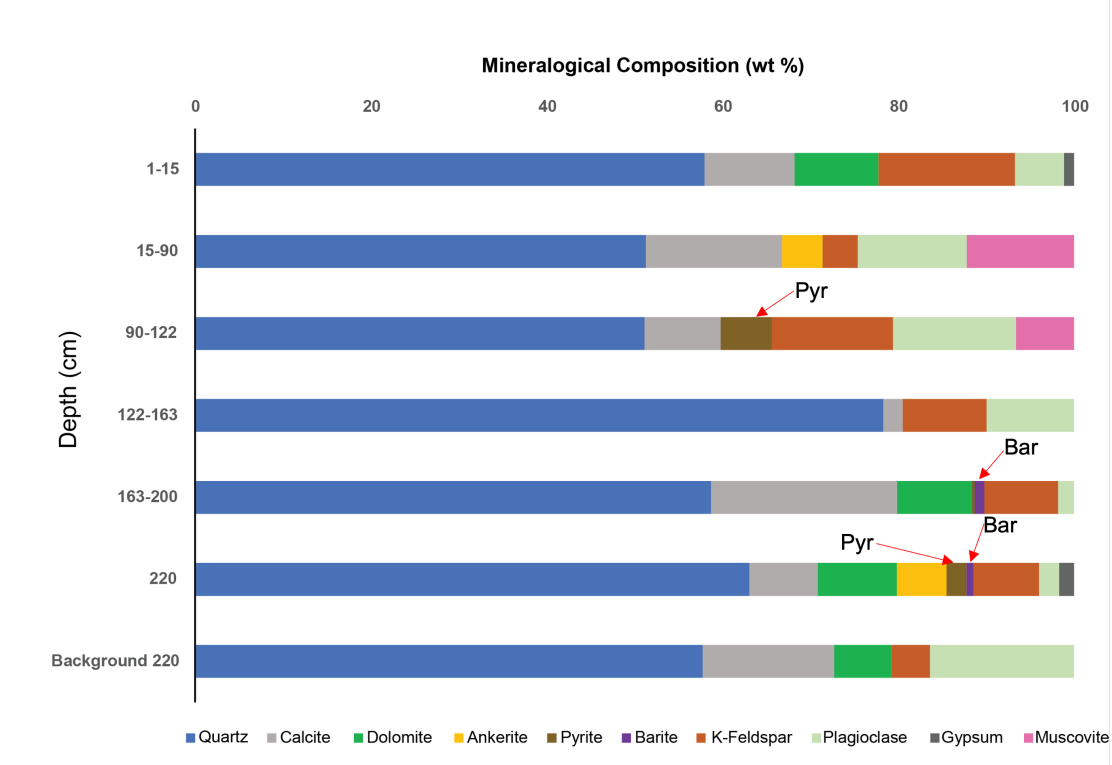


Figure S1: Bulk mineralogy of soil profile reported as weight percent, where impacted soil layer (ISL) is at 220 cm depth.

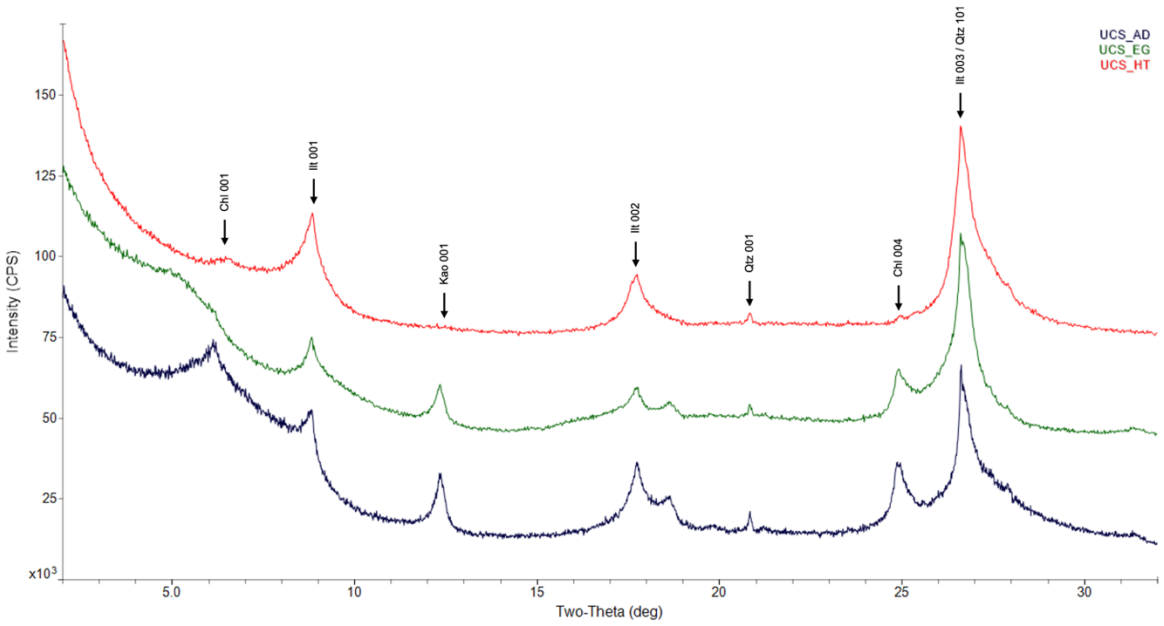


Figure S2: Clay mineralogy of UCS; Air-dried (dark blue scan), Ethylene glycol-treated (green scan) and Heat treated (red scan).

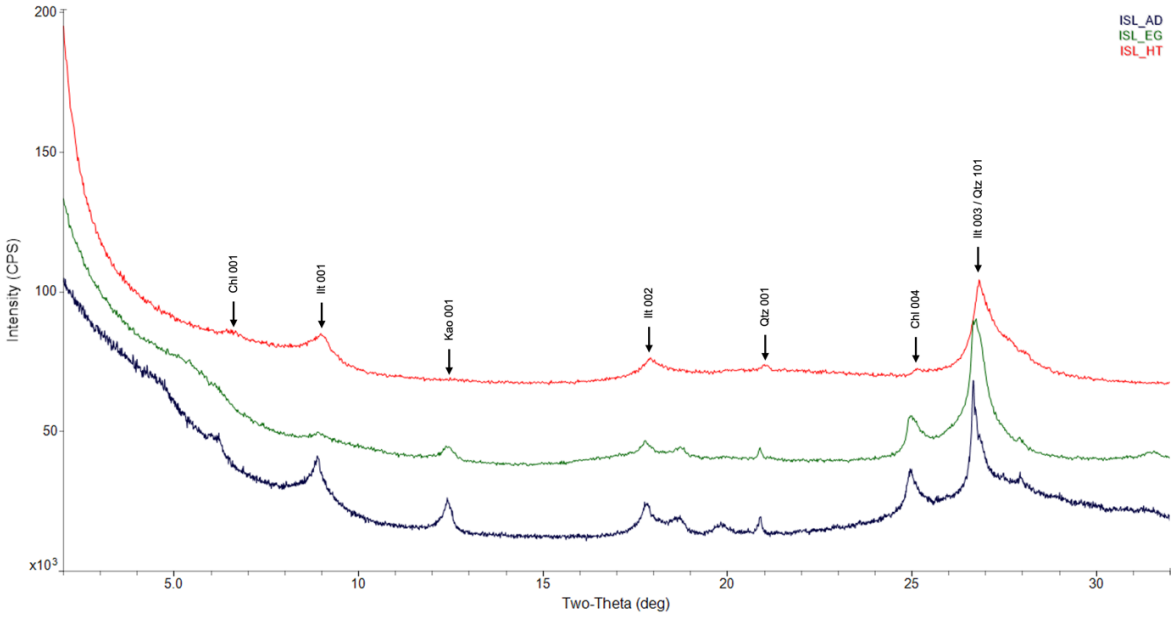


Figure S3: Clay mineralogy of ISL; Air-dried (dark blue scan), Ethylene glycol-treated (green scan) and Heat treated (red scan).

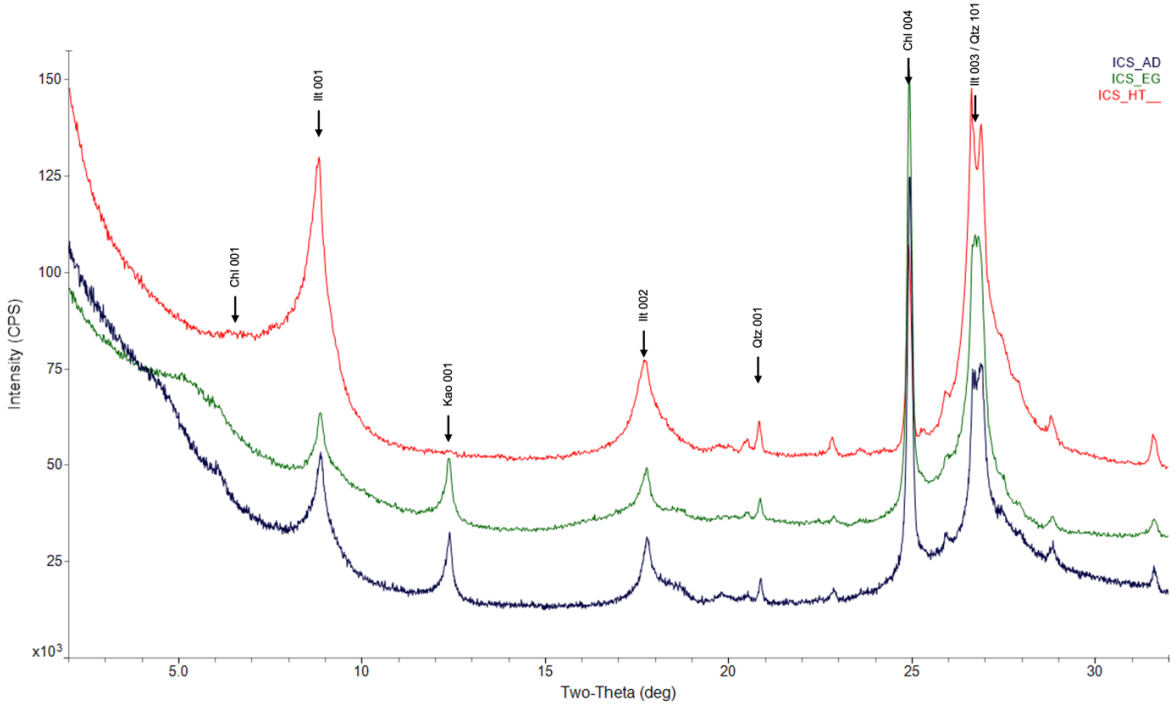


Figure S4: Clay mineralogy of ICS; Air-dried (dark blue scan), Ethylene glycol-treated (green scan) and Heat treated (red scan).

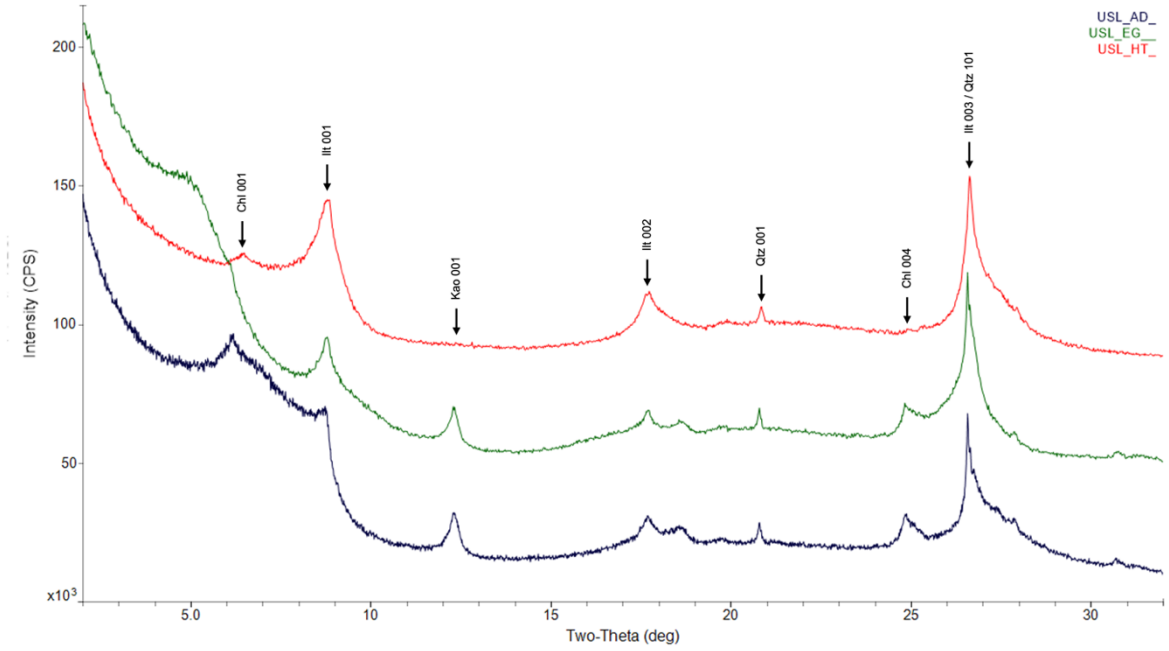


Figure S5: Clay mineralogy of USL; Air-dried (dark blue scan), Ethylene glycol-treated (green scan) and Heat treated (red scan).

Figure S6: Picture of precipitated surficial jarosite above the ICS sampling point.

# Chapter 2: Responses of smectite octahedral sheet composition to euxinic conditions

Itunu T. Apalara[1*], Caitlin Hodges[1], Julian E. C. Sabisch[2], Megan E. Elwood Madden[1], Preston R. Larson[2], Andrew S. Elwood Madden[1,2]

[1]School of Geosciences, University of Oklahoma, Norman, OK 73019, USA

[2]Samuel Roberts Noble Microscopy Laboratory, University of Oklahoma, Norman, OK 73019, USA

## Abstract

Changes in redox conditions cause physical, morphological and chemical changes in minerals including Fe-rich smectite clays. Transitions from oxic to euxinic conditions are examples of one such redox change. Much of ancient Earth history is recorded in and interpreted from sediments deposited from euxinic (sulfide-rich) waters, where the evolution of clay chemistry is poorly understood. However, modern euxinic environments are useful proxies for early Earth and potentially sulfur bearing extra-terrestrial bodies such as Mars. Therefore, we sought to understand the morphological and chemical changes recorded in smectites with varying octahedral sheet composition after reacting with euxinic (anoxic and sulfidic) conditions. We investigated the reaction of SWa-1 (Fe-rich smectite) and SAz-1 (Al-rich smectite) with a modern euxinic spring over a period of 504 hours. We used a combination of Transmission Electron Microcopy and Scanning/ Transmission Electron Microcopy coupled with energy dispersive spectroscopy (TEM-EDX), and Xray Diffraction Analysis (XRD). Our results show that SWa-1 underwent progressive reductive dissolution of Fe, accompanied by color change from yellow to black under sulfidic and anoxic condition. The dissolution was followed by secondary Fe-sulfide and $S^0$ precipitation. However, SAz-1 showed remarkable stability of its aluminosilicate framework despite minor Fe loss. SAz-1 also accumulated some $S^0$ and barite but in lesser quantity when compared to the reduced SWa-1. TEM analysis shows morphological alterations i.e. curling and folding of clay edges in reduced SWa-1 while no noticeable difference is seen in the morphology of Al-smectite SAz-1 throughout the experiment. The observed cation exchange trend in reacted SAz-1 is $Ca^{2+} > K^+ > Na^+$, which aligns with known smectite cation exchange hierarchies under certain conditions; however, the transition from $Na^+$ to $Ca^{2+}$ interlayer dominance in SWa-1 after reductive dissolution highlights the role of kinetic limitations in natural systems. We demonstrate that octahedral sheet

composition governs the extent of smectite alteration under natural reducing conditions. Our findings show that Fe-rich clay minerals would have been unstable on the early earth and could explain the partial dissolution of Fe-rich smectites observed by rover and orbiter missions on Mars.

## 2.0 Introduction

Clay minerals are important components of biogeochemical cycling of metals and nutrients in the environment. Although it is widely recognized that clays are important sorbents for organic and inorganic constituents and are critical for determining the physical, chemical, and hydrologic properties of soils and sediments, less attention is often given to their responses to fluctuations in redox conditions[1,2].

One of the common groups of clay minerals capable of redox activity is the smectite group. Smectite clay structure includes an octahedral sheet sandwiched between two tetrahedral sheets[3–5], known as a "2:1" structure. The octahedral sheet is usually composed of major elements Al, Mg, and Fe, often in combinations of two or all of them. This causes variations such as tri or di-octahedral sheet occupancy[34]. The tetrahedral sheet is usually composed of Si with some trace or major incorporation of Al. The composition of the octahedral sheet influences the properties of the clay, such as cation exchange capacity, layer charge and swelling behavior. These properties make smectite play an important role in nutrient cycling and storage of paleo elemental cycling signals.

Fe-rich smectites are sensitive to redox changes and have been widely studied in the laboratory[6–18]. The redox reactivity of smectites is directly linked to its iron content and oxidation state[3,17–19]. Redox changes affect some of Fe-rich smectites' properties such as color, cation exchange capacity and swelling ability. Fe atoms in Fe-rich smectite are mostly located in the octahedral sheet[3,17–21]. This octahedral Fe is called structural iron, in contrast with any 'exchangeable' iron found in the

interlayer, and could either be Fe(II), or Fe(III), or both[18,22]. The reduction or oxidation of structural Fe can be biotically or abiotically mediated[3,17–20]. A variety of bacteria are able to reduce structural Fe(III) in Fe-rich smectite[18,20,23]. Furthermore, chemical reagents such as dithionite, sulfide and benzidine can reduce structural Fe(III). In fact, Stucki et. al (1996) demonstrated that the potency of sulfide in reducing Fe(III) to Fe(II) in Fe-rich smectite is only second to dithionite when compared with other reducing agents. The reduction of Fe(III) in Fe-rich clays also increases its layer charge, causing an increase in cation exchange capacity, which is crucial to smectite's ability to immobilize trace elements in the environment [3,17,24,25].

Al-rich smectite on the other hand is believed to be less sensitive to redox changes because the octahedral sheet is dominated by redox-stable $Al^{3+}$. The Al–O bond is strong compared to the Fe-O bond in ferruginous smectites[21]. This makes dissolution or structural changes difficult in Al-rich smectites under neutral pH conditions. A previous study of clay minerals exposed to modern euxinic conditions demonstrated that detrital Al – rich smectites only responded to euxinic (sulfidic and anoxic) conditions by cation exchange in the interlayer and adsorption of sulfur bearing minerals on their edges, over a period of tens of thousands of years[26]. There was no significant change in the Al-smectite octahedral sheet composition of the smectite exposed to the euxinic (sulfidic and anoxic) aqueous environment.

In order to better understand the processes prevalent on the early Earth and extra-terrestrial bodies such as Mars, modern terrestrial analogous environments such as modern euxinic environments are scientific research hotspots. Modern euxinic environments are natural laboratories to study geochemical proxies from interactions between smectite and euxinic conditions. These extreme conditions were prevalent in the early Earth ocean. The time range being the early to mid-Proterozoic[27,28], lasting for about 1Ga with more episodes in the later Cambrian[29], the end

Ordovician[30] up to the mid – early Devonian[31]. Recently, the ability to send sophisticated orbiting and lander/rover spacecraft to other planetary bodes increased attention on studying origins of life and astrobiology, including the exploration of habitability on Mars[32,33]. On Earth, sulfidic and anoxic environments such as hydrothermal vents host extremophiles who have special adaptation mechanisms to survive such extreme conditions[34,35]. These extremophiles are believed to have been prevalent on the early Earth before oxygenic photosynthesis became dominant[34,35]. Therefore, studying euxinic environments gives us insight into the limits of life and where life can exist. Furthermore, Fe-Mg smectite, Al-rich smectites and sulfate minerals occur on Mars[36–38]. The presence of these minerals on Mars could be indicative of aqueous alteration of regolith and therefore environments favorable to life[36,39].

While previous studies have investigated the interactions of sulfide with smectite and its effect on smectite properties in the laboratory, the understanding of this interaction in the natural modern euxinic environment is limited. Therefore, in this study, we investigated the effect of octahedral sheet composition on smectite reactivity in a modern euxinic spring. We hypothesize that octahedral sheet cations (e.g., Al vs. Fe/Mg) will control smectite response to euxinic conditions. We expect mechanisms such as ion exchange, redox reactions, and structural reconfiguration to be more pronounced in the Fe-rich smectite. We use electron microscopy coupled with energy dispersive X-ray spectroscopy, X-ray diffraction and geochemical modeling for the investigation. Our study aims to advance the scientific understanding of clay behavior in natural extreme environments, with implications for understanding the reactivity of Fe-rich and Al-rich smectites on the early euxinic Earth and potentially Mars.

## 2.1 Study Area

The study site is an anoxic and sulfidic spring called the Zodletone spring, located in southwest Oklahoma. This spring is located within the Cambrian-Ordovician Slick Hills of the oil-producing Anadarko basin. Zodletone spring is rich in sulfide (8-10 mM) and major cations[40–42] (Table 1), fed by deep basinal brines. The spring has no detectable oxygen with a pH of 7.1. Hydrocarbon gases such as methane and propane gas bubbles out of the spring, which is believed to have also been sourced from the deeply buried hydrocarbons[42]. Complex biogeochemical activities such as microbial sulfur cycling have been reported at this site[40,43].

Table 1: Major ion concentrations in Zodletone spring water[41]

| Element | Concentration (ppm) | Concentration (mmol / kg) |
|---|---|---|
| $Na^+$ | 2800 | 121.8 |
| $Ca^{2+}$ | 320 | 7.98 |
| $Mg^{2+}$ | 150 | 6.17 |
| $Ba^{2+}$ | 67 | 0.49 |
| $K^+$ | 27 | 0.69 |
| $Sr^{2+}$ | 19 | 0.22 |
| $S^{2-}$ | 139 | 4.02 |
| $Cl^-$ | 6160 | 173.8 |
| $HCO_3^-$ | 481 | 7.88[44] |
| Fe | 0.5 | 0.0090 |

## 2.2 Sampling and Methods

### 2.2.1 Field Sampling

Two different clay standard material from the Clay Mineral Society were used for this study. One is dioctahedral Al-rich smectite (montmorillonite, SAz-1) and the other is dioctahedral Fe-rich smectite (SWa-1). Both clays were gently disaggregated using the agate mortar and pestle. The disaggregated clays were soaked in ultra-pure water (UPW) at a ratio of about 15 g : 200 ml for about 24 hours in order to remove non-clay materials. A set of both clays were saturated with $Na^+$ at a ratio of 1 g of clay / 10 ml of 1 M NaCl solution. A total of 15 g of each clay was allowed to equilibrate with the Na solution for 3 days, then rinsed four times with ultrapure water. The rinsed samples were transferred into dialysis bags and were deployed into the euxinic spring for 8 hours. Another set of the clays were prepared without equilibrating with $Na^+$ and deployed into the euxinic spring for 5 days (120 hours). A third set was prepared and deployed for 3 weeks (504 hours). Finally, sets of each clay with and without homogenizing with $Na^+$ were reserved to serve as controls for the experiment and were not reacted with the euxinic spring.

Reacted clays were retrieved into canning jars from the euxinic spring under strict anaerobic conditions. Anaerobic canning jars were prepared in the laboratory. Jars were opened in an anaerobic chamber (97:3 $N_2$:$H_2$), equilibrated, and sealed for transport to the field. For sampling, the sealed jars were immersed into the spring and opened below the water surface, as the spring water itself has no detectable dissolved oxygen. Without exposure to the atmosphere, the dialysis tubes with reacted clays were tucked into the jars and closed. The samples were transported back to the lab on dry ice and were transferred immediately to the freezer. The frozen samples were freeze dried. After the 3 weeks experiment, two different size populations developed. We separated the size fractions by sieving through a 0.42 mm sieve. Finer fractions are hereafter labeled SWa-

1_A and SAz-1 (A) while coarser fractions are labeled SWa-1_B and SAz-1 (B). All samples were kept in an anaerobic chamber prior to analysis.

### 2.2.2 Laboratory study

#### 2.2.2.1 Electron microscopy

The freeze dried smectite clays were prepared for electron microscopy by dispersion in methanol and pipetting directly onto a lacey carbon copper grid. Samples were analyzed for morphology and semi-quantitative chemical composition using Transmission Electron Microscopy (TEM) and Scanning/Transmission Electron Microscopy coupled with energy dispersive X-ray spectroscopy (STEM-EDX). Analysis was done using a JEOL 2010F TEM with a Schottky field-emission source at 200 kV and an Oxford EDS X-ray detector. Analytical correction was done using the Cliff Lorimer method-computed K-factor. Smectite nanoparticles are identified based on their elemental composition, morphology, and electron diffraction pattern.

#### 2.2.2.2 X-ray diffraction

About 2 mL of reacted and unreacted Swa-1 and SAz-1 were disaggregated using the agate mortar and pestle in the anaerobic chamber to minimize oxidation. The disaggregated samples were randomly mounted on glass slides. Bulk powder X-ray diffraction (XRD) analysis was done using a Rigaku SmartLab 9 kW diffractometer using Cu-K-alpha radiation (45 kV, 250 mA). Data analysis was completed using Jade Pro software with the American Mineralogist Crystal Structure Database[45].

## 2.3 Safety statement

No unexpected or unusually high safety hazards were encountered.

## 2.4 Results

### 2.4.1 Color

Unreacted Fe-rich smectite SWa-1 has a yellowish color while unreacted Al-rich smectite SAz-1 has a whitish color. However, the color of SWa-1 changes from yellow to pale green after 5 hours in the spring and further changed to a deep blue-greenish color after 8 hours (Figure 1). Furthermore, after both the 120 hours and the 504 hours reaction in the spring, the color changed to a completely black color. SAz-1 on the other hand, only had a slight change of color after 504 hours of reaction time in the euxinic spring.

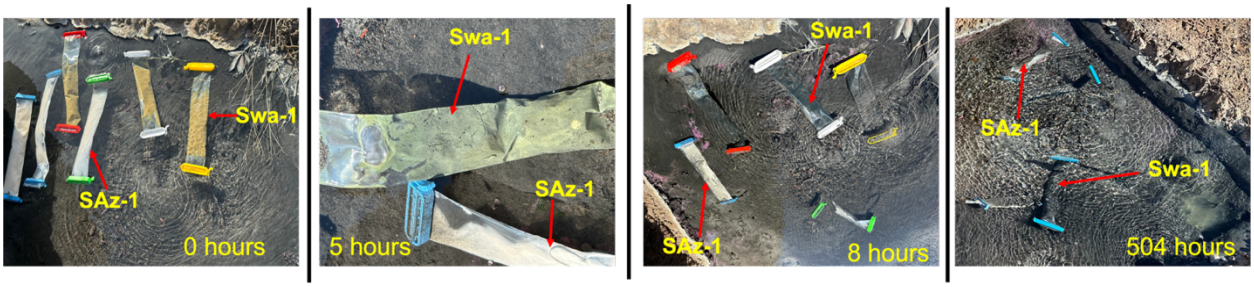


Figure 1: Smectite color change with respect to reaction time in the spring. Only Fe-rich SWa-1 shows intense color change with increasing reaction time.

### 2.4.2 Smectite morphology

We used TEM bright field imaging to study the changes in smectite morphology before and after interaction with the euxinic spring. Both SWa-1 and SAz-1 have a flat, platy morphology (Figure 2). However, after 504 hours, two different size populations were noticed in SWa-1, reflecting the development of coarse particles. We labeled fine fraction as SWa-1_A while the coarse fraction is labeled as SWa-1_B (Figure 3). TEM analysis of both sets of particles SWa-1_A and SWa-1_B showed similar morphology (Figure 4) to each other, but differences compared to the unreacted material. They both showed more folded, curled and denser edges after reaction (Figure 2). In TEM bright field images, areas with thicker or denser mass and/or lattice planes oriented for

diffraction scatter more electrons and therefore, fewer electrons are transmitted through, making that area darker in the image. Generally, darker regions in these images can be interpreted as areas with greater thickness.  SAz-1 on the other hand has no noticeable change in morphology.

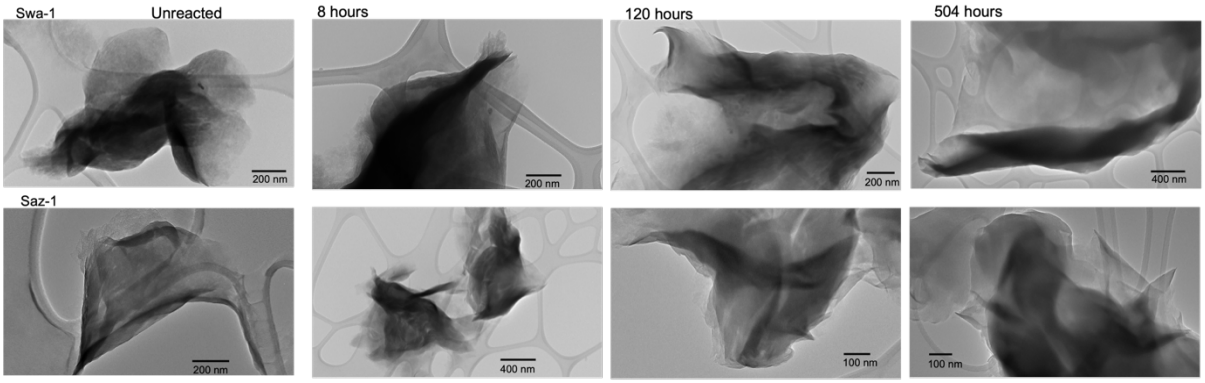


Figure 2: Smectite morphology change with respect to interaction with euxinic spring

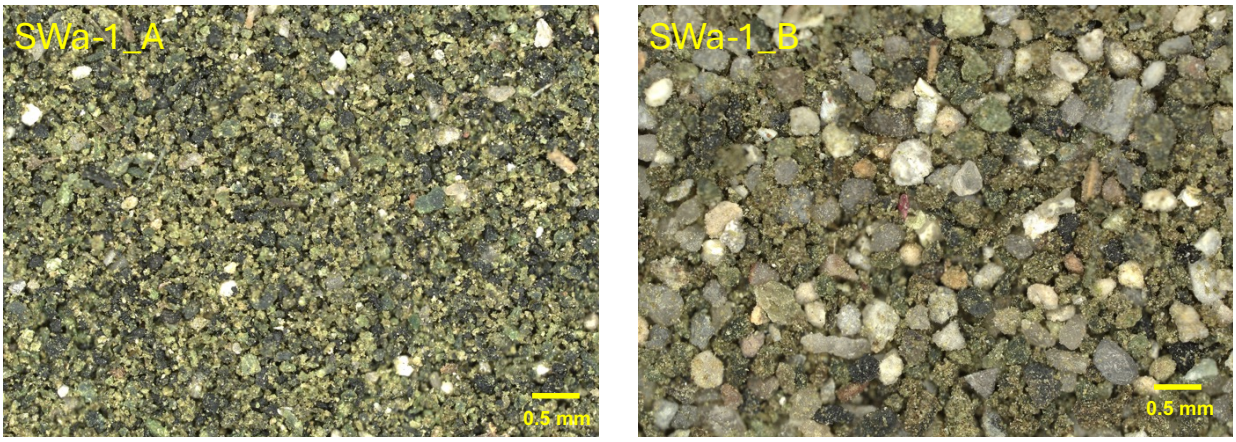


Figure 3: Ultramicroscope image of SWa-1_A and SWa-1_B showing their grain size difference

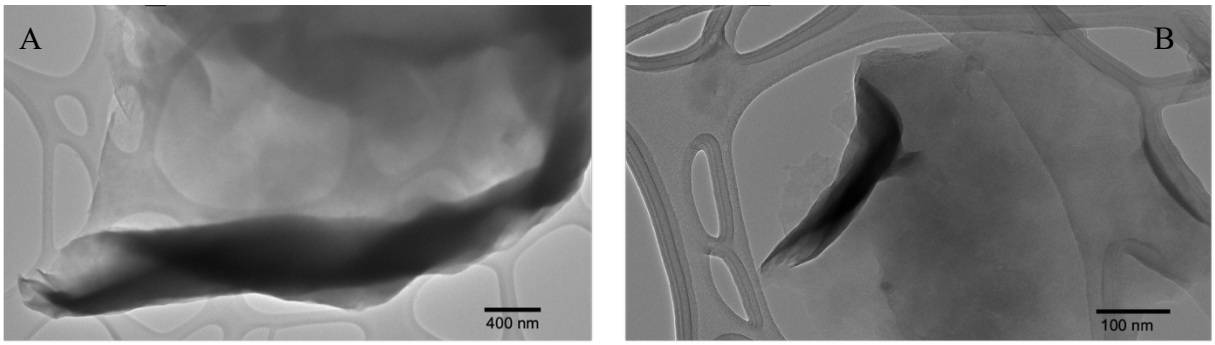


Figure 4: TEM images comparing smectite morphology in SWa-1_A and SWa_1_B

### 2.4.3 Smectite chemical composition

The elemental composition of individual smectite nanoparticles were determined using TEM-EDX and STEM-EDX. The EDX system is capable of detecting elements with atomic number ≥ 4 (not H, He, Li, or Be). Unreacted SWa-1 grains contain O, Fe, Si, Al, Mg, Ti, Ca; Na was also present in the set treated with NaCl. After 8 hours in the spring, S, Na, K, Ba and Sr concentrations increased compared to the initial composition, while the average concentration of Al, Si and Fe decreased. After 120 hours, the average concentrations of Fe, Al and Si decreased even further. At the end of 504 hours, two different populations of data were seen. The first population of particles (SWa-1_A) contains the same elements as the samples collected after 8 and 120 hours; however, the concentration of Si, Al, Fe and Mg in this set is less than the concentration in unreacted SWa-1 but slightly higher than the result from 120 hours (Figure 5a-5d). The second set of particles (SWa-1_B) are coarse and they contain almost 70 wt.% Fe with only trace amounts of Al, Si, Mg, Ca, K and Na, compared with about 15 wt.% Fe in the SWa-1_ A population.

Unreacted SAz-1 grains on the other hand contain O, Al, Si, Mg, Fe, Ti, K, and Ca, as well as Na in the set treated with NaCl. After 120 hours, trace amounts of Sr and Ba were added without S, however after 504 hours in the euxinic spring, no S, Ba or Sr was detected. It is noteworthy that,

throughout the experiment, the average concentration of Fe in SAz-1 decreased with increasing reaction time (Figure 5d).

In SWa-1, Na initially dominated the interlayer because the clays were homogenized with Na before deploying them into the spring. After the first 8 hours, Na, Ca, K, concentration increased while Na is still dominating the interlayer. Also, Ba and Sr were introduced in the first 8 hours. However, after 120 hours, the concentration of K increased slightly while the concentration of Sr and Ba decreased slightly. After 504 hours, Na concentration decreased significantly, Ba, Sr and K continued to decrease, and Ca became the dominant cation in the interlayer by the end of 504 hours (Figure 6a).

However, in SAz-1, the interlayer chemistry was initially dominated by Na followed by Ca, after 8 hours, Na concentration decreased drastically and K and Ca became dominant while traces of Ba and Sr were introduced, after 120 hours Na gained dominance again while the concentration of Ba and Sr also increased. By the end of 504 hours of reaction in the spring, Na became the dominant cation, followed by Ca, while K is occurring in trace concentration, and Ba and Sr are totally absent (Figure 6b).

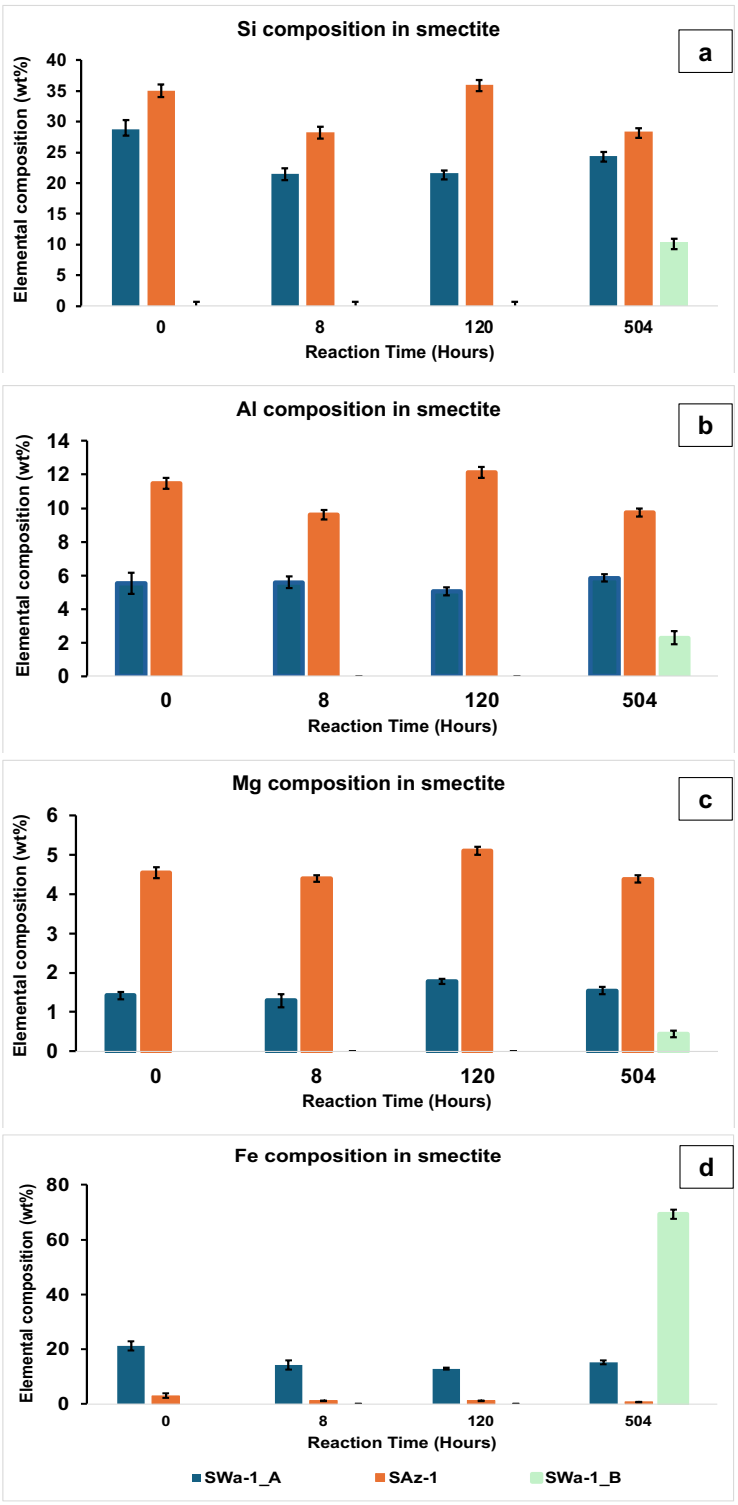


Figure 5 (a-c): Octahedral sheet composition changes in reacted clays with varying time

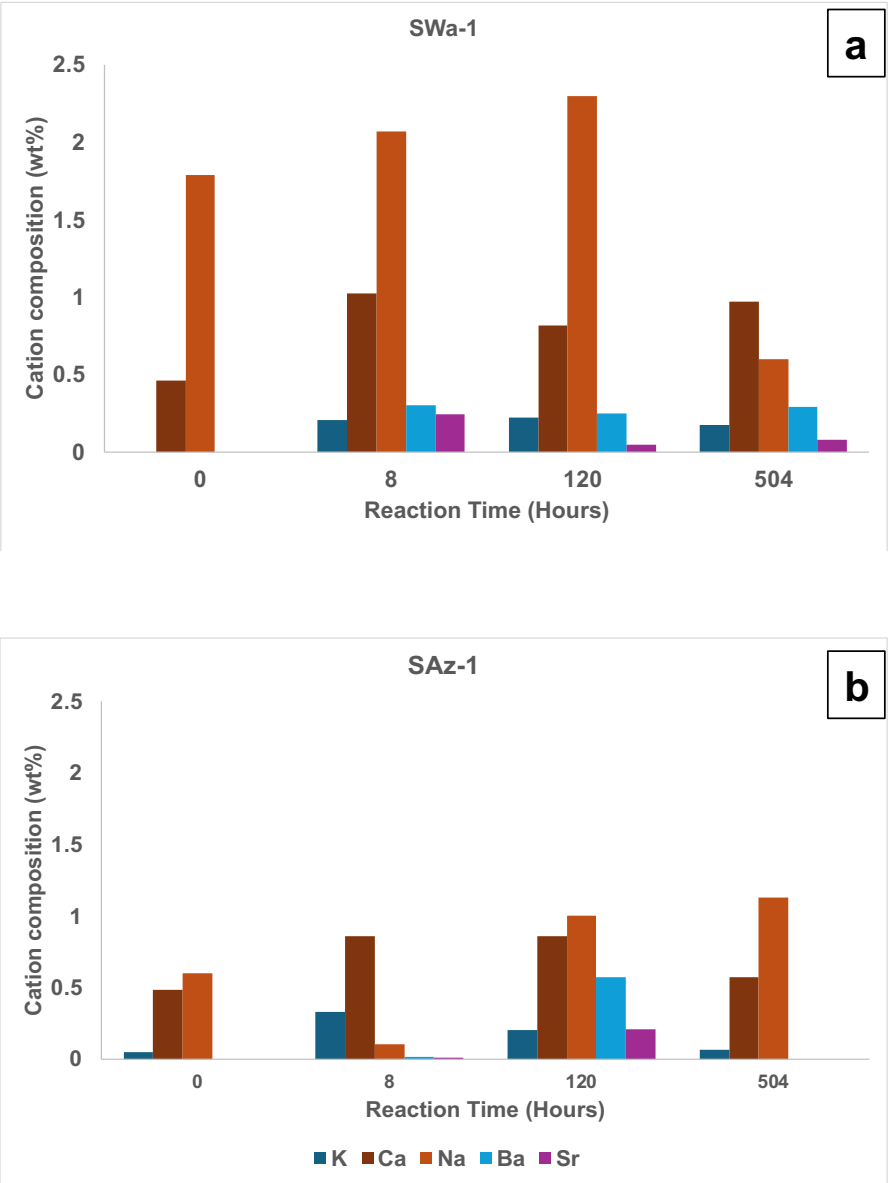


Figure 6 (a-b): Interlayer cation trend in reacted Al-rich smectite over the reaction time

### 2.4.4 X-ray diffraction Analysis

XRD results show peak shift from 14.7 Å in unreacted SWa-1 to 12.8 Å in reacted SWa-1_A and reacted SWa-1_B after 504 hours (3 weeks) reaction in the euxinic spring (Figure 7a). Additionally, new peaks were observed in reacted SWa-1 A and SWa-1_B. Peaks at 5.90 Å, 3.96 Å, 3.80 Å, 3.24 Å, and 2.14 Å in both SWa-1_A and SWa-1_B, all corresponds to elemental sulfur, while the peaks

at 3.16 Å, 3.04 Å, 2.93 Å, 2.08 Å and 1.92 Å in SWa-1_A and SWa-1_B corresponds to pyrite. We also decided to sieve the reacted SAz-1 after 504 hours using a 0.42 mm size sieve. The smaller fraction is SAz-1(A) and larger fraction is SAz-1 (B). In both size fractions; SAz-1 (A and B), we saw a peak shift from 15.20 Å in unreacted SAz-1 to 13.96 Å after 504 hours of reaction in the spring. The peak shape also changed from sharp to a broader structure (Figure 7b). Additional tiny peaks were also noticed at 5.90 Å, 3.96 Å, 3.80 Å, 3.24 Å, and 2.14 Å for elemental sulfur with peaks at 3.32 Å and 2.91 Å for barite.

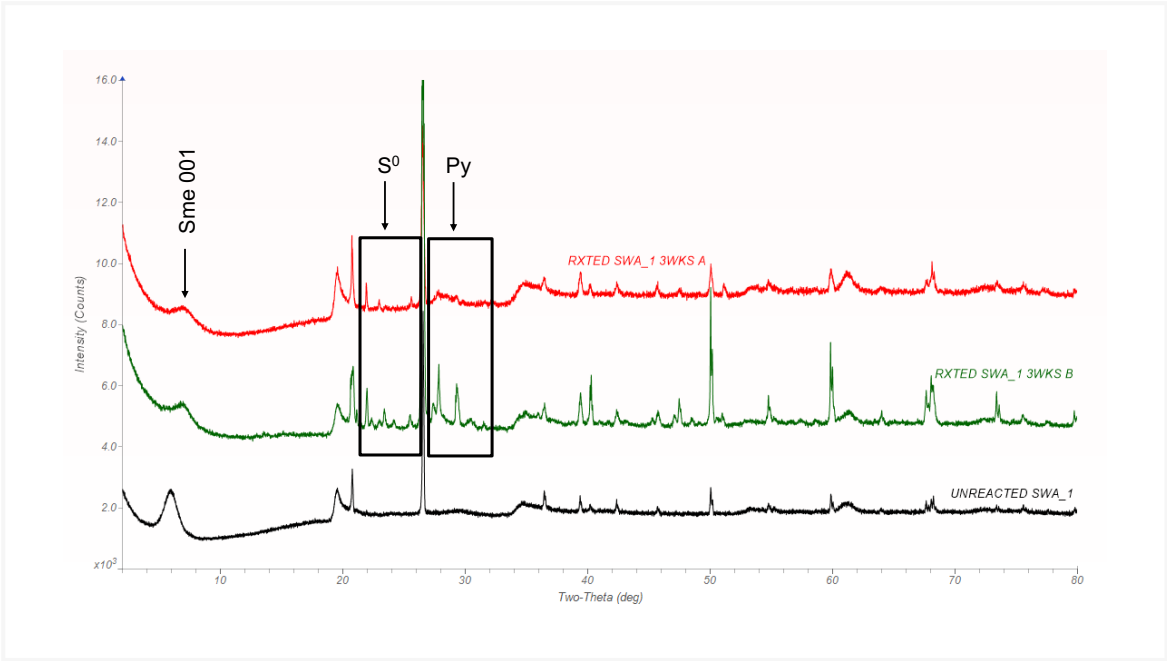


Figure 7a: Comparison between XRD analysis of unreacted Fe-rich smectite and reacted Fe-rich smectite SWa-1 (A and B) after 504 hours showing SWa-1 001 reflection changes and new precipitated phases.

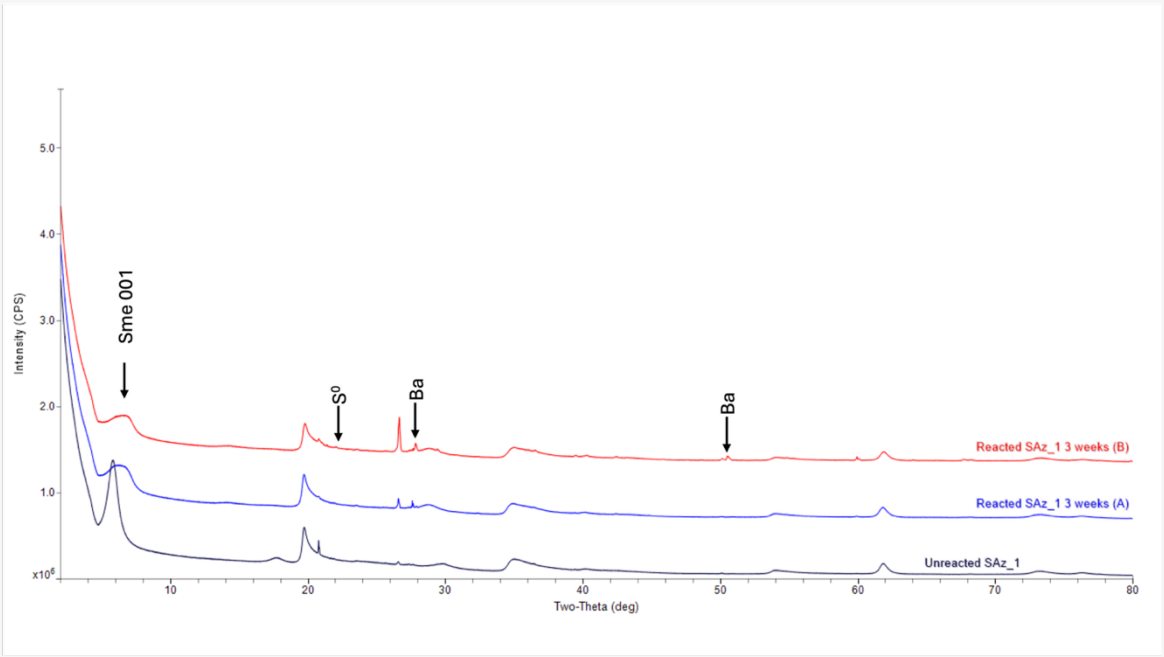


Figure 7b: Comparison between XRD analysis of unreacted Al-rich smectite and reacted Al-rich smectite (A and B) after 504 hours showing SAz-1 001 reflection changes and new precipitated phases.

## 2.5 Discussion

### 2.5.1 Effect of euxinic condition on smectite color

Previous studies have shown color changes when structural Fe in Fe rich smectite is reduced[19,46]. Stucki (2011) explained that the color change from orange to blue-green is because of electron transfer from Fe(III) to other species, resulting in absorbance in the visible spectrum from 700 to 750 nm. These changes have been observed in laboratory[19] studies and are now observed in this study in a natural reducing, sulfidic and anoxic environment. However, in the field samples, even darker coloration appears distinct from the lab studies likely due to the additional formation of iron sulfide associated with the clay. The Al-rich smectite did not experience intense color change as the color remained white even after 3 weeks of reaction with the spring.

### 2.5.2 Evidence of Fe-reduction and smectite dissolution

The reaction of the clays with the euxinic spring for the duration of 8 hours, 120 hours and 504 hours produced significant observations especially in SWa-1. In addition to TEM spot analyses, STEM-EDX mapping showed there is a significant change in the clay composition after interacting with the euxinic spring water (Figure 8). The decrease in smectite Al and Si concentrations with increasing reaction time suggests the reduction of structural Fe in the octahedral sheet leading to the dissolution and leaching of these elements under euxinic conditions. The euxinic spring is rich in sulfide, therefore the reduction of structural ferric iron is facilitated chiefly by the presence of sulfide. This observation aligns with previous studies demonstrating that reducing environments promote the destabilization of aluminosilicate minerals by creating a charge imbalance and facilitating the breakdown of Si-O and Al-O bonds[16,46–51]. Biogenic Fe reduction could also be possible within the dialysis bag (32 mm diameter and molecular weight cutoff (MWCO) of 6-8 kDa). Microorganisms are capable of releasing electron shuttling molecules or Fe chelators for Fe-reduction. While this is possible, we do not expect it to be a major contributor to Fe-reduction in this experiment because previous studies have shown that this form of Fe-reduction only contributed 2 to 3% of the reduction process[124].

The continuous decrease in Fe content over time (Figure 5d) indicates reductive dissolution, where Fe(III) in the smectite structure is reduced to more soluble Fe(II) and subsequently released into solution. This process is well-documented in previous laboratory experiments[3,9,16,19,20,52] that mimic sulfidic environments, where sulfide ($HS^-$) acts as a strong reductant, driving the dissolution of Fe-bearing clays. However, the formation of secondary Fe-rich minerals (>70% Fe) (SWa-1_B) with minimal Al and Si after 504 hours suggests a shift from dissolution to Fe reprecipitation. The near absence of Al and Si in these secondary phases implies that Fe was preferentially sequestered,

likely as Fe-sulfides[53] (e.g., mackinawite, pyrite) or Fe-(oxyhydr)oxides (possibly due to partial oxidation during sampling and analysis). The dominance of Fe in the secondary minerals supports the hypothesis that under prolonged sulfidic conditions, Fe(II) reacts with residual sulfide to form stable Fe-sulfides, while Al and Si remain in solution or form amorphous aluminosilicate residues[51]. Because the coarser fraction is much thicker, the data may be biased towards Fe and O/S signals may be preferentially absorbed by the thick crystal. This is because as sample thickness increases, the probability of X-rays generated by lighter elements to be absorbed by heavier elements increases, causing the concentration of heavier elements to be exaggerated and lighter elements to be underestimated[54,55]. The persistence of smectite in the XRD pattern suggests incomplete dissolution, consistent with studies showing that Fe(III)-rich clays can undergo partial reduction while retaining their layered structure[19].

On the other hand, SAz-1 (Al-rich smectite) after reacting with the euxinic spring for 504 hours revealed distinct geochemical behavior of the major structural elements (Al, Si, and Fe). The TEM-EDX results showed remarkable stability of aluminum and silicon concentrations throughout the experimental duration, while iron exhibited progressive decrease. These observations show the differential reactivity of smectite components under reducing, anoxic and sulfidic conditions. The stability of Al and Si concentrations in the SAz-1 may be attributed to the fact that Al is not sensitive to redox changes, therefore there is no option of electron transfer from the sulfide to the clay making SAz-1 less susceptible to reductive dissolution compared to SWa-1. However, the continuous decrease of iron, despite its presumably low initial concentration in this Al-rich smectite, suggests that iron exists in more labile forms within the structure, potentially in the clay interlayer[19]. This observation aligns with studies showing that Fe(III) in smectite is particularly susceptible to reductive dissolution (Stucki, 2011). The reduction process likely proceeded through

electron transfer from sulfide species to structural Fe(III), followed by release of Fe(II) into solution[56]. The persistence of the aluminosilicate framework of SAz-1 suggests that Al-rich smectites may maintain their structural integrity and cation exchange capacity longer than Fe-rich varieties under similar reducing conditions[26].

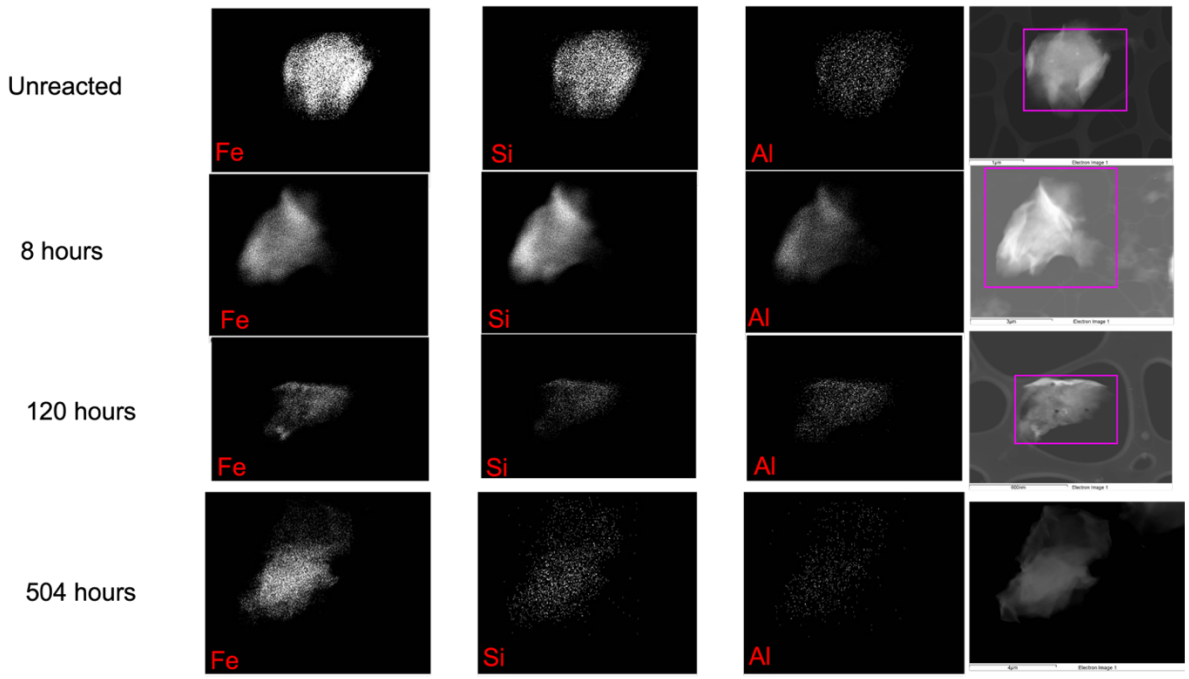


Figure 8: STEM-EDX analysis showing loss of Si and Al in reacted SWa-1 with reaction time (504 hours scan is from SWa-1_B).

### 2.5.3 Impact of euxinic condition on smectite interlayer composition

There are significant interlayer composition shifts in the reacted clays, suggesting competitive cation exchange, The rapid response to surrounding aqueous chemistry could be related to the total amount and location of layer charge in both clays. Due to Coulomb's law, the strength of interaction is proportional to the total layer charge and proximity of the negative layer charge to the positively charged interlayer cations. The layer charge is located in the octahedral sheet in

SAz-1, making the bond between negatively charged layer and the interlayer cations weaker than in SWa-1, where the initial layer charge is located in the tetrahedral sheet.

In SAz-1, the interlayer was initially dominated by Na. However, the rapid decline of Na and the concurrent rise in K and Ca within the first 8 hours suggest preferential uptake of these cations under early reaction conditions. The strong affinity of SAz-1 for Ca over Na during the first 8 hours is well-documented due to higher charge density and stronger electrostatic interactions of Ca with the negatively charged clay layers[57,58]. The introduction of K may indicate initial competitive absorption, as K can effectively compete for interlayer sites due to its low hydration energy, facilitating partial collapse of smectite layers[59,60]. The appearance of trace Ba and Sr suggests their initial availability in the euxinic spring, with smectite exhibiting a short-term uptake before their subsequent release.

By 504 hours, the interlayer was again dominated by Na, followed by Ca and K reduced to trace levels (Figure 6b). The complete absence of Ba and Sr is possibly due to their lower abundance compared to Na and Ca under extended reaction with the spring water, which itself is dominated by Na (Table 1). This final state may reflect equilibrium with the euxinic water, where Na becomes the major interlayer cation due to its high concentration in solution, while Ca remains due to its strong binding capacity. This observation is consistent with our previous study at the study site[26] where the interlayers of euxinic spring impacted Al-rich smectite were dominated by Na.

In SWa-1 the dominance of Na at the onset reflects the pretreatment homogenization of the smectite with Na, saturating the interlayer with Na. Upon exposure to the euxinic spring, the initial increase in Na, Ca, and K after 8 hours suggests rapid cation exchange driven by the influx of dissolved ions from the spring water (Figure 6a). The persistence of Na as the dominant cation indicates that, despite competition from Ca and K, the high initial Na in the interlayer delayed

immediate displacement. The delayed displacement of Na could also be associated to the distribution of layer charge in SWa-1. The layer charge is located in the tetrahedral sheet, due to isomorphic substitution in the tetrahedral sheet. This means there is a stronger bond between the tetrahedral sheet and the interlayer cation when compared to SAz-1. The introduction of Ba and Sr at this stage is due to the presence of dissolved Ba and Sr in the euxinic water. The lower hydration energy of K and its tendency for selective fixation in clays is possibly responsible for the increase noticed after 120 hours, making it accumulate more effectively than the larger Ba and Sr cations, which may have been gradually desorbed due to competitive displacement by Ca and Na. The significant decrease in Na concentration after 504 hours with Ca becoming the dominant interlayer cation reflects the thermodynamically favored absorption of Ca over Na in smectite due to its higher charge density and stronger electrostatic interactions with the clay's negatively charged surfaces[57,58]. This contradicts previous laboratory-based experiments that studied cation exchange due to reductive dissolution of Fe-rich smectites. These studies show that the resulting mineral phase after reductive dissolution of Fe-rich smectite will incorporate cations with lower charge density such as K, Na more than cations with higher charge density such as Ca[3]. However, our study shows that cation exchange in natural aqueous system is different from laboratory experiments. The decline in Na, K, Ba, and Sr (Figure 6a) suggests that these cations were outcompeted by Ca over extended reaction times. The near-complete loss of Ba and Sr may be attributed to their lower affinity compared to Ca and their possible re-release into the spring as the system approached equilibrium. The changes seen in interlayer cation compositions of both clays is reflected in their 001-peak shift, collapse and shape change as revealed by the XRD analysis.

### 2.5.4 Effect of euxinic condition on smectite morphology

The octahedral sheet composition of smectite influences its morphology. The structural cation in the octahedral sheet determines the structure of the smectite. Smectite clays generally have platy, flat cornflakes morphology. In this study, we observed that the Fe-rich smectite morphology changed after the 504 hours. The clay particles developed more folded edges making the edges to be darker in the bright field TEM images. The observed curling and folding at the edges after three weeks of reaction in an anoxic, sulfidic spring suggests significant mineralogical alterations driven by redox and sulfidation processes. Such morphological changes are consistent with previous studies documenting the transformation of Fe(III)-rich smectite under reducing conditions[52]. The reduction of the structural Fe(III) in SWa-1 led to partial dissolution of octahedral layers[16,23]. The preferential attack on particle edges, where broken bonds and increased surface reactivity are concentrated can result in the observed curling and folding[19]. Al-rich smectite on the other hand did not show any change in morphology. This is likely because Al is not redox sensitive and Al-rich smectite is much less responsive to redox changes. This is consistent with our previous study in the study area[26].

### 2.5.5 Evidence of secondary mineral precipitation

Evidence of secondary mineralization was seen only in SWa-1. XRD analysis of the reacted SWa-1 after 504 hours revealed the presence of elemental sulfur and pyrite as secondary minerals precipitated due to the clay's interaction with the euxinic spring. The formation of elemental sulfur ($S^0$) and pyrite ($FeS_2$) provides clear evidence of sulfur-driven mineral transformation under reducing conditions. These newly formed phases indicate complex redox interactions between structural Fe(III) in smectite and aqueous sulfide ($H_2S/HS^-$) in the euxinic spring, with implications for both clay mineral stability and sulfur cycling in euxinic environments. The detection of pyrite

suggests that Fe(II), released via the reductive dissolution of smectite Fe(III), reacted with dissolved sulfide in the spring releasing $Fe^{2+}$ into solution[52,61]. Initial $Fe^{2+}$ reaction with sulfide forms metastable intermediates (e.g., mackinawite, FeS), which can further react with polysulfides or $H_2S$ to form pyrite[62]. Smectite edges may have facilitated pyrite nucleation by providing reactive sites for $Fe^{2+}$-sulfide interaction.

The presence of $S^0$ indicates an oxidative sulfur pathway, possibly due to incomplete Sulfide Oxidation reaction between Fe(III) (from smectite) and $H_2S$ from the euxinic spring producing $S^0$[62–65]. Another possibility is polysulfide disproportionation. Under neutral-alkaline conditions, polysulfides (formed from $H_2S$ oxidation) may decompose into $S^0$ and sulfide. The coexistence of $S^0$ and pyrite suggests dynamic sulfur cycling, where $S^0$ could serve as a precursor for pyrite formation or persist due to kinetic barriers in its further reduction[62]. The formation of pyrite and $S^0$ demonstrates that Fe-rich smectite is a reactive substrate for sulfur transformations. Though XRD analysis of SAz-1 shows the presence of trace amount of $S^0$ and barite, we believe that these phases were likely inherited from the spring rather than produced through smectite-fluid interactions. In contrast, SWa-1 showed a significant increase in pyrite ($FeS_2$) and elemental sulfur, judging from the peak heights, although we believe that some of the $S^0$ in SWa-1 is inherited from the spring. However, the lack of detectable barite in SWa-1 implies a more active role of Fe in SWa-1. Barite, being highly stable in sulfate-rich euxinic environments likely precipitated directly from the spring water without significant interaction with the Al-smectite. Senko et al. (2004) showed that microorganisms are actively cycling sulfur from sulfide to $S^0$ which is further oxidized to sulfate, thereby precipitating barite in the spring. The abundance of pyrite and $S^0$ in the reacted SWa-1, in the absence of barite, indicates that iron redox chemistry played a key role in sulfur speciation in our experiment.

The observed dissolution of Fe-rich smectite under anoxic and sulfidic conditions in our field experiment provides critical insights into the stability of clay minerals on early Mars and their implications for past habitability. Recent discoveries by Mars missions have detected both smectite-rich deposits and sulfur-bearing minerals in ancient sedimentary environments[37,66,67]. The persistence of Fe-rich smectite in some Martian terrains may suggests localized stability, while its absence in other regions may reflect sulfide-driven breakdown, as observed in our experiment. Also, the released $Fe^{2+}$ and silica during Fe-rich smectite dissolution under sulfidic conditions could have supported chemolithotrophic microbial communities on early Mars[68].

## 2.6 Conclusions

The reaction of smectites with varying octahedral sheet composition (Al-rich and Fe-rich) in a modern euxinic spring for over 500 hours shows that the octahedral sheet composition of smectite plays an important role in its response to euxinic conditions. The reaction of Fe-rich smectite with the euxinic spring resulted in significant mineralogical, morphological, and compositional changes in Fe-rich smectite. This demonstrates the dynamic interplay between Fe(III)-bearing clays and reduced sulfur species. The formation of pyrite ($FeS_2$) and elemental sulfur ($S^0$), as confirmed by XRD, indicates sulfur-driven redox transformations, where structural Fe(III) in smectite was reduced to Fe(II), promoting pyrite nucleation. Concurrently, the release of Fe, along with the observed loss of Si and Al, and the persistence of smectite in the XRD analysis points to partial dissolution of the smectite structure.

The morphological alterations i.e. curling and folding of clay edges, further support a dissolution mechanism, where preferential leaching of octahedral Fe leads to structural collapse, thereby destabilizing the smectite layers. The color shift from yellow to black aligns with the reduction of Fe(III) and the precipitation of fine-grained pyrite, which are known to impart dark coloration. All

these changes highlight the sensitivity of Fe-rich smectite to euxinic conditions, with implications for its stability in natural reducing environments such as on the early earth, sulfate-rich groundwater systems, or hydrothermal vents. However, this study supports previous studies by showing that Al-rich smectite only responds to euxinic conditions by cation exchange while the octahedral sheet remains stable.

The observed cation exchange trends in reacted SAz-1 align with known smectite cation exchange hierarchies (Ca > K > Na under certain conditions) but the transition from Na to Ca dominance in SWa-1 interlayer after reductive dissolution contrary to reported laboratory experiments in literature highlight the role of reaction kinetics limitations in natural systems. Apart from aqueous chemistry, layer charge, cation ionic properties, the response of reacted SAz-1 and SWa-1 to euxinic aqueous solution is controlled by the variations in layer charge distribution and redox interactions in Fe-bearing clays. The short-term enrichment of Ba and Sr suggests that smectite may act as a temporary sink for these trace metals in euxinic environments, though long-term retention is limited. These findings have implications for understanding trace metal cycling in reducing aquatic systems and the role of clay minerals in regulating cation mobility.

This study shows the role of Fe-rich clays as both reactants and templates for secondary mineralization on the early earth. Furthermore, this study also shows that Fe-rich clay mineral would have been unstable on the early Earth, where smectite edges would have served as nucleation sites for Fe-S minerals. Pyrite would have also been a sink for Fe and S on the early earth. Also, Fe-rich clay-sulfide reactions could have altered Martian clay stability, explaining the partial dissolution/transformation of smectites observed by rover missions[69].

## Acknowledgements

We thank Dani Storms for help with deploying clay samples into the spring. We acknowledge funding support from the University of Oklahoma Joe and Robert Klabzuba Chair and NASA grant 22-HW22_2-0005.

## References


(1) Droge, S. T. J.; Goss, K.-U. Sorption of Organic Cations to Phyllosilicate Clay Minerals: CEC-Normalization, Salt Dependency, and the Role of Electrostatic and Hydrophobic Effects. *Environ. Sci. Technol.* **2013**, *47* (24), 14224–14232. https://doi.org/10.1021/es403187w.

(2) Hearon, S. E.; Orr, A. A.; Moyer, H.; Wang, M.; Tamamis, P.; Phillips, T. D. Montmorillonite Clay-Based Sorbents Decrease the Bioavailability of per- and Polyfluoroalkyl Substances (PFAS) from Soil and Their Translocation to Plants. *Environ. Res.* **2022**, *205*, 112433. https://doi.org/10.1016/j.envres.2021.112433.

(3) Stucki, J. W. Properties and Behaviour of Iron in Clay Minerals. In *Developments in Clay Science*; Elsevier, 2013; Vol. 5, pp 559–611. https://doi.org/10.1016/B978-0-08-098258-8.00018-3.

(4) Moore, D. M.; Reynolds, R. C., Jr. *X-Ray Diffraction and the Identification and Analysis of Clay Minerals*, 2nd ed.; Oxford University Press, 1997.

(5) Stucki, J. W. Structural Iron in Smectites. In *Iron in Soils and Clay Minerals*; Stucki, J. W., Goodman, B. A., Schwertmann, U., Eds.; Springer Netherlands: Dordrecht, 1988; pp 625–675. https://doi.org/10.1007/978-94-009-4007-9_17.

(6) Sanz-Montero, M. E. R.-A.; Pablo Pérez-Soba, C. Microbial Weathering of Fe-Rich Phyllosilicates and Formation of Pyrite in the Dolomite Precipitating Environment of a Miocene Lacustrine System. *Eur. J. Mineral.* **2009**, *21* (1), 163–175. https://doi.org/10.1127/0935-1221/2009/0021-1877.

(7) Jaisi, D. P.; Liu, C.; Dong, H.; Blake, R. E.; Fein, J. B. Fe2+ Sorption onto Nontronite (NAu-2). *Geochim. Cosmochim. Acta* **2008**, *72* (22), 5361–5371. https://doi.org/10.1016/j.gca.2008.08.022.

(8) Jaisi, D. P.; Eberl, D. D.; Dong, H.; Kim, J. The Formation of Illite from Nontronite by Mesophilic and Thermophilic Bacterial Reaction. *Clays Clay Miner.* **2011**, *59* (1), 21–33. https://doi.org/10.1346/CCMN.2011.0590105.

(9) Jaisi, D. P.; Dong, H.; Morton, J. P. Partitioning of Fe(II) in Reduced Nontronite (NAu-2) to Reactive Sites: Reactivity in Terms of Tc(VII) Reduction. *Clays Clay Miner.* **2008**, *56* (2), 175–189. https://doi.org/10.1346/CCMN.2008.0560204.

(10) Jaisi, D. P.; Dong, H.; Plymale, A. E.; Fredrickson, J. K.; Zachara, J. M.; Heald, S.; Liu, C. Reduction and Long-Term Immobilization of Technetium by Fe(II) Associated with Clay Mineral Nontronite. *Chem. Geol.* **2009**, *264* (1–4), 127–138. https://doi.org/10.1016/j.chemgeo.2009.02.018.

(11) Jaisi, D. P.; Dong, H.; Kim, J.; He, Z.; Morton, J. P. Nontronite Particle Aggregation Induced by Microbial Fe(III) Reduction and Exopolysaccharide Production. *Clays Clay Miner.* **2007**, *55* (1), 96–107. https://doi.org/10.1346/CCMN.2007.0550108.

(12) Jaisi, D. P.; Dong, H.; Liu, C. Kinetic Analysis of Microbial Reduction of Fe(III) in Nontronite. *Environ. Sci. Technol.* **2007**, *41* (7), 2437–2444. https://doi.org/10.1021/es0619399.

(13) Jaisi, D. P.; Dong, H.; Liu, C. Influence of Biogenic Fe(II) on the Extent of Microbial Reduction of Fe(III) in Clay Minerals Nontronite, Illite, and Chlorite. *Geochim. Cosmochim. Acta* **2007**, *71* (5), 1145–1158. https://doi.org/10.1016/j.gca.2006.11.027.

(14) Gorski, C. A.; Klüpfel, L. E.; Voegelin, A.; Sander, M.; Hofstetter, T. B. Redox Properties of Structural Fe in Clay Minerals: 3. Relationships between Smectite Redox and Structural Properties. *Environ. Sci. Technol.* **2013**, *47* (23), 13477–13485. https://doi.org/10.1021/es403824x.

(15) Stucki, J. W. Properties and Behaviour of Iron in Clay Minerals. In *Developments in Clay Science*; Elsevier, 2013; Vol. 5, pp 559–611. https://doi.org/10.1016/B978-0-08-098258-8.00018-3.

(16) Stucki, J. W.; Kostka, J. E. Microbial Reduction of Iron in Smectite. *Comptes Rendus Geosci.* **2006**, *338* (6), 468–475. https://doi.org/10.1016/j.crte.2006.04.010.

(17) Neumann, A.; Sander, M.; Hofstetter, T. B. Redox Properties of Structural Fe in Smectite Clay Minerals. In *ACS Symposium Series*; Tratnyek, P. G., Grundl, T. J., Haderlein, S. B., Eds.; American Chemical Society: Washington, DC, 2011; Vol. 1071, pp 361–379. https://doi.org/10.1021/bk-2011-1071.ch017.

(18) Stucki, J. W.; Lee, K.; Zhang, L.; Larson, R. A. Effects of Iron Oxidation State on the Surface and Structural Properties of Smectites. *Pure Appl. Chem.* **2002**.

(19) Stucki, J. W. A Review of the Effects of Iron Redox Cycles on Smectite Properties. *Comptes Rendus Geosci.* **2011**, *343* (2–3), 199–209. https://doi.org/10.1016/j.crte.2010.10.008.

(20) Liu, D.; Dong, H.; Bishop, M. E.; Zhang, J.; Wang, H.; Xie, S.; Wang, S.; Huang, L.; Eberl, D. D. Microbial Reduction of Structural Iron in Interstratified Illite-smectite Minerals by a Sulfate-reducing Bacterium. *Geobiology* **2012**, *10* (2), 150–162. https://doi.org/10.1111/j.1472-4669.2011.00307.x.

(21) Sherman, D. M.; Vergo, N. Optical (Diffuse Reflectance) and Moessbauer Spectroscopic Study of Nontronite and Related Fe-Bearing Smectites. *Am. Mineral.* **1988**, *73* (11–12), 1346–1354.

(22) Chemtob, S. M.; Nickerson, R. D.; Morris, R. V.; Agresti, D. G.; Catalano, J. G. Synthesis and Structural Characterization of Ferrous Trioctahedral Smectites: Implications for Clay Mineral Genesis and Detectability on Mars. *J. Geophys. Res. Planets* **2015**, *120* (6), 1119–1140. https://doi.org/10.1002/2014JE004763.

(23) Kostka, J. E.; Stucki, J. W.; Nealson, K. H.; Wu, J. Reduction of Structural Fe(III) in Smectite by a Pure Culture of Shewanella Putrefaciens Strain MR-1. *Clays Clay Miner.* **1996**, *44* (4), 522–529. https://doi.org/10.1346/CCMN.1996.0440411.

(24) Veith, J. A.; Jackson, M. L. Iron Oxidation and Reduction Effects on Structural Hydroxyl and Layer Charge in Aqueous Suspensions of Micaceous Vermiculites. *Clays Clay Miner.* **1974**, *22* (4), 345–353. https://doi.org/10.1346/CCMN.1974.0220405.

(25) Stucki, J. W.; Roth, C. B. Interpretation of Infrared Spectra of Oxidized and Reduced Nontronite. *Clays Clay Miner.* **1976**, *24* (6), 293–296. https://doi.org/10.1346/CCMN.1976.0240604.

(26) Apalara, I. T.; Hodges, C.; Sabisch, J. E. C.; Elwood Madden, M. E.; Larson, P. R.; Elwood Madden, A. S. Understanding the Impact of a Modern Euxinic Spring on Sediment Using

Bulk Sediment and Smectite Clay-Preserved Proxies. *ACS Earth Space Chem.* **2025**, *9* (2), 265–276. https://doi.org/10.1021/acsearthspacechem.4c00269.

(27) Gilleaudeau, G. J.; Sahoo, S. K.; Ostrander, C. M.; Owens, J. D.; Poulton, S. W.; Lyons, T. W.; Anbar, A. D. Molybdenum Isotope and Trace Metal Signals in an Iron-Rich Mesoproterozoic Ocean: A Snapshot from the Vindhyan Basin, India. *Precambrian Res.* **2020**, *343*, 105718. https://doi.org/10.1016/j.precamres.2020.105718.

(28) Johnston, D. T.; Wolfe-Simon, F.; Pearson, A.; Knoll, A. H. Anoxygenic Photosynthesis Modulated Proterozoic Oxygen and Sustained Earth's Middle Age. *Proc. Natl. Acad. Sci.* **2009**, *106* (40), 16925–16929. https://doi.org/10.1073/pnas.0909248106.

(29) Gill, B. C.; Lyons, T. W.; Young, S. A.; Kump, L. R.; Knoll, A. H.; Saltzman, M. R. Geochemical Evidence for Widespread Euxinia in the Later Cambrian Ocean. *Nature* **2011**, *469* (7328), 80–83. https://doi.org/10.1038/nature09700.

(30) Hammarlund, E. U.; Dahl, T. W.; Harper, D. A. T.; Bond, D. P. G.; Nielsen, A. T.; Bjerrum, C. J.; Schovsbo, N. H.; Schönlaub, H. P.; Zalasiewicz, J. A.; Canfield, D. E. A Sulfidic Driver for the End-Ordovician Mass Extinction. *Earth Planet. Sci. Lett.* **2012**, *331–332*, 128–139. https://doi.org/10.1016/j.epsl.2012.02.024.

(31) Sperling, E. A.; Melchin, M. J.; Fraser, T.; Stockey, R. G.; Farrell, U. C.; Bhajan, L.; Brunoir, T. N.; Cole, D. B.; Gill, B. C.; Lenz, A.; Loydell, D. K.; Malinowski, J.; Miller, A. J.; Plaza-Torres, S.; Bock, B.; Rooney, A. D.; Tecklenburg, S. A.; Vogel, J. M.; Planavsky, N. J.; Strauss, J. V. A Long-Term Record of Early to Mid-Paleozoic Marine Redox Change. *Sci. Adv.* **2021**, *7* (28), eabf4382. https://doi.org/10.1126/sciadv.abf4382.

(32) de Vera, J.-P.; Alawi, M.; Backhaus, T.; Baqué, M.; Billi, D.; Böttger, U.; Berger, T.; Bohmeier, M.; Cockell, C.; Demets, R.; de la Torre Noetzel, R.; Edwards, H.; Elsaesser, A.; Fagliarone, C.; Fiedler, A.; Foing, B.; Foucher, F.; Fritz, J.; Hanke, F.; Herzog, T.; Horneck, G.; Hübers, H.-W.; Huwe, B.; Joshi, J.; Kozyrovska, N.; Kruchten, M.; Lasch, P.; Lee, N.; Leuko, S.; Leya, T.; Lorek, A.; Martínez-Frías, J.; Meessen, J.; Moritz, S.; Moeller, R.; Olsson-Francis, K.; Onofri, S.; Ott, S.; Pacelli, C.; Podolich, O.; Rabbow, E.; Reitz, G.; Rettberg, P.; Reva, O.; Rothschild, L.; Sancho, L. G.; Schulze-Makuch, D.; Selbmann, L.; Serrano, P.; Szewzyk, U.; Verseux, C.; Wadsworth, J.; Wagner, D.; Westall, F.; Wolter, D.; Zucconi, L. Limits of Life and the Habitability of Mars: The ESA Space Experiment BIOMEX on the ISS. *Astrobiology* **2019**, *19* (2), 145–157. https://doi.org/10.1089/ast.2018.1897.

(33) Fairén, A. G.; Davila, A. F.; Lim, D.; Bramall, N.; Bonaccorsi, R.; Zavaleta, J.; Uceda, E. R.; Stoker, C.; Wierzchos, J.; Dohm, J. M.; Amils, R.; Andersen, D.; McKay, C. P. Astrobiology through the Ages of Mars: The Study of Terrestrial Analogues to Understand the Habitability of Mars. *Astrobiology* **2010**, *10* (8), 821–843. https://doi.org/10.1089/ast.2009.0440.

(34) RUSSELL, M. J.; HALL, A. J. The Emergence of Life from Iron Monosulphide Bubbles at a Submarine Hydrothermal Redox and pH Front. *J. Geol. Soc.* **1997**, *154* (3), 377–402. https://doi.org/10.1144/gsjgs.154.3.0377.

(35) Martin, W.; Baross, J.; Kelley, D.; Russell, M. J. Hydrothermal Vents and the Origin of Life. *Nat. Rev. Microbiol.* **2008**, *6* (11), 805–814. https://doi.org/10.1038/nrmicro1991.

(36) Bibring, J.-P.; Langevin, Y.; Mustard, J. F.; Poulet, F.; Arvidson, R.; Gendrin, A.; Gondet, B.; Mangold, N.; Pinet, P.; Forget, F.; Berthé, M.; Bibring, J.-P.; Gendrin, A.; Gomez, C.;

Gondet, B.; Jouglet, D.; Poulet, F.; Soufflot, A.; Vincendon, M.; Combes, M.; Drossart, P.; Encrenaz, T.; Fouchet, T.; Merchiorri, R.; Belluci, G.; Altieri, F.; Formisano, V.; Capaccioni, F.; Cerroni, P.; Coradini, A.; Fonti, S.; Korablev, O.; Kottsov, V.; Ignatiev, N.; Moroz, V.; Titov, D.; Zasova, L.; Loiseau, D.; Mangold, N.; Pinet, P.; Douté, S.; Schmitt, B.; Sotin, C.; Hauber, E.; Hoffmann, H.; Jaumann, R.; Keller, U.; Arvidson, R.; Mustard, J. F.; Duxbury, T.; Forget, F.; Neukum, G. Global Mineralogical and Aqueous Mars History Derived from OMEGA/Mars Express Data. *Science* **2006**, *312* (5772), 400–404. https://doi.org/10.1126/science.1122659.

(37) Bishop, J. L.; Loizeau, D.; McKeown, N. K.; Saper, L.; Dyar, M. D.; Des Marais, D. J.; Parente, M.; Murchie, S. L. What the Ancient Phyllosilicates at Mawrth Vallis Can Tell Us about Possible Habitability on Early Mars. *Planet. Space Sci.* **2013**, *86*, 130–149. https://doi.org/10.1016/j.pss.2013.05.006.

(38) Jain, N.; Chauhan, P. Study of Phyllosilicates and Carbonates from the Capri Chasma Region of Valles Marineris on Mars Based on Mars Reconnaissance Orbiter-Compact Reconnaissance Imaging Spectrometer for Mars (MRO-CRISM) Observations. *Icarus* **2015**, *250*, 7–17. https://doi.org/10.1016/j.icarus.2014.11.018.

(39) Jain, R.; Jordan, N.; Tsushima, S.; Hübner, R.; Weiss, S.; Lens, P. N. L. Shape Change of Biogenic Elemental Selenium Nanomaterials from Nanospheres to Nanorods Decreases Their Colloidal Stability. *Environ. Sci. Nano* **2017**, *4* (5), 1054–1063. https://doi.org/10.1039/C7EN00145B.

(40) Senko, J. M.; Campbell, B. S.; Henriksen, J. R.; Elshahed, M. S.; Dewers, T. A.; Krumholz, L. R. Barite Deposition Resulting from Phototrophic Sulfide-Oxidizing Bacterial Activity. *Geochim. Cosmochim. Acta* **2004**, *68* (4), 773–780. https://doi.org/10.1016/j.gca.2003.07.008.

(41) Sanders, W. E. Rate and Mechanism of Barite Mineralization at Zodletone Mountain, Southwestern Oklahoma. PhD Thesis, University of Oklahoma, 1998.

(42) Bachman, E. E.; Hullaster, D.; Krumholz, L. R.; Elwood Madden, A. S. Biotic and Abiotic Mineralogical Signatures Induced by Euxinic Methane-Rich Brine Spring Discharge; 2018; p 324175. https://doi.org/Geological Society of America Abstracts with Programs. Vol. 50, No. 6 10.1130/abs/2018AM-324175.

(43) Widanagamage; Griffith, E. M.; Singer, D. M.; Scher, H. D.; Buckley, W. P.; Senko, J. M. Controls on Stable Sr-Isotope Fractionation in Continental Barite. *Chem. Geol.* **2015**, *411*, 215–227. https://doi.org/10.1016/j.chemgeo.2015.07.011.

(44) Younger, P. L. Barite Travertine from Southwestern Oklahoma and West - Central Colorado. **1984**. https://doi.org/Unpublished Masters thesis.

(45) Downs, R. T.; Hall-Wallace, M. The American Mineralogist Crystal Structure Database.

(46) Yong, S. N.; Lim, S.; Ho, C. L.; Chieng, S.; Kuan, S. H. Mechanisms of Microbial-Based Iron Reduction of Clay Minerals: Current Understanding and Latest Developments. *Appl. Clay Sci.* **2022**, *228*, 106653. https://doi.org/10.1016/j.clay.2022.106653.

(47) Stucki, J. W.; Golden, D. C.; Roth, C. B. Effects of Reduction and Reoxidation of Structural Iron on the Surface Charge and Dissolution of Dioctahedral Smectites. *Clays Clay Miner.* **1984**, *32* (5), 350–356.

(48) Rozenson, I.; Heller-Kallai, L. Reduction and Oxidation of $Fe^{3+}$ in Dioctahedral Smectites — 2: Reduction with Sodium Sulphide Solutions. *Clays Clay Miner.* **1976**, *24* (6), 283–288. https://doi.org/10.1346/CCMN.1976.0240602.

(49) O'Reilly, S. E.; Watkins, J.; Furukawa, Y. Secondary Mineral Formation Associated with Respiration of Nontronite, NAu-1 by Iron Reducing Bacteria. *Geochem. Trans.* **2005**, *6* (4), 67. https://doi.org/10.1186/1467-4866-6-67.

(50) Jones, A. M.; Murphy, C. A.; Waite, T. D.; Collins, R. N. Fe(II) Interactions with Smectites: Temporal Changes in Redox Reactivity and the Formation of Green Rust. *Environ. Sci. Technol.* **2017**, *51* (21), 12573–12582. https://doi.org/10.1021/acs.est.7b01793.

(51) Huang, L.; Feng, C.; Jiang, H.; Dong, H.; Liu, Z.; Zeng, Q.; Wang, X.; Zhang, L. Reduction of Structural Fe(III) in Nontronite by Thermophilic Microbial Consortia Enriched from Hot Springs in Tengchong, Yunnan Province, China. *Chem. Geol.* **2018**, *479*, 47–57. https://doi.org/10.1016/j.chemgeo.2017.12.028.

(52) Jaisi, D. P.; Kukkadapu, R. K.; Eberl, D. D.; Dong, H. Control of Fe(III) Site Occupancy on the Rate and Extent of Microbial Reduction of Fe(III) in Nontronite. *Geochim. Cosmochim. Acta* **2005**, *69* (23), 5429–5440. https://doi.org/10.1016/j.gca.2005.07.008.

(53) Rickard, D.; Luther, G. W. Chemistry of Iron Sulfides. *Chem. Rev.* **2007**, *107* (2), 514–562. https://doi.org/10.1021/cr0503658.

(54) Conconi, R.; Ventruti, G.; Nieto, F.; Capitani, G. TEM-EDS Microanalysis: Comparison among the Standardless, Cliff & Lorimer and Absorption Correction Quantification Methods. *Ultramicroscopy* **2023**, *254*, 113845. https://doi.org/10.1016/j.ultramic.2023.113845.

(55) McLaren, A. C. *Transmission Electron Microscopy of Minerals and Rocks*, 2nd ed.; Cambridge University Press, 1991. https://doi.org/10.1017/CBO9780511529382.

(56) Poulton, S. W.; Krom, M. D.; Raiswell, R. A Revised Scheme for the Reactivity of Iron (Oxyhydr)Oxide Minerals towards Dissolved Sulfide. *Geochim. Cosmochim. Acta* **2004**, *68* (18), 3703–3715. https://doi.org/10.1016/j.gca.2004.03.012.

(57) Robin, V.; Tertre, E.; Beaufort, D.; Regnault, O.; Sardini, P.; Descostes, M. Ion Exchange Reactions of Major Inorganic Cations (H+, Na+, Ca2+, Mg2+ and K+) on Beidellite: Experimental Results and New Thermodynamic Database. Toward a Better Prediction of Contaminant Mobility in Natural Environments. *Appl. Geochem.* **2015**, *59*, 74–84. https://doi.org/10.1016/j.apgeochem.2015.03.016.

(58) Li, K. J.; Kurniawan, A.; Christidis, G. E.; He, J. Y.; Zhou, C. H. Interfacial Interactions Controlling Adsorption of Metal Cations on Montmorillonite. *Am. Mineral.* **2024**, *109* (4), 633–655. https://doi.org/10.2138/am-2022-8834.

(59) Zhou, M.; Lu, X.; Chen, M.; Li, Q.; Wang, K.; Liu, X. Molecular Simulation on Cs, Rb Retention in Na/K-Montmorillonite Interlayer Coupling Clay Swelling/Collapse. *Appl. Geochem.* **2025**, *178*, 106249. https://doi.org/10.1016/j.apgeochem.2024.106249.

(60) Yang, S.; Li, X.; Li, Q.; Gu, P.; Liu, X.; Yang, G. Competitive Adsorption of Metal Ions at Smectite/Water Interfaces: Mechanistic Aspects, and Impacts of Co-Ions, Charge Densities, and Charge Locations. *J. Phys. Chem. C* **2020**, *124* (2), 1500–1510. https://doi.org/10.1021/acs.jpcc.9b10341.

(61) Burton, E. D.; Bush, R. T.; Johnston, S. G.; Sullivan, L. A.; Keene, A. F. Sulfur Biogeochemical Cycling and Novel Fe–S Mineralization Pathways in a Tidally Re-Flooded Wetland. *Geochim. Cosmochim. Acta* **2011**, *75* (12), 3434–3451. https://doi.org/10.1016/j.gca.2011.03.020.

(62) Rickard, D.; Luther, G. W. Chemistry of Iron Sulfides. *Chem. Rev.* **2007**, *107* (2), 514–562. https://doi.org/10.1021/cr0503658.

(63) Benning, L. G.; Wilkin, R. T.; Barnes, H. L. Reaction Pathways in the Fe–S System below 100°C. *Chem. Geol.* **2000**, *167* (1–2), 25–51. https://doi.org/10.1016/S0009-2541(99)00198-9.

(64) Thiel, J.; Byrne, J. M.; Kappler, A.; Schink, B.; Pester, M. Pyrite Formation from FeS and H2S Is Mediated through Microbial Redox Activity. *Proc. Natl. Acad. Sci.* **2019**, 201814412. https://doi.org/10.1073/pnas.1814412116.

(65) Luther, I.; Glazer, B.; Hohmann, L.; Popp, J.; Taillefert, M.; Rozan, T.; Brendel, P.; Theberge, S.; Nuzzio, D. Sulfur Speciation Monitored in Situ with Solid State Gold Amalgam Voltammetric Microelectrodes: Polysulfides as a Special Case in Sediments, Microbial Mats and Hydrothermal Vent Waters. *J. Environ. Monit.* **2000**, *3* (1). https://doi.org/10.1039/B006499H.

(66) Ehlmann, B. L.; Edwards, C. S. Mineralogy of the Martian Surface. *Annu. Rev. Earth Planet. Sci.* **2014**, *42* (1), 291–315. https://doi.org/10.1146/annurev-earth-060313-055024.

(67) Bristow, T. F.; Bish, D. L.; Vaniman, D. T.; Morris, R. V.; Blake, D. F.; Grotzinger, J. P.; Rampe, E. B.; Crisp, J. A.; Achilles, C. N.; Ming, D. W.; Ehlmann, B. L.; King, P. L.; Bridges, J. C.; Eigenbrode, J. L.; Sumner, D. Y.; Chipera, S. J.; Moorokian, J. M.; Treiman, A. H.; Morrison, S. M.; Downs, R. T.; Farmer, J. D.; Marais, D. D.; Sarrazin, P.; Floyd, M. M.; Mischna, M. A.; McAdam, A. C. The Origin and Implications of Clay Minerals from Yellowknife Bay, Gale Crater, Mars. *Am. Mineral.* **2015**, *100* (4), 824–836. https://doi.org/10.2138/am-2015-5077CCBYNCND.

(68) Michalski, J. R.; Cuadros, J.; Niles, P. B.; Parnell, J.; Deanne Rogers, A.; Wright, S. P. Groundwater Activity on Mars and Implications for a Deep Biosphere. *Nat. Geosci.* **2013**, *6* (2), 133–138. https://doi.org/10.1038/ngeo1706.

(69) Bristow, T. F.; Rampe, E. B.; Achilles, C. N.; Blake, D. F.; Chipera, S. J.; Craig, P.; Crisp, J. A.; Des Marais, D. J.; Downs, R. T.; Gellert, R.; Grotzinger, J. P.; Gupta, S.; Hazen, R. M.; Horgan, B.; Hogancamp, J. V.; Mangold, N.; Mahaffy, P. R.; McAdam, A. C.; Ming, D. W.; Morookian, J. M.; Morris, R. V.; Morrison, S. M.; Treiman, A. H.; Vaniman, D. T.; Vasavada, A. R.; Yen, A. S. Clay Mineral Diversity and Abundance in Sedimentary Rocks of Gale Crater, Mars. *Sci. Adv.* **2018**, *4* (6), eaar3330. https://doi.org/10.1126/sciadv.aar3330.

# Chapter 3: Effect of smectite octahedral composition on trace element mobility in a modern euxinic environment

Itunu T. Apalara[1*], E. C. Butler[2], Andrew S. Elwood Madden[1,3]

[1]School of Geosciences, University of Oklahoma, Norman, OK 73019, USA

[2]School of Civil Engineering and Environmental Science, University of Oklahoma, . Norman, OK 73019, USA

[3]Samuel Roberts Noble Microscopy Laboratory, University of Oklahoma, Norman, OK 73019, USA

## Abstract

Trace elements have diverse importance, ranging from essential micronutrients for life to their importance in technological advancement. While clay minerals are known to influence trace element mobility, the interactions of trace metals with clays of varying chemistry in sulfidic and anoxic environmental conditions has not been widely explored. Therefore, we investigated the role of smectite octahedral sheet composition in controlling trace element enrichment and retention in smectites during reaction with sulfidic, anoxic aqueous solutions. We conducted field-based experiments with Fe-rich (SWa-1), and Al-rich (SAz-1) exposed to a trace element-containing natural euxinic spring for 3 weeks (504 hours). With Inductively Coupled Plasma Atomic Emission Spectroscopy (ICP-AES) and Inductively Coupled Plasma Mass Spectrometry (ICP-MS) laboratory analysis of reacted and unreacted clays, we demonstrate that: (1) after 504 hours, reduced SWa-1 showed the highest trace element enrichment, particularly Ba (with over 100-fold enrichment), Rb and Sr (both over 7-fold enrichment), and Cs (with over 3-fold enrichment), correlating with increasing Fe(III)-reduction. SAz-1 on the other hand showed similar trend but the enrichment of Ba, Rb, Sr and Cs are not as high as we see in SWa-1. Furthermore, in reduced SWa-1 chalcophilic elements Sn, Cu, Zn and Pb were enriched after the initial hours of the reaction but were subsequently depleted for the remainder of the experiment, whereas in SAz-1 the reverse is the case, as the enrichment of Cu, Pb and Zn was not detected until about 504 hours in the spring. Cu in SAz-1 has a surprising enrichment over 9-fold after 504 hours in the spring. In addition, In the reduced SWa-1 the largely lithophilic elements Cr, Ga, Hf, Nb, Ta, Th, Ti, U, W, and Zr were generally enriched after the depletion of the chalcophilic elements. In contrast, the mirror image of these trends was seen with SAz-1; we saw an initial enrichment of the lithophilic elements, followed by their depletion and a subsequent enrichment of the chalcophilic elements. Moreso, reduced

SWa-1 shows to be a more effective sink for rare earth elements (REEs) compared to SAz-1. These results provide new mechanistic insights into trace element partitioning during clay-sulfide interactions and have important implications for predicting contaminant mobility in reducing environments, designing engineered clay barriers, and understanding trace element cycling and sequestration of bio-essential metals in anoxic and sulfidic sedimentary systems such as the early Earth and potentially Mars.

## 3.0 Introduction

Trace elements play a crucial role in biogeochemical cycles, acting as essential micronutrients for biological productivity[1,2] but also potentially causing toxicity when present in excess. Apart from the biochemical importance of trace elements, their importance in technological advancement is attracting more attention. Rare earth elements (REEs) have become an important discussion in world markets due to their role in technological advances. Special attention is being paid to REE mining in different environments and clays are integral parts of such studies[3], due to the ability of clays to accumulate metals through multiple mechanisms, and their high external and internal surface areas. Some studies have investigated the role of cation valency in leaching and extracting REEs[4,5]. Generally, the mobility of metals is dependent on the redox conditions in the environment, and they have been widely used as proxies for paleo-environmental redox reconstruction[6–12]. However, many factors play a role in determining the mobility of these metals, including organic matter, water column chemistry, biotic activity, redox properties of available solid mineral phase, among others [10,11,13].

Elements such as molybdenum (Mo), uranium (U), vanadium (V), and arsenic (As) exhibit distinct redox-sensitive behavior, making them valuable proxies for reconstructing paleoenvironmental

conditions[7,13–16]. Among factors controlling trace element mobility, a crucial one is the presence of a redox sensitive clay such as Fe-rich smectite. Smectite-metal interactions have been studied under oxic conditions[17–19], demonstrating that smectite can influence trace metal distribution by adsorption at phyllosilicate layer edges and through interlayer cation exchange[20], although the reduction of Fe in Fe-rich smectites increases their interlayer cation exchange even more. However, the mobility of trace metals in the presence of smectite and sulfide in anoxic conditions has not been widely explored.

Links between bulk concentrations of minerals and trace metals in euxinic conditions have also been widely studied. For example, pyrite has been proven to be an effective sink for trace metals such as Cd, Zn, Cu, and Mn in euxinic sediments[13,21,22]. Trace element concentrations in the water column and its affinity for pyrite are some of the factors that impact the accumulation of trace elements in euxinic sediments. However, the role of clay chemistry in immobilizing trace elements in modern euxinic environments has not been widely studied, most importantly their octahedral sheet composition.

The octahedral sheet composition of smectites, which can vary between dioctahedral (e.g., montmorillonite, beidellite) and trioctahedral (e.g., saponite, hectorite) structures, critically affects their surface charge, layer expandability, and affinity for trace metals[23–26]. Also, the preferential incorporation of these trace metals by smectite in a modern euxinic-oxic boundary environment has not been studied. Elemental composition of smectite clay affects its reactivity. For example, Fe-rich smectite are more sensitive to redox changes[26–29]. A wide range of studies have explored the reduction and re-oxidation of Fe-rich smectites using both organic and inorganic compounds[24,26,30–33]. Stucki et al. (1996) have shown that the potency of sulfide in reducing Fe(III) to Fe(II) in Fe-rich smectite is only second to dithionite when compared with other reducing agents.

The reduction of Fe(III) in Fe-rich clays increases its layer charge causing an increase in cation exchange capacity, which is crucial to its ability to immobilize trace elements in the environment[30,34,35]. For example, reduction of Fe causes the fixation of $K^+$ and Cr into the smectite interlayer[30]. Another property of smectite that is affected due to Fe reduction is color. The color changes from greenish-yellow to bluish-green after reduction[24,26].

Euxinic systems, such as modern Black Sea basin or anoxic fjords, are characterized by high dissolved sulfide ($H_2S$) concentrations, which can lead to the formation of metal-sulfide precipitates and organic-metal complexes. In such environments, smectites may compete with sulfides and organic matter for trace element binding, yet the extent to which their octahedral chemistry influences this partitioning is unclear. Understanding these interactions is essential for predicting trace element fate in both modern euxinic systems and ancient sedimentary records, where smectite clay composition may be proxies for geochemical signals. Additionally, with increased primary production on ocean surfaces as a result of increased anthropogenic continental nutrient loading[36,37], we might have a repetition of the Proterozoic widespread ocean bottom anoxia and ultimately euxinia in the near future[10]. Therefore, investigating the distribution of metals at euxinic/oxic boundaries will be increasingly critical.

Therefore, we studied the impact of smectite octahedral sheet composition on trace element accumulation in a modern euxinic environment by comparing trace element enrichment between Fe-rich smectite and Al-rich smectite reacted in the field with euxinic spring discharge. We aim to identify the dominant controls, including octahedral cation substitution, layer charge, and sulfide competition on metal adsorption and retention. Our findings advance the understanding of clay-metal interactions in sulfidic environments and the use of trace elements in smectites paleoenvironmental reconstruction in euxinic sediments, especially on early Earth and potentially

on Mars, where smectite and potential paleo-sulfidic conditions have been identified. Furthermore, this work has implications for contaminant mobility in anoxic sediments, remediation strategies, and the formation of economically important metal deposits in reducing basins.

## 3.1 Study Area

The study site is as described in Apalara et al. (2025). Zodletone spring is an anoxic and sulfidic spring located in southwest Oklahoma. Spring waters originate as a combination of deep basinal brine mixing with meteoric waters. The spring has no detectable oxygen, with a pH of 7.1, and a high total dissolved solids values ranging from ~9,000 to 11,000 mg/L[38]. Concentrations of sulfide in spring are ~2mM[39]. Although the spring flow was not quantified, discharge from the main pool feeds an outflow stream that was observed to remain consistent over a three-year period despite fluctuations in regional precipitation[38].

## 3.2 Sampling and Analysis

Two different clay standard materials from the Clay Mineral Society were used for this study. One is Al-rich (montmorillonite) (SAz-1), and the other is dioctahedral Fe-rich smectite (SWa-1). Both clays were gently disaggregated using the agate mortar and pestle. The disaggregated clays were soaked in UPW at a ratio of about 15 g: 200 ml for about 24 hours to remove non clay materials. A set of both clays were homogenized with $Na^+$ at a ratio of 1 g of clay / 10 ml of 1 M NaCl solution. A total of 15 g of each clay was allowed to equilibrate with the Na solution for 3 days, then rinsed four times with ultrapure water. The rinsed samples were transferred into dialysis bags (cellulose acetate, 32 mm diameter, molecular weight cutoff (MWCO) of 6-8 kDa) and were deployed into the euxinic spring for 8 hours. Another set of the clays were prepared without equilibrating with $Na^+$ and deployed into the euxinic spring for 5 days (120 hours). Another set was prepared and deployed for 3 weeks (504 hours). Finally sets of each clay with and without

homogenizing with Na were reserved to serve as controls (background) for the experiment and were not reacted with the euxinic spring.

Reacted clays were retrieved from the euxinic spring under strict anaerobic conditions. Anaerobic canning jars were prepared in the laboratory. Jars were opened in an anaerobic chamber (97:3 $N_2$:$H_2$), equilibrated, and sealed for transport to the field. For sampling, the sealed jars were immersed into the spring and opened below the water surface, as the spring water itself has no detectable oxygen. Without exposure to the atmosphere, the dialysis tubes with reacted clays were tucked into the jars and closed. The samples were transported back to the lab on dry ice and were transferred immediately to the freezer. The frozen samples were freeze dried and were gently passed through a 0.42 mm sieve. All samples were kept in an anaerobic chamber prior to analysis. All samples were in duplicates and analyzed for base metals and whole rock chemistry using ICP-AES, trace metal analysis by ICP-MS and ferrous iron analysis by titration with potassium dichromate following acid decomposition at ALS Vancouver.

Spring water samples were collected from the main pool with syringes, passed through 0.2-micron filters (discarding the initial filtered solution), and stored under ice in tubes acidified to <pH 2 with nitric acid. Samples were kept refrigerated or on ice during storage and shipment to the University of Houston ICP Analytical Laboratory & Agilent Facility Center. Sample was in duplicate, and they were analyzed with an Agilent 725 ICP-OES and an Agilent 8800 ICP-QQQ-MS. Reported values are the calculated mean of each duplicate measurement.

## 3.3 Results

### 3.3.1 Evidence and extent of clay Fe(III) reduction

Visual observation of reacted samples shows definite color changes typical of structural Fe reduction especially in Fe-rich smectite SWa-1. The color of SWa-1 changed from yellowish in the unreacted to a completely dark-blue-greenish color after 504 hours of reaction in the spring. This color change has been reported in literature to be an indication of structural Fe reduction[26,40]. Al-rich smectite SAz-1 on the other hand, shows a slight color change from white to slightly darker at the end of 504 hours (as described in Chapter 2).

All samples, both reacted and unreacted clays were analyzed for ferrous Fe concentration in order to qualitatively ascertain Fe reduction and also quantify the extent of Fe reduction. In SWa-1, after 8 hours in the euxinic spring, average ferrous Fe concentration went from 0.36% in unreacted SWa-1 to 0.48%. It increased to 1.28% after 120 hours and ultimately 2.86% after 504 hours in the spring. SAz-1 on the other hand had an average of 0.13% ferrous Fe in unreacted sample, which remained unchanged for the first 8 hours in the spring. After 120 hours, it increased to 0.26% and decreased back to the initial value of 0.13% after 504 hours of reaction in the spring (Figure 1).

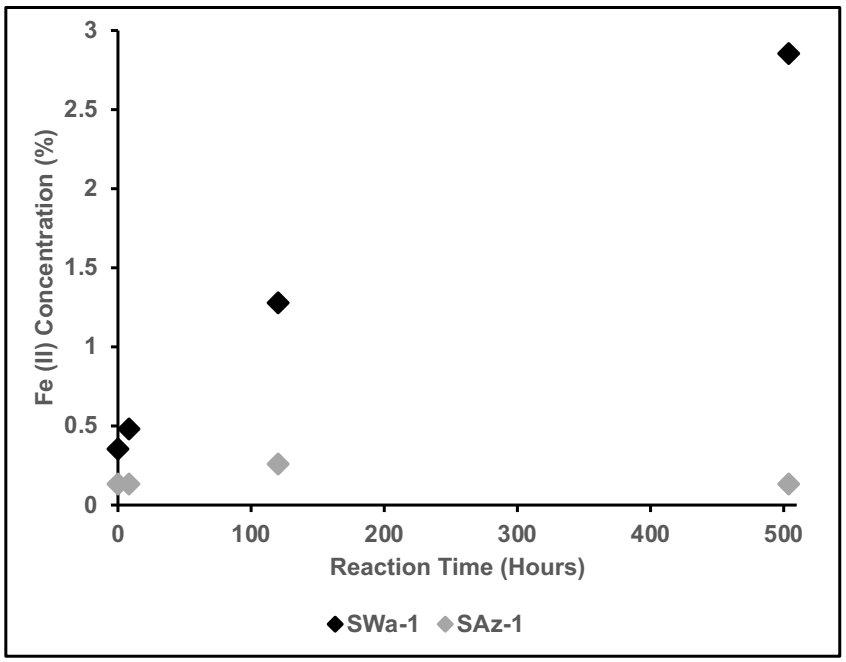


Figure 1: Fe(II) concentration in smectites with increasing time reacted in the euxinic spring

### 3.3.2. Elemental composition of the euxinic spring water

The trace element and Rare Earth Element concentrations of the spring water are displayed in Table 1. Ba and Sr are typically considered as 'trace' elements and categorized as such here. Their values are provided from previous analysis[38] of spring water chemistry. Their values were not recorded in our analyses since they occur at much higher concentrations in the euxinic spring water than is used in the ICP-MS methods in this study, and they were not included in the ICP-OES elemental standards.

**Table 1: Trace element concentrations, including rare earth elements, in Zodletone spring water**

| Trace element | Concentration (µg/kg) | Standard Deviation | REE | Concentration (µg/kg) | Standard Deviation |
|---|---|---|---|---|---|
| Ba | 67,000.00[38] | | Ce | 0.63 | 0.58 |
| Cr | 2.19 | 0.90 | Dy | 0.72 | 0.62 |
| Cs | 4.02 | 0.26 | Er | 0.91 | 0.82 |
| Ga | 1.19 | 0.76 | Eu | 27.89 | 2.04 |
| Hf | 0.87 | 0.37 | Gd | 1.51 | 0.86 |
| Nb | 2.57 | 1.27 | Ho | 1.00 | 0.93 |
| Rb | 67.00 | 2.94 | La | 2.1 | 0.9 |
| Sn | 2.13 | 1.67 | Lu | 0.98 | 0.81 |
| Sr | 19,360.00 | 55.90 | Nd | 1.51 | 0.93 |
| Th | 1.39 | 0.82 | Pr | 0.8 | 0.7 |
| Ti | 1.12 | 14.07 | Sc | 0.80 | 0.04 |
| U | 1.51 | 1.38 | Sm | 1.1 | 0.7 |
| V | 0.60 | 0.65 | Tb | 0.9 | 0.0 |
| Zr | 1.19 | 0.26 | Tm | 0.83 | 0.73 |
| Co | 1.46 | 0.11 | Y | 0.69 | 0.12 |
| Cu | 1.87 | 0.00 | Yb | 0.62 | 0.49 |
| Li | 1,109.00 | 11.19 | | | |
| Ni | 1.17 | 0.90 | | | |
| Pb | 0.96 | 0.63 | | | |
| Zn | 74.81 | 11.27 | | | |

### 3.3.3 Trace elements in reacted clays

#### 3.3.3.1 Trace element distribution in Fe-rich smectite SWa-1

We analyzed trace element concentrations in all the samples. The concentrations normalized to the concentrations measured in the unreacted SWa-1 (background) are presented in Table 2. Normalization was done by dividing measured values in reacted samples by measured values in

unreacted sample. Values >1 representing enrichment and values <1 representing depletion. Ba, Cs, Rb, and Sr are continuously enriched throughout the experiment. Ba has the highest enrichment level with over a 100-fold enrichment after 504 hours, followed by Rb and Sr with over 7-fold enrichment after 504 hours and Cs has over 3-fold enrichment in the 504 hours reaction time in the euxinic spring. The enrichment trend seen in Ba and Sr also corresponds to their concentration levels in the spring (Figure 2). Cr, Ga, Hf, Nb, Ta, Th, Ti, U, W, and Zr all became enriched only after 504 hours. However, Sn, Cu, Pb and Zn were all enriched during the initial 8 hours but became depleted as reaction time progressed. Li has a 2-fold enrichment in the first 120 hours but went back to its initial concentration in the unreacted after 504 hours.

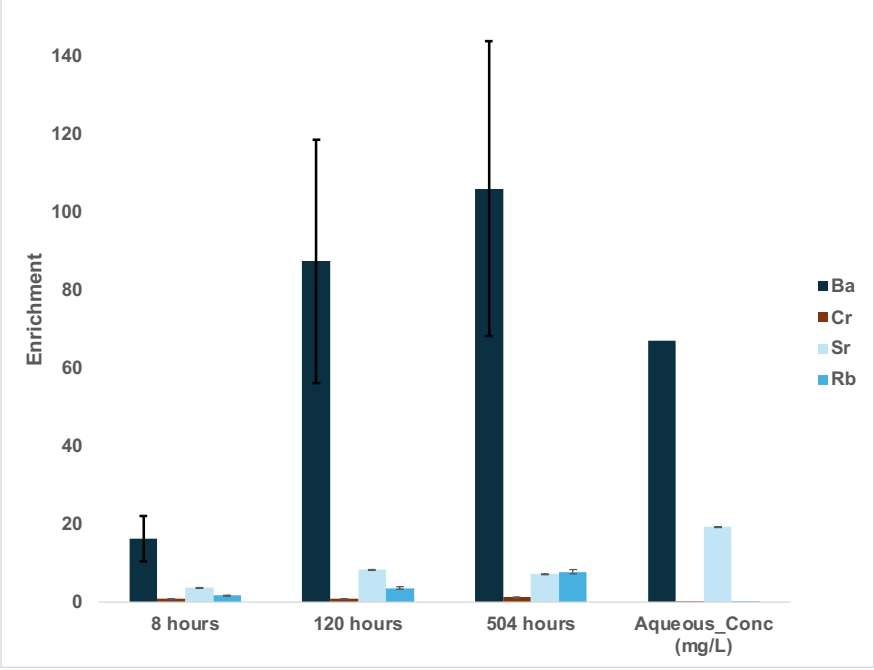


Figure 2: Ba, Cr, Sr and Rb showing corresponding enrichment trend in SWa-1 over their concentrations in the unreacted clay, along with their respective aqueous concentration in the spring discharge. Ba and Sr with higher concentration in the spring also are more enriched in the clay.

**Table 2: Trace element enrichment levels and uncertainty in reacted Fe-rich smectite in alphabetical order (> 1 = enriched (Bold), < 1 = depleted (*Italics*)). Uncertainty = E* [((std dev R)/R)^2+((std dev U)/U)^2]^0.5, where E is enrichment, R is concentration in reacted sample and U is concentration in unreacted sample.**

| Element | SWa-1_8 hours | SWa-1_120 hours | SWa-1_504 hours |
|---|---|---|---|
| **Ba** | **16.3±5.8** | **87.5±31.2** | **106±37** |
| ***Co*** | *0.80±0.13* | *0.42±0.07* | *0.70±0.11* |
| **Cr** | *0.89±0.02* | *0.84±0.02* | **1.20±0.05** |
| **Cs** | **1.08±0.02** | **1.90±0.03** | **3.15±0.05** |
| **Cu** | **5.00±0.11** | 0.73±0.00 | **1.09±0.00** |
| **Ga** | *0.93±0.00* | *0.96±0.00* | **1.2±0.00** |
| **Hf** | *0.90±0.03* | *0.95±0.03* | **1.60±0.05** |
| **Li** | **2.0±0.0** | **2.0±0.0** | *1.0±0.0* |
| **Nb** | *0.88±0.03* | *0.90±0.03* | **1.30±0.04** |
| ***Ni*** | *0.73±0.05* | *0.53±0.07* | *0.90±0.06* |
| **Pb** | **1.80±0.12** | *0.40±0.03* | *1.00±0.07* |
| **Rb** | **1.7±0.1** | **3.6±0.3** | **7.8±0.6** |
| **Sn** | **1.92±0.40** | *0.70±0.14* | *1.04±0.21* |
| **Sr** | **3.80±0.05** | **8.32±0.12** | **7.2±0.1** |
| **Ta** | *1.0±0.0* | *1.0±0.0* | **1.5±0.0** |
| **Th** | *0.93±0.02* | *0.90±0.02* | **1.32±0.03** |
| ***Ti*** | *0.93±0.02* | *0.91±0.02* | *1.04±0.02* |
| **U** | *0.70±0.01* | *0.7±0.0* | **1.10±0.01** |
| ***V*** | *0.8±0.0* | *0.8±0.0* | *0.73±0.00* |
| ***W*** | *1.0±0.4* | *0.7±0.3* | *1.2±0.4* |
| **Zn** | **1.10±0.01** | *0.95±0.01* | *0.96±0.01* |
| **Zr** | *0.9±0.0* | *0.9±0.0* | **1.50±0.01** |

### 3.3.3.2 Trace element distribution in Al-rich smectite SAz-1

The trace element concentrations in the reacted SAz-1 normalized to the values in the unreacted SAz-1 (background) is shown in Table 3. In terms of enrichment and depletion in the reacted SAz-

1, Ba, Cs, Rb, and Sn are continuously enriched throughout the experiment, although at values far less than in SWa-1. Sr is similarly enriched at 8 hours, reaches a maximum at 120 hours, and returns to the 8-hour value at 504 hours. Furthermore, Ga, Hf, Ta, Th, Ti, U, V, Zr and Li were largely unchanged; slightly enriched for the first 120 hours then returning closer to their original values, with variations within 10% over the reaction time. Cr was 29% enriched around 120 hours but returned to its original value by 504 hours. Ni was only slightly enriched in the first 8 hours. Cu, Pb and Zn were only enriched in the SAz-1 clay after 504 hours in the spring. Co remained unchanged, while Nb and W were depleted throughout the experiment.

**Table 3: Trace element enrichment levels and Uncertainty in reacted Al-rich smectite in alphabetical order (> 1 = enriched (Bold), < 1 = depleted (*Italics*)). Uncertainty = E* [((std dev R)/R)^2+((std dev U)/U)^2]^0.5, where E is enrichment, R is concentration in reacted sample and U is concentration in unreacted sample.**

| Element | SAz-1_8 hours | SAz-1_120 hours | SAz-1_504 hours |
|---|---|---|---|
| **Ba** | **2.88±0.08** | **6.55±0.18** | **5.4±0.2** |
| ***Co*** | *1.0±0.0* | *1.0±0.0* | *1.0±0.0* |
| **Cr** | *1.0±0.1* | **1.29±0.18** | *1.0±0.2* |
| **Cs** | **1.14±0.03** | **1.82±0.04** | **2.31±0.05** |
| **Cu** | *0.5±0.0* | *0.22±0.04* | **9.43±1.30** |
| ***Ga*** | *1.01±0.02* | *1.06±0.03* | *0.94±0.02* |
| ***Hf*** | *1.03±0.02* | *1.04±0.02* | *0.99±0.02* |
| ***Li*** | *1.05±0.00* | *1.09±0.00* | *0.95±0.00* |
| ***Nb*** | *1±0.02* | *0.99±0.02* | *0.92±0.02* |
| ***Ni*** | *1.2±0.2* | *0.8±0.2* | *1.0±0.2* |
| ***Pb*** | *0.98±0.04* | *0.95±0.03* | *1.2±0.0* |
| **Rb** | **1.46±0.08** | **1.9±0.1** | **2.1±0.1** |
| **Sn** | *1.06±0.08* | **1.13±0.09** | **3.8±0.9** |
| **Sr** | **1.78±0.06** | **2.5±0.1** | **1.84±0.06** |
| **Ta** | *1.04±0.08* | **1.12±0.09** | *1.0±0.1* |
| ***Th*** | *1.01±0.04* | *1.06±0.04* | *0.93±0.03* |
| **Ti** | **1.04±0** | **1.08±0** | *1.0±0.0* |
| ***U*** | *0.98±0.06* | *1.02±0.06* | *0.85±0.05* |
| ***V*** | *1.01±0.04* | *1.05±0.04* | *0.90±0.03* |
| ***W*** | *0.85±0.00* | *0.90±0.04* | *0.95±0.07* |
| **Zn** | *0.96±0.01* | *0.99±0.01* | **1.23±0.01** |
| ***Zr*** | *1.01±0.02* | *1.0±0.0* | *0.98±0.02* |

### 3.3.4 Rare Earth Element (REE) concentration

#### 3.3.4.1 REE distribution in SWa-1

SWa-1 was analyzed for REE composition. All elements analyzed have been normalized to the levels in unreacted SWa-1 (background) and presented in Table 4. Eu, Ho, Lu, Tb and Tm are all enriched throughout the experiment, with their highest enrichment level at the 504 hours reaction time. Er was enriched after the first 8 hours but became slightly depleted after 120 hours, followed by enrichment after 504 hours. Dy, Gd, La, Pr, Sm, Y and Yb were only enriched after 504 hours. Ce, Nd and Sc were consistently depleted throughout the reaction times.

**Table 4: REE enrichment levels and uncertainty in reacted Fe-rich smectite in alphabetical order (> 1 = enriched (Bold), < = depleted (*Italics*)). Uncertainty = E* [((std dev R)/R)^2+((std dev U)/U)^2]^0.5, where E is enrichment, R is concentration in reacted sample and U is concentration in unreacted sample.**

| Element | SWa-1_8hours | SWa-1_120 hours | SWa-1_504 hours |
|---|---|---|---|
| ***Ce*** | *0.85±0.04* | *0.89±0.04* | *0.97±0.05* |
| **Dy** | *0.90±0.01* | *0.88±0.01* | **1.12±0.01** |
| **Er** | *1.04±0.02* | *0.92±0.02* | **1.37±0.03** |
| **Eu** | **1.19±0.05** | *1.08±0.05* | **1.46±0.07** |
| ***Gd*** | *0.93±0.01* | *0.89±0.01* | *1.08±0.01* |
| **Ho** | **1.30±0.03** | *1.06±0.03* | **1.79±0.04** |
| ***La*** | *0.9±0.0* | *0.9±0.0* | *1.03±0.01* |
| **Lu** | **1.75±0.07** | **1.19±0.05** | **2.73±0.07** |
| ***Nd*** | *0.9±0.0* | *0.9±0.0* | *0.97±0.00* |
| **Pr** | *0.9±0.0* | *1.0±0.1* | **1.12±0.00** |
| ***Sc*** | *1.0±0.0* | *0.9±0.0* | *0.9±0.0* |
| ***Sm*** | *0.94±0.0* | *0.94±0.0* | *1.1±0.0* |
| **Tb** | **1.31±0.06** | *1.05±0.06* | **1.80±0.09** |
| **Tm** | **1.71±0.02** | **1.17±0.04** | **2.62±0.07** |
| ***Y*** | *0.81±0.02* | *0.85±0.02* | *1.02±0.03* |
| **Yb** | *0.97±0.04* | *0.87±0.03* | **1.35±0.05** |

### 3.3.4.2 REE distribution in SAz-1

Analysis of REE in reacted SAz-1 normalized to levels in unreacted SAz-1 (Table 5), shows there is very negligible enrichment of REEs throughout the reaction time. Only Lu shows a slight enrichment throughout the experiment. Apart from Lu, no other REE is enriched after the 504 hours reaction time. Dy, Eu, and Y show slight enrichment after the first 120 hours of SAz-1 in the spring but were depleted after the initial enrichment. Ce, Er, Gd, Ho, La, Nd, Pr, Sc, Sm, Tb, Tm

and Yb all were either unchanged or depleted after the first 12 hours and then further depleted after 504 hours.

**Table 5: REE enrichment levels and uncertainty in reacted Al-rich smectite in alphabetical order (> 1 = enriched, < 1 = depleted). Uncertainty = E* [((std dev R)/R)^2+((std dev U)/U)^2]^0.5, where E is enrichment, R is concentration in reacted sample and U is concentration in unreacted sample.**

| Element | SAz-1_8hours | SAz-1_120 hours | SAz-1_504 hours |
|---|---|---|---|
| ***Ce*** | *0.98±0.04* | *1.05±0.04* | *0.87±0.04* |
| ***Dy*** | *1.01±0.05* | *1.10±0.05* | *0.92±0.04* |
| ***Er*** | *0.97±0.05* | *1.04±0.06* | *0.91±0.05* |
| ***Eu*** | *1.07±0.06* | *1.11±0.06* | *1.0±0.1* |
| ***Gd*** | *1.05±0.05* | *1.07±0.05* | *0.93±0.04* |
| ***Ho*** | *1.04±0.06* | *1.08±0.06* | *0.91±0.05* |
| ***La*** | *1.0±0.0* | *1.04±0.03* | *0.93±0.02* |
| ***Lu*** | *1.13±0.00* | *1.14±0.00* | *1.1±0.0* |
| ***Nd*** | *1.00±0.02* | *1.06±0.03* | *0.92±0.02* |
| ***Pr*** | *1.01±0.02* | *1.04±0.02* | *0.92±0.02* |
| ***Sc*** | *0.93±0.02* | *0.82±0.01* | *0.84±0.01* |
| ***Sm*** | *1.01±0.07* | *1.06±0.07* | *0.93±0.06* |
| ***Tb*** | *1.01±0.08* | *1.05±0.08* | *0.93±0.07* |
| ***Tm*** | *1.0±0.1* | *1.1±0.1* | *0.9±0.1* |
| ***Y*** | *1.04±0.05* | *1.11±0.05* | *0.92±0.04* |
| ***Yb*** | *1.0±0.1* | *1.1±0.1* | *0.94±0.04* |

## 3.4 Discussion

### 3.4.1 Trace element sequestration in a modern euxinic spring with respect to smectite composition

The reaction of SWa-1 (Fe-rich) and SAz-1 (Al-rich) smectite with a natural modern euxinic spring led to distinct variations in trace metal enrichment, revealing a dynamic sequence of geochemical

interactions between the clay and aqueous conditions during exposure to the sulfidic spring. The reduction of structural Fe(III) to Fe(II) in SWa-1 to a much greater extent than SAz-1 (Figure 1) significantly alters its surface reactivity by generating more adsorption sites, new potential binding mechanisms, and increasing layer charge, thereby affecting trace element adsorption and absorption[24,26,30,41]. For example, Fe (III) reduction in Fe-rich smectite generates increased sorption sites on the edges of the clay[23]. Increased layer charge generates additional Cation Exchange Capacity (CEC) for metal immobilization in smectite clay interlayers and basal surfaces. We hypothesized that the Fe (III) reduction in the reacted Fe-rich smectite will generate increased cation exchange capacity, so we calculated the inner layer milliequivalent per 100 g of all the cations that are expected to be in the interlayer of the clay from the TEM-EDX analysis. We found out that our result is consistent with the hypothesis (Figure 3a-3b).

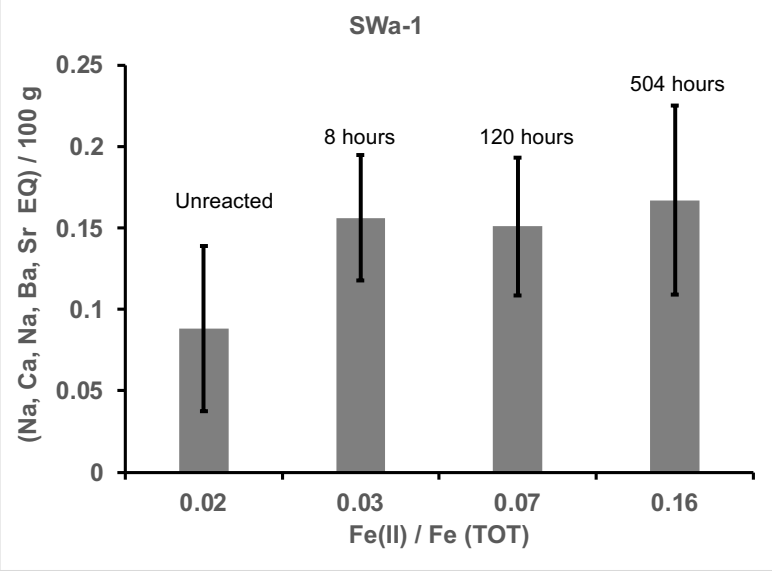


Figure 3a: Increasing interlayer cations (Na, Ca, K, Sr and Ba) with increasing Fe(III) reduction in Fe-rich smectite.

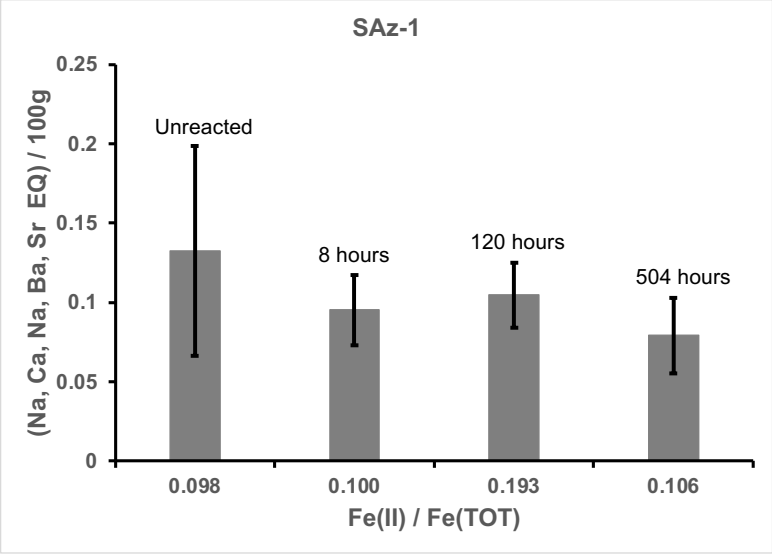


Figure 3b: Interlayer cations (Na, Ca, K, Sr and Ba) trend with increasing reaction time of Al-rich smectite in the spring.

We observed that the enrichment of Ba, Cs, Rb, and Sr (Figure 4) increases coincidentally with increasing Fe(III) reduction in SWa-1 as reaction time progresses (Figure 1). In SAz-1, Ba, Cs, Rb, and Sr have similar trend as SWa-1, however, the enrichment levels of these elements in SAz-1 (5.41, 2.31, 2.07, and 1.84, respectively) are much lower than that of SWa-1 (106.11, 3.15, 7.77, and 7.2). We believe the much greater enrichments in the Fe-rich smectite reflects a mechanistic connection with Fe(III) reduction to Fe(II) in the smectite. Octahedral sheet cation redox changes generate extra adsorption capacity / sites that either does not occur or is negligible in aluminous SAz-1.

The Fe content in SAz-1 is low (1.77 wt.%)[42,43] compared to SWa-1 (12.6 wt.%) . Fe in smectites with low Fe contents remain oxidized at lower oxidation potential than Fe-rich smectites (i.e., they are less easily reduced), as demonstrated previously for Fe-rich SWa-1, NAu-1, NAu-2, and low-iron SWy-2[44]. Therefore, low-Fe SAz-1 is less susceptible to reduction than SWa-1, and the Fe-

rich clay acts as a better sink for these trace elements. Sn is enriched throughout the reaction time in SAz-1 (Figure 4) but was depleted after 8 hours in SWa-1 (Figure 6).

Furthermore, the euxinic spring is rich in Ba and Sr, creating a steady supply of Ba and Sr. While some of the Ba and Sr recorded in reacted SWa-1 and SAz-1 would be in the interlayer of the clay, as S/TEM scans for Ba and Sr in SWa-1 are similar to other interlayer cations like Ca and K (Figure 6), we believe that most of the Ba and Sr are immobilized as barite, celestine or other solid phase sulfur-bearing minerals[45]. Moreso, there is a contribution of inherited barite from the spring to the Ba[39] and possibly Sr[46] pool seen in the reacted SWa-1. We believe that some of the Ba and Sr seen in reacted SAz-1 are inherited from the microbially-generated barite in the spring itself and are not entirely adsorbed unto the clay. However, surface complexation reactions and cation exchange will be responsible for the accumulation of these trace elements.

We believe that Fe reduction in Fe-rich smectites promotes irreversible $Cs^+$ and $Rb^+$ fixation in collapsed interlayers due to their low hydration energy. While $Rb^+$ adsorption is generally weaker than $Cs^+$, the presence of higher concentration of Rb than Cs in the euxinic spring favors more Rb adsorption to both reacted SWa-1 and SAz-1[18,47].

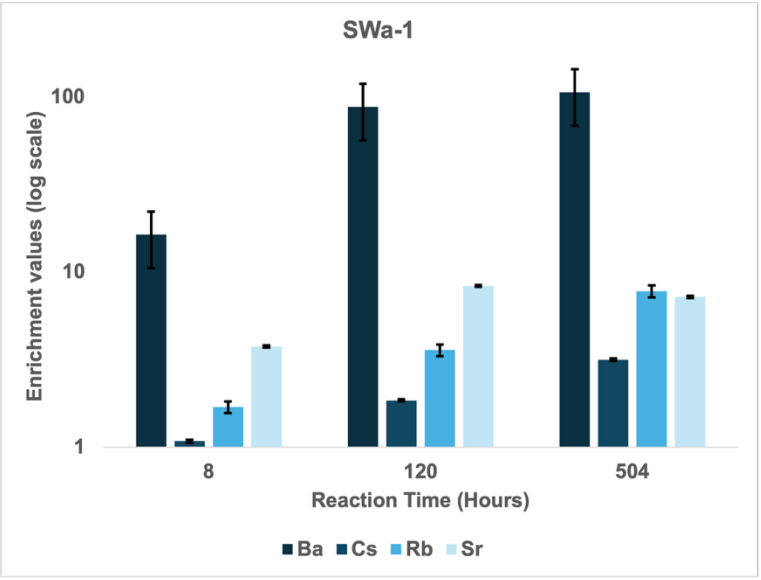


Figure 3: Ba, Cs, Rb, Sr and Sn enrichment levels in Fe-rich smectite over 504 hours of reaction in the euxinic spring

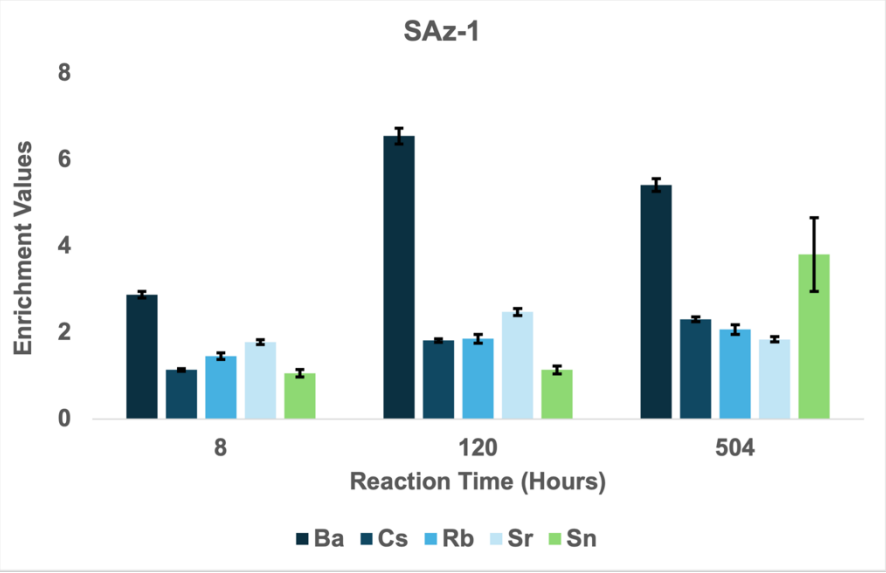


Figure 4: Ba, Cs, Rb, Sr and Sn enrichment levels in Al-rich smectite over 504 hours of reaction in the euxinic spring

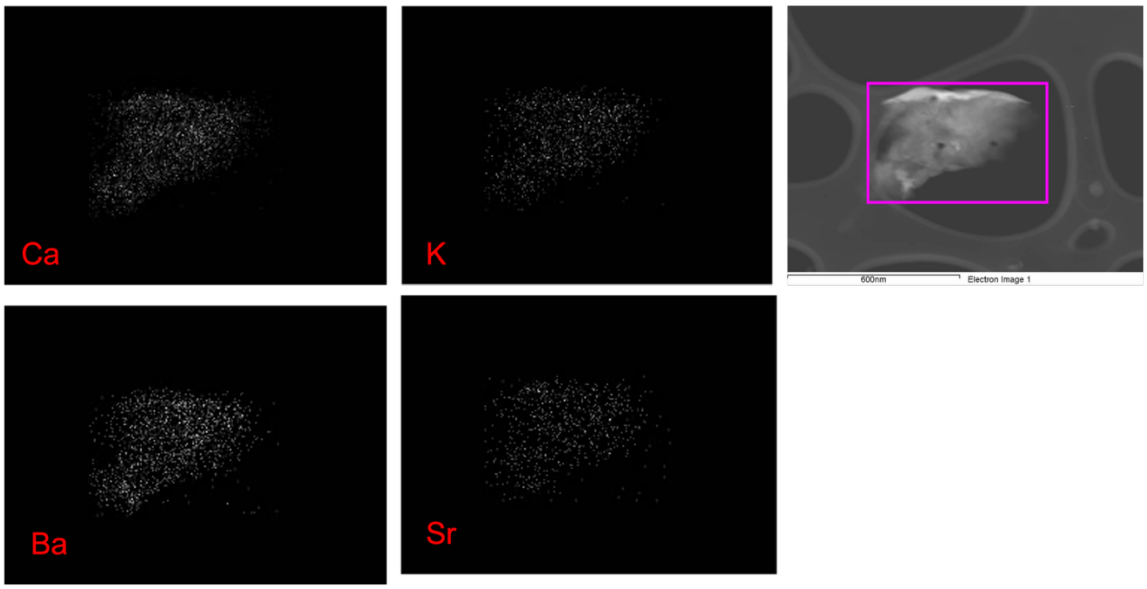


Figure 5: S/TEM scans of selected cations in reacted Fe-rich smectite after 504 hours in the spring showing similar enrichment trends in Ca, K, Ba and Sr

Our results demonstrate that chalcophilic elements Sn, Cu, Zn and Pb in SWa-1 were enriched after the initial hours of the reaction but then were measured at or just below their initial values for the remainder of the experiment (Figure 7). The rapid enrichment and subsequent depletion of Sn, Cu, Zn and Pb in the SWa-1 is possibly due to the fact that as Fe-reduction progresses, monovalent cations begin to replace divalent cations in the interlayer except for in the case of Ba and Sr. Another possible explanation for the initial enrichment of Sn, Cu, Zn and Pb in the clay likely resulted from their strong affinity for sulfide species, forming insoluble sulfides (e.g., CuS, PbS, $SnS_2$) under sulfidic conditions[10,48,49]. Mobile Fe(II) produced from Fe(III) reduction and clay dissolution (Figure 8) can readily react with sulfide in the spring to precipitate solid phase Fe-S species that are capable of immobilizing trace elements in their structure[10,15,15,48]. These metals are known to exhibit high chalcophilic tendencies, leading to their immediate sequestration as solid phases. However, their subsequent depletion could be as a result of colloidal instability or competition for adsorption sites from other cations in solution. However, in SAz-1, the enrichment

of Cu, Pb and Zn after a long time in the spring suggests they are preferred over other trace cations in SAz-1 in the long term. Cu is the dominant trace cation with over 9-fold enrichment after 504 hours of SAz-1 in the spring. This is even more than Ba enrichment in reacted SAz-1. This is probably due to the high charge density of Cu (small ionic radius: 0.73 Å) and intermediate hydration energy, making it more selective than larger divalent cations like Ba.

In contrast, the largely lithophilic elements Cr, Ga, Hf, Nb, Ta, Th, Ti, U, W, and Zr were generally enriched in reduced SWa-1 after the depletion of the chalcophilic elements (Figure 9). This trend can be attributed to differences in metal solubility, redox sensitivity, and affinity for sulfidic and clay mineral surfaces under anoxic conditions[50–53]. The delayed enrichment of Cr, G, Hf, Nb, Ta, Th, Ti, U, W, and Zr suggests different retention and release mechanisms and the effect of increased adsorption sites in reduced SWa-1. These elements are less prone to sulfide precipitation, and their behavior is instead controlled by redox transformations and interactions with clay mineral surfaces. Under anoxic conditions, Cr(VI) (if initially present) can be reduced to Cr(III), which has a strong tendency to adsorb onto clay minerals. Reduced Swa-1 is a better sink for Cr in this study while SAz-1 exhibits a short-term sink. $Ga^{3+}$ exhibits geochemical behavior similar to $Al^{3+}$ and $Fe^{3+}$, forming hydrolyzed species that can adsorb onto clay surfaces[54,55]. Highly hydrolyzed cations, Hf, Nb, Ta, Th, Ti, U, W, and Zr tend to form strong complexes with oxygen ligands, including clay siloxane surfaces[56,57]. The switch from divalent trace elements to high valence trace elements coincide with increasing Fe(III) reduction to Fe (II) trend observed. This means their delayed enrichment is connected to Fe (III) reduction generating more adsorption sites on the clay edges. High-valence cations primarily bind to clay edge sites (≡S–OH) via inner-sphere complexation or ion exchange[56–58]. At neutral pH, most high valence cations hydrolyze and precipitate or form strong surface complexes[56].

However, in SAz-1, we see what looks like a mirror image of the behavior of double valent cations versus multivalent cations in SWa-1. Our findings demonstrate an initial enrichment of Cr, Ga, Hf, Sr, Ta, Th, V, Zr and Li (Figure 10) within the first 120 hours of SAz-1 in the spring, followed by their subsequent depletion and a later enrichment of Cu, Pb and Zn (Figure 11). Additionally, Cr and U **e**xhibited a short-term enrichment phase between these two stages.

Apart from SWa-1 interlayer being a sequestration site for these trace elements, Fe-sulfides (e.g., pyrite, mackinawite) which are possible products of structural Fe reduction by sulfide in Fe-rich smectite, can sequester redox-sensitive metals V, Pb, Zn, Cr, U, Cu via structural incorporation or surface adsorption. The preferential accumulation of trace elements in the reacted SWa-1 are controlled by the law of mass action and the degree of Fe (III) reduction in SWa-1.

The result of our experiment shows similar trace element enrichments in the Black Sea[9]. The euxinic sediments of the Black Sea characterized by reducing and sulfidic conditions are enriched in redox sensitive trace elements such as Cr and U which is similar to what we have seen in our experiment. Also, sulfide precipitation plays an important role in chalcophilic trace elements accumulation in the Black Sea and other euxinic basins[59].

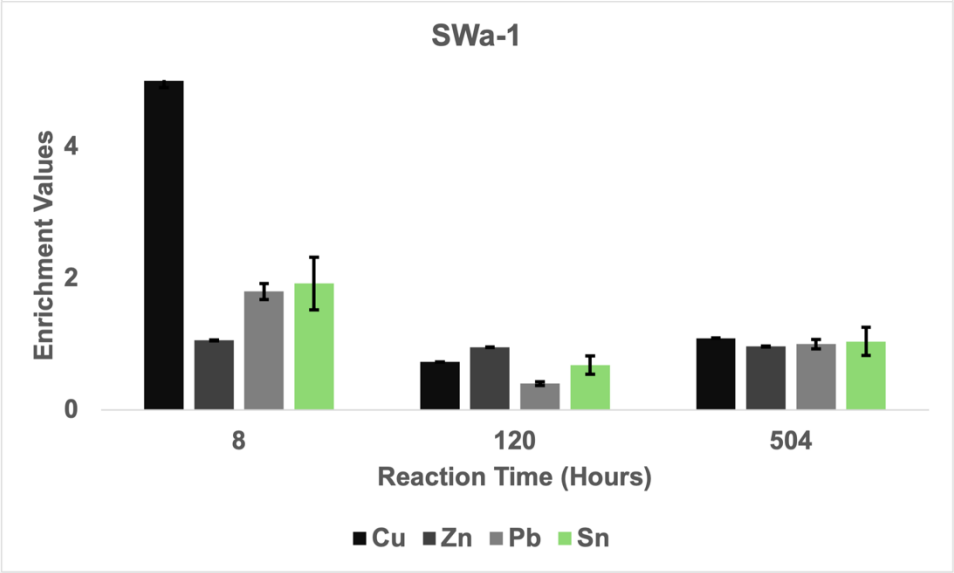


Figure 6: Cu, Zn, Pb and Sn enrichment levels in Fe-rich smectite over 504 hours of reaction in the euxinic spring

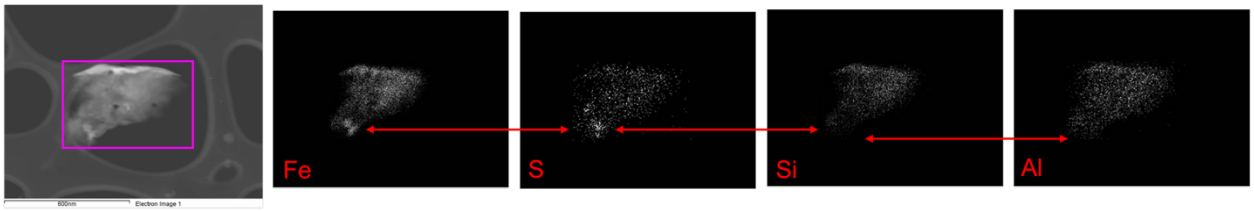


Figure 7: S/TEM image showing Fe-S mineralization with Si and Al loss in reacted Fe-rich smectite after 504 hours. The arrows show Fe-S mineralization at the edges where Si and Al is lost.

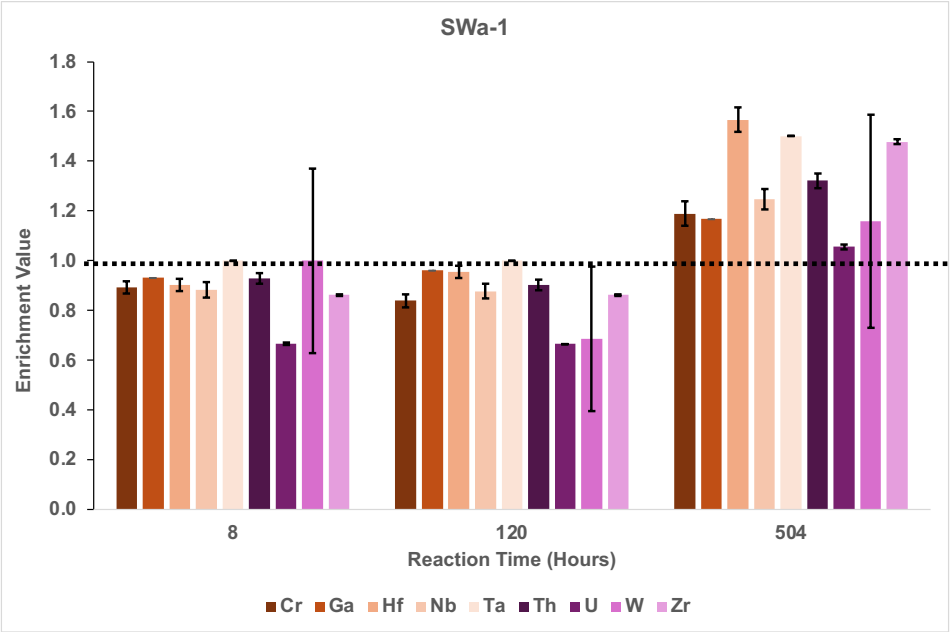


Figure 8: Cr, Ga, Hf, Nb, Ta, Th, U, W and Zr enrichment levels in Fe-rich smectite over 504 hours of reaction in the euxinic spring

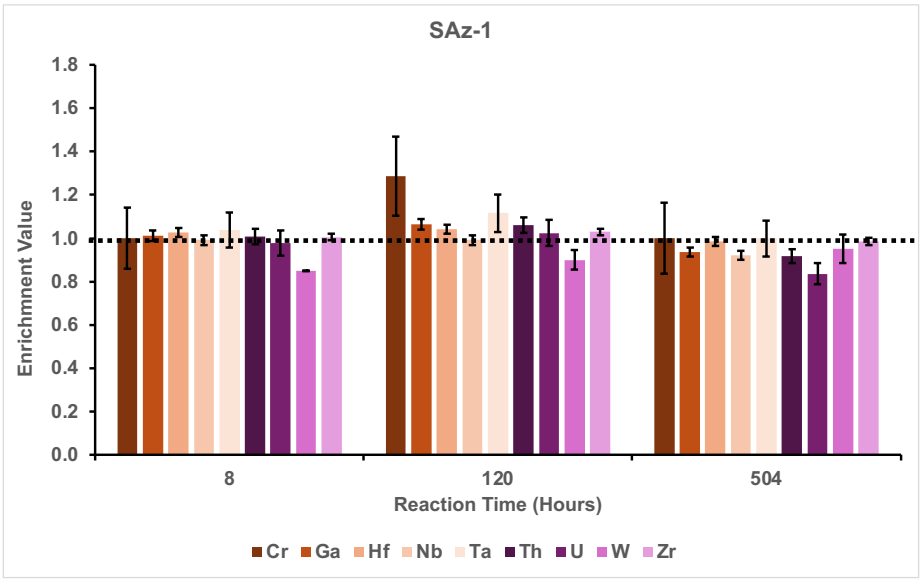


Figure 9: Cr, Ga, Hf, Nb, Ta, Th, U, W and Zr enrichment levels in Al-rich smectite over 504 hours of reaction in the euxinic spring

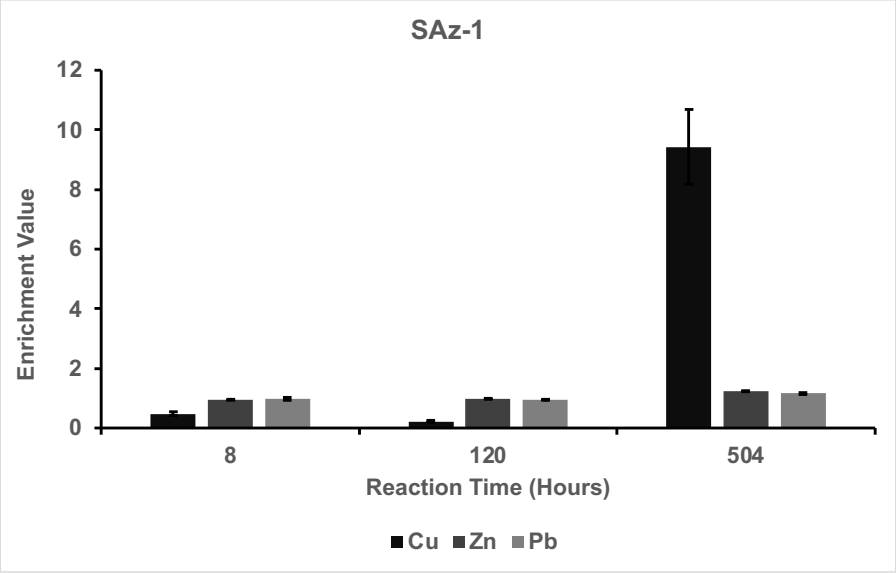


Figure 10: Cu, Zn and Pb enrichment levels in Al-rich smectite over 504 hours of reaction in the euxinic spring

### 3.4.2 Impact of euxinic condition on REE distribution in smectite

Our analysis shows SWa-1 to be a sink for most REEs such as Lu and Tm with over double-fold enrichment in both (2.73 and 2.62 respectively). Only Ce, Nd and Sc were consistently depleted throughout the reaction time. This is probably due to competition from other cations. Eu, Ho, Lu, Tb and Tm are consistently enriched throughout the experiment while Dy, Gd, La, Pr, Sm, Y and Yb accumulated only after 504 hours in the spring. It is interesting to see that despite the high concentration of Eu in the spring, we do not see high accumulation of Eu in the clays. This could be due to kinetic limitations that could be explained over a longer experiment time. Our study shows that increasing Fe (III) reduction facilitated increased REE sorption to the clay surface. SAz-1 on the hand is a poor sink for these REEs. There was barely any REE enrichment throughout the experiment time, at least for the 504 hours.

Al-rich clays such as kaolinite have been proven to be good sink for REEs[3,60], however our study shows that Al-rich smectite is not a good sink for REEs, at least over a period of 504 hours.

Kaolinite, unlike Al-rich smectite does not have inner layer in its structure, making edge sorption the dominant process of cation sorption. The edge sorption strongly binds hydrolyzed REEs without competition from weakly bound inner layer cations as in Al-rich smectite.

## 3.5 Broader Implication and Conclusions

The experimental interaction of Fe-rich smectite SWa-1 and Fe-poor smectite SAz-1 with a modern euxinic spring shows dynamic trace element and REE mobilization, with different stages of enrichment and depletion over a period of 504 hours. Our study gives insights into trace element cycling in ancient sulfidic marine basins, where reduced Fe-rich clay minerals may have acted as both temporary sinks and sources of bio-essential metals (e.g., Cu, Zn) and a potential long-term sink for redox-sensitive elements (e.g., Cr).

Furthermore, in the event of future euxinia in the modern-day oceans, the initial enrichment and subsequent depletion of Zn and Cu imply that, under expanding euxinia in the presence of Fe-rich clays, these micronutrients may become temporarily more bioavailable before being sequestered in sulfidic sediments. This could affect phytoplankton community dynamics, particularly for organisms with high Zn and Cu demands. Al-rich smectite would be a sink for these bio-essential trace elements, inhibiting their availability to the bio-community that needs them.

The subsequent shift from divalent trace elements towards higher valence trace elements shows reduced Fe-smectite are effective sinks for high valence trace elements like Cr(III), Ga(III), Hf(IV), Nb(IV), Ta(V), Th(IV), Ti(IV), U(IV), W(VI), and Zr(IV). This attribute is useful both in metal remediation processes and paleo redox reconstruction. With the presence of Fe-rich smectites and evidence of past sulfidic conditions on Mars, similar processes could have influenced trace element availability in ancient Martian groundwater. The detection of similar enrichment sequence e.g. Zn, Cu, Pb and Zn depletion followed by high valence trace elements

enrichment in Martian clay strata by rover missions could be a signal of redox gradients and a sign of potential microbial habitability. Attempts have been made to understand the chemostratigraphy on Mars with studies showing the presence of smectites, sulfates, silica and oxides on Mars[61,62]. However, the observed trends of interaction between the clays and trace elements in neutral pH euxinic water as seen in our study could be indicative of neutral pH hydrology and habitable lakes on the early Mars.

The reverse trend observed in SAz-1 where Cu, Pb, and Zn are immobilized with longer exposure to euxinic condition could suggests that Al-rich smectites on the early earth and Mars may have sequestered bio-essential metals, possibly influencing nutrient availability for any potential microbial life. The observed behavior of Ba and Sr supports their potential as paleoenvironmental proxies in Proterozoic anoxic sediments.

With increasing demands for REEs especially towards clean energy transition, our study has shown that reduced Fe-rich smectite are potentially effective traps or sources of important REEs such as Lu and Tm used in laser production for medical applications, Dy and Tb needed for renewable energy infrastructure, Pr and Y useful in superconductor production, and Eu for light emitting diodes (LEDs) manufacturing.

## Acknowledgements

We thank Emma Bachman and Desiree Hullaster for assistance with sampling the spring water, and Dr. Yongjun Gao from the University of Houston for handling the ICP analyses. We also thank Dani Storms and Dr. Caitlin Hodges for help with deploying clay samples into the spring. We acknowledge funding support from the University of Oklahoma Joe and Robert Klabzuba Chair and NASA grant 22-HW22_2-0005.

## References


(1) Mukherjee, I.; Large, R. R. Co-Evolution of Trace Elements and Life in Precambrian Oceans: The Pyrite Edition. *Geology* **2020**, *48* (10), 1018–1022. https://doi.org/10.1130/G47890.1.

(2) Xu, Y.; Cao, J.; Jiang, L.; Zhang, Y. Biogeographic and Evolutionary Patterns of Trace Element Utilization in Marine Microbial World. *Genomics Proteomics Bioinformatics* **2021**, *19* (6), 958–972. https://doi.org/10.1016/j.gpb.2021.02.003.

(3) Yang, M.; Liang, X.; Ma, L.; Huang, J.; He, H.; Zhu, J. Adsorption of REEs on Kaolinite and Halloysite: A Link to the REE Distribution on Clays in the Weathering Crust of Granite. *Chem. Geol.* **2019**, *525*, 210–217. https://doi.org/10.1016/j.chemgeo.2019.07.024.

(4) Moldoveanu, G. A.; Papangelakis, V. G. Recovery of Rare Earth Elements Adsorbed on Clay Minerals: I. Desorption Mechanism. *Hydrometallurgy* **2012**, *117–118*, 71–78. https://doi.org/10.1016/j.hydromet.2012.02.007.

(5) Li, M. Y. H.; Zhou, M.-F. The Role of Clay Minerals in Formation of the Regolith-Hosted Heavy Rare Earth Element Deposits. *Am. Mineral.* **2020**, *105* (1), 92–108. https://doi.org/doi:10.2138/am-2020-7061.

(6) Atienza, N. M. M.; Gregory, D. D.; Taylor, S. D.; Swing, M.; Perea, D. E.; Owens, J. D.; Lyons, T. W. Refined Views of Ancient Ocean Chemistry: Tracking Trace Element Incorporation in Pyrite Framboids Using Atom Probe Tomography. *Geochim. Cosmochim. Acta* **2023**, *357*, 1–12. https://doi.org/10.1016/j.gca.2023.07.013.

(7) Gilleaudeau, G. J.; Sahoo, S. K.; Ostrander, C. M.; Owens, J. D.; Poulton, S. W.; Lyons, T. W.; Anbar, A. D. Molybdenum Isotope and Trace Metal Signals in an Iron-Rich Mesoproterozoic Ocean: A Snapshot from the Vindhyan Basin, India. *Precambrian Res.* **2020**, *343*, 105718. https://doi.org/10.1016/j.precamres.2020.105718.

(8) Gregory, D.; Mukherjee, I.; Olson, S. L.; Large, R. R.; Danyushevsky, L. V.; Stepanov, A. S.; Avila, J. N.; Cliff, J.; Ireland, T. R.; Raiswell, R.; Olin, P. H.; Maslennikov, V. V.; Lyons, T. W. The Formation Mechanisms of Sedimentary Pyrite Nodules Determined by Trace Element and Sulfur Isotope Microanalysis. *Geochim. Cosmochim. Acta* **2019**, *259*, 53–68. https://doi.org/10.1016/j.gca.2019.05.035.

(9) Gregory, D. D.; Lyons, T. W.; Large, R. R.; Stepanov, A. S. Ground-Truthing the Pyrite Trace Element Proxy in Modern Euxinic Settings. *Am. Mineral.* **2022**, *107* (5), 848–859. https://doi.org/10.2138/am-2022-8024.

(10) Rickard, D. Euxinic Systems. In *Developments in Sedimentology*; Elsevier, 2012; Vol. 65, pp 495–542. https://doi.org/10.1016/B978-0-444-52989-3.00013-1.

(11) Snow, L. J.; Duncan, R. A.; Bralower, T. J. Trace Element Abundances in the Rock Canyon Anticline, Pueblo, Colorado, Marine Sedimentary Section and Their Relationship to Caribbean Plateau Construction and Oxygen Anoxic Event 2: OAE2 linked to hydrothermal activity. *Paleoceanography* **2005**, *20* (3), n/a-n/a. https://doi.org/10.1029/2004PA001093.

(12) Taylor, S. D.; Gregory, D. D.; Perea, D. E.; Kovarik, L.; Cliff, J. B.; Lyons, T. W. Pushing the Limits: Resolving Paleoseawater Signatures in Nanoscale Fluid Inclusions by Atom Probe Tomography. *Earth Planet. Sci. Lett.* **2022**, *599*, 117859. https://doi.org/10.1016/j.epsl.2022.117859.

(13) Jenkyns, H. C. Geochemistry of Oceanic Anoxic Events: REVIEW. *Geochem. Geophys. Geosystems* **2010**, *11* (3), n/a-n/a. https://doi.org/10.1029/2009GC002788.

(14) Tribovillard, N.; Algeo, T. J.; Lyons, T.; Riboulleau, A. Trace Metals as Paleoredox and Paleoproductivity Proxies: An Update. *Chem. Geol.* **2006**, *232* (1–2), 12–32. https://doi.org/10.1016/j.chemgeo.2006.02.012.

(15) Rickard, D.; Luther, G. W. Chemistry of Iron Sulfides. *Chem. Rev.* **2007**, *107* (2), 514–562. https://doi.org/10.1021/cr0503658.

(16) Lyons, T. W.; Severmann, S. A Critical Look at Iron Paleoredox Proxies: New Insights from Modern Euxinic Marine Basins. *Geochim. Cosmochim. Acta* **2006**, *70* (23), 5698–5722. https://doi.org/10.1016/j.gca.2006.08.021.

(17) Robin, V.; Tertre, E.; Beaufort, D.; Regnault, O.; Sardini, P.; Descostes, M. Ion Exchange Reactions of Major Inorganic Cations (H+, Na+, Ca2+, Mg2+ and K+) on Beidellite: Experimental Results and New Thermodynamic Database. Toward a Better Prediction of Contaminant Mobility in Natural Environments. *Appl. Geochem.* **2015**, *59*, 74–84. https://doi.org/10.1016/j.apgeochem.2015.03.016.

(18) Ohnuki, T.; Kozai, N. Sorption Characteristics of Radioactive Cesium and Strontium on Smectite. *Radiochim. Acta* **1994**, *66–67* (Supplement), 327–332. https://doi.org/10.1524/ract.1994.6667.special-issue.327.

(19) Vejsada, J.; Hradil, D.; Řanda, Z.; Jelínek, E.; Štulík, K. Adsorption of Cesium on Czech Smectite-Rich Clays—A Comparative Study. *Appl. Clay Sci.* **2005**, *30* (1), 53–66. https://doi.org/10.1016/j.clay.2005.03.003.

(20) Apalara, I. T.; Hodges, C.; Sabisch, J. E. C.; Elwood Madden, M. E.; Larson, P. R.; Elwood Madden, A. S. Understanding the Impact of a Modern Euxinic Spring on Sediment Using Bulk Sediment and Smectite Clay-Preserved Proxies. *ACS Earth Space Chem.* **2025**, *9* (2), 265–276. https://doi.org/10.1021/acsearthspacechem.4c00269.

(21) Morse, J. W. Interactions of Trace Metals with Authigenic Sulfide Minerals: Implications for Their Bioavailability. *Mar. Chem.* **1994**, *46* (1–2), 1–6. https://doi.org/10.1016/0304-4203(94)90040-x.

(22) Sundelin, B.; Eriksson, A.-K. Mobility and Bioavailability of Trace Metals in Sulfidic Coastal Sediments. *Environ. Toxicol. Chem.* **2001**, *20* (4), 748–756. https://doi.org/10.1002/etc.5620200408.

(23) Stucki, J. W. Properties and Behaviour of Iron in Clay Minerals. In *Developments in Clay Science*; Elsevier, 2013; Vol. 5, pp 559–611. https://doi.org/10.1016/B978-0-08-098258-8.00018-3.

(24) Stucki, J. W.; Lee, K.; Zhang, L.; Larson, R. A. Effects of Iron Oxidation State on the Surface and Structural Properties of Smectites. *Pure Appl. Chem.* **2002**.

(25) Stucki, J. W.; Golden, D. C.; Roth, C. B. Effects of Reduction and Reoxidation of Structural Iron on the Surface Charge and Dissolution of Dioctahedral Smectites. *Clays Clay Miner.* **1984**, *32* (5), 350–356.

(26) Stucki, J. W. A Review of the Effects of Iron Redox Cycles on Smectite Properties. *Comptes Rendus Geosci.* **2011**, *343* (2–3), 199–209. https://doi.org/10.1016/j.crte.2010.10.008.

(27) Gorski, C. A.; Aeschbacher, M.; Soltermann, D.; Voegelin, A.; Baeyens, B.; Marques Fernandes, M.; Hofstetter, T. B.; Sander, M. Redox Properties of Structural Fe in Clay Minerals. 1. Electrochemical Quantification of Electron-Donating and -Accepting Capacities of Smectites. *Environ. Sci. Technol.* **2012**, *46* (17), 9360–9368. https://doi.org/10.1021/es3020138.

(28) Stucki, J. W.; Kostka, J. E. Microbial Reduction of Iron in Smectite. *Comptes Rendus Geosci.* **2006**, *338* (6), 468–475. https://doi.org/10.1016/j.crte.2006.04.010.

(29) Jaisi, D. P.; Kukkadapu, R. K.; Eberl, D. D.; Dong, H. Control of Fe(III) Site Occupancy on the Rate and Extent of Microbial Reduction of Fe(III) in Nontronite. *Geochim. Cosmochim. Acta* **2005**, *69* (23), 5429–5440. https://doi.org/10.1016/j.gca.2005.07.008.

(30) Stucki, J. W. Properties and Behaviour of Iron in Clay Minerals. In *Developments in Clay Science*; Elsevier, 2013; Vol. 5, pp 559–611. https://doi.org/10.1016/B978-0-08-098258-8.00018-3.

(31) Stucki, J. W.; Bailey, G. W.; Gan, H. Oxidation-Reduction Mechanisms in Iron-Bearing Phyllosilicates. *Appl. Clay Sci.* **1996**, *10* (6), 417–430. https://doi.org/10.1016/0169-1317(96)00002-6.

(32) Liu, D.; Wang, F.; Dong, H.; Wang, H.; Zhao, L.; Huang, L.; Wu, L. Biological Reduction of Structural Fe(III) in Smectites by a Marine Bacterium at 0.1 and 20MPa. *Chem. Geol.* **2016**, *438*, 1–10. https://doi.org/10.1016/j.chemgeo.2016.05.020.

(33) Yang, S.; Liu, D.; Zheng, W.; Fan, Q.; Wang, H.; Zhao, L. Microbial Reduction and Alteration of Fe(III)-Containing Smectites in the Presence of Biochar-Derived Dissolved Organic Matter. *Appl. Geochem.* **2023**, *152*, 105661. https://doi.org/10.1016/j.apgeochem.2023.105661.

(34) Veith, J. A.; Jackson, M. L. Iron Oxidation and Reduction Effects on Structural Hydroxyl and Layer Charge in Aqueous Suspensions of Micaceous Vermiculites. *Clays Clay Miner.* **1974**, *22* (4), 345–353. https://doi.org/10.1346/CCMN.1974.0220405.

(35) Stucki, J. W.; Roth, C. B. Interpretation of Infrared Spectra of Oxidized and Reduced Nontronite. *Clays Clay Miner.* **1976**, *24* (6), 293–296. https://doi.org/10.1346/CCMN.1976.0240604.

(36) Dodds, W. K.; Bouska, W. W.; Eitzmann, J. L.; Pilger, T. J.; Pitts, K. L.; Riley, A. J.; Schloesser, J. T.; Thornbrugh, D. J. Eutrophication of U.S. Freshwaters: Analysis of Potential Economic Damages. *Environ. Sci. Technol.* **2009**, *43* (1), 12–19. https://doi.org/10.1021/es801217q.

(37) Le Moal, M.; Gascuel-Odoux, C.; Ménesguen, A.; Souchon, Y.; Étrillard, C.; Levain, A.; Moatar, F.; Pannard, A.; Souchu, P.; Lefebvre, A.; Pinay, G. Eutrophication: A New Wine in an Old Bottle? *Sci. Total Environ.* **2019**, *651*, 1–11. https://doi.org/10.1016/j.scitotenv.2018.09.139.

(38) Sanders, W. E. Rate and Mechanism of Barite Mineralization at Zodletone Mountain, Southwestern Oklahoma. PhD Thesis, University of Oklahoma, 1998.

(39) Senko, J. M.; Campbell, B. S.; Henriksen, J. R.; Elshahed, M. S.; Dewers, T. A.; Krumholz, L. R. Barite Deposition Resulting from Phototrophic Sulfide-Oxidizing Bacterial Activity. *Geochim. Cosmochim. Acta* **2004**, *68* (4), 773–780. https://doi.org/10.1016/j.gca.2003.07.008.

(40) Yong, S. N.; Lim, S.; Ho, C. L.; Chieng, S.; Kuan, S. H. Mechanisms of Microbial-Based Iron Reduction of Clay Minerals: Current Understanding and Latest Developments. *Appl. Clay Sci.* **2022**, *228*, 106653. https://doi.org/10.1016/j.clay.2022.106653.

(41) Neumann, A.; Sander, M.; Hofstetter, T. B. Redox Properties of Structural Fe in Smectite Clay Minerals. In *ACS Symposium Series*; Tratnyek, P. G., Grundl, T. J., Haderlein, S. B., Eds.; American Chemical Society: Washington, DC, 2011; Vol. 1071, pp 361–379. https://doi.org/10.1021/bk-2011-1071.ch017.

(42) Metz, V.; Amram, K.; Ganor, J. Stoichiometry of Smectite Dissolution Reaction. *Geochim. Cosmochim. Acta* **2005**, *69* (7), 1755–1772. https://doi.org/10.1016/j.gca.2004.09.027.

(43) Mermut, A. R. Baseline Studies of the Clay Minerals Society Source Clays: Chemical Analyses of Major Elements. *Clays Clay Miner.* **2001**, *49* (5), 381–386. https://doi.org/10.1346/CCMN.2001.0490504.

(44) Gorski, C. A.; Klüpfel, L. E.; Voegelin, A.; Sander, M.; Hofstetter, T. B. Redox Properties of Structural Fe in Clay Minerals: 3. Relationships between Smectite Redox and Structural Properties. *Environ. Sci. Technol.* **2013**, *47* (23), 13477–13485. https://doi.org/10.1021/es403824x.

(45) Tribovillard, N.; Algeo, T. J.; Lyons, T.; Riboulleau, A. Trace Metals as Paleoredox and Paleoproductivity Proxies: An Update. *Chem. Geol.* **2006**, *232* (1–2), 12–32. https://doi.org/10.1016/j.chemgeo.2006.02.012.

(46) Widanagamage; Griffith, E. M.; Singer, D. M.; Scher, H. D.; Buckley, W. P.; Senko, J. M. Controls on Stable Sr-Isotope Fractionation in Continental Barite. *Chem. Geol.* **2015**, *411*, 215–227. https://doi.org/10.1016/j.chemgeo.2015.07.011.

(47) Wampler, J. M.; Krogstad, E. J.; Elliott, W. C.; Kahn, B.; Kaplan, D. I. Long-Term Selective Retention of Natural Cs and Rb by Highly Weathered Coastal Plain Soils. *Environ. Sci. Technol.* **2012**, *46* (7), 3837–3843. https://doi.org/10.1021/es2035834.

(48) Rickard, D. Sedimentary Sulfides. In *Developments in Sedimentology*; Elsevier, 2012; Vol. 65, pp 543–604. https://doi.org/10.1016/B978-0-444-52989-3.00014-3.

(49) Rickard, D. Sulfur Chemistry in Aqueous Solutions. In *Developments in Sedimentology*; Elsevier, 2012; Vol. 65, pp 31–83. https://doi.org/10.1016/B978-0-444-52989-3.00002-7.

(50) Lee, J.-H.; Fredrickson, J. K.; Kukkadapu, R. K.; Boyanov, M. I.; Kemner, K. M.; Lin, X.; Kennedy, D. W.; Bjornstad, B. N.; Konopka, A. E.; Moore, D. A.; Resch, C. T.; Phillips, J. L. Microbial Reductive Transformation of Phyllosilicate Fe(III) and U(VI) in Fluvial Subsurface Sediments. *Environ. Sci. Technol.* **2012**, *46* (7), 3721–3730. https://doi.org/10.1021/es204528m.

(51) Maher, K.; Bargar, J. R.; Brown, G. E. Jr. Environmental Speciation of Actinides. *Inorg. Chem.* **2013**, *52* (7), 3510–3532. https://doi.org/10.1021/ic301686d.

(52) Edebali, S. *Advanced Sorption Process Applications*; IntechOpen, 2019.

(53) Yang, P.; Dai, S.; Nechaev, V. P.; Song, X.; Chekryzhov, I. Y.; Tarasenko, I. A.; Tian, X.; Yao, M.; Kang, S.; Zheng, J. Modes of Occurrence of Critical Metals (Nb-Ta-Zr-Hf-REY-Ga) in Altered Volcanic Ashes in the Xuanwei Formation, Eastern Yunnan Province, SW China: A Quantitative Evaluation Based on Sequential Chemical Extraction. *Ore Geol. Rev.* **2023**, *160*, 105617. https://doi.org/10.1016/j.oregeorev.2023.105617.

(54) Shiller, A. M.; Frilot, D. M. The Geochemistry of Gallium Relative to Aluminum in Californian Streams. *Geochim. Cosmochim. Acta* **1996**, *60* (8), 1323–1328. https://doi.org/10.1016/0016-7037(96)00002-6.

(55) Benézéth, P.; Diakonov, I. I.; Pokrovski, G. S.; Dandurand, J.-L.; Schott, J.; Khodakovsky, I. L. Gallium Speciation in Aqueous Solution. Experimental Study and Modelling: Part 2. Solubility of α-GaOOH in Acidic Solutions from 150 to 250°C and Hydrolysis Constants of Gallium (III) to 300°C. *Geochim. Cosmochim. Acta* **1997**, *61* (7), 1345–1357. https://doi.org/10.1016/S0016-7037(97)00012-4.

(56) Langmuir, D. *Aqueous Environmental Geochemistry*; Prentice Hall: Upper Saddle River, N.J, 1997.

(57) Bradbury, M. H.; Baeyens, B. Modelling the Sorption of Mn(II), Co(II), Ni(II), Zn(II), Cd(II), Eu(III), Am(III), Sn(IV), Th(IV), Np(V) and U(VI) on Montmorillonite: Linear Free Energy Relationships and Estimates of Surface Binding Constants for Some Selected Heavy Metals and Actinides. *Geochim. Cosmochim. Acta* **2005**, *69* (4), 875–892. https://doi.org/10.1016/j.gca.2004.07.020.

(58) Bradbury, M. H.; Baeyens, B. Sorption of Eu on Na- and Ca-Montmorillonites: Experimental Investigations and Modelling with Cation Exchange and Surface Complexation. *Geochim. Cosmochim. Acta* **2002**, *66* (13), 2325–2334. https://doi.org/10.1016/s0016-7037(02)00841-4.

(59) Rickard, D.; Luther, G. W. Chemistry of Iron Sulfides. *Chem. Rev.* **2007**, *107* (2), 514–562. https://doi.org/10.1021/cr0503658.

(60) Elliott, W. C.; Gardner, D. J.; Malla, P.; Riley, E. A New Look at the Occurrences of the Rare-Earth Elements in the Georgia Kaolins. *Clays Clay Miner.* **2018**, *66* (3), 245–260. https://doi.org/10.1346/CCMN.2018.064096.

(61) Ehlmann, B. L.; Mustard, J. F.; Murchie, S. L.; Bibring, J.-P.; Meunier, A.; Fraeman, A. A.; Langevin, Y. Subsurface Water and Clay Mineral Formation during the Early History of Mars. *Nature* **2011**, *479* (7371), 53–60. https://doi.org/10.1038/nature10582.

(62) Bishop, J. L.; Fairén, A. G.; Michalski, J. R.; Gago-Duport, L.; Baker, L. L.; Velbel, M. A.; Gross, C.; Rampe, E. B. Surface Clay Formation during Short-Term Warmer and Wetter Conditions on a Largely Cold Ancient Mars. *Nat. Astron.* **2018**, *2* (3), 206–213. https://doi.org/10.1038/s41550-017-0377-9.

**Supporting Information for Chapter 3**

Table 1: Trace elements mean concentrations (ppm) of Fe-rich smectite and their standard deviation (SD) values

| Element | Unreacted SWa-1 | SD | SWa-1_8hrs | SD | SWa-1_120 hrs | SD | SWa-1_ 504 hrs | SD |
|---|---|---|---|---|---|---|---|---|
| Ba | 34.35 | 12.25 | 560.00 | 2.00 | 3005.00 | 5.00 | 3645.00 | 5.00 |
| Co | 18.00 | 3.00 | 14.00 | 1.00 | 7.50 | 0.50 | 12.00 | 0.00 |
| Cr | 18.50 | 0.50 | 16.50 | 0.50 | 15.50 | 0.50 | 22.00 | 3.00 |
| Cs | 0.62 | 0.01 | 0.67 | 0.02 | 1.15 | 0.03 | 1.96 | 0.04 |
| Cu | 11.00 | 0.00 | 55.00 | 8.00 | 8.00 | 0.00 | 12.00 | 0.00 |
| Ga | 8.70 | 0.00 | 8.10 | 0.10 | 8.35 | 0.15 | 10.15 | 0.25 |
| Hf | 3.04 | 0.09 | 2.74 | 0.02 | 2.90 | 0.05 | 4.76 | 0.19 |
| Li | 10.00 | 0.00 | 20.00 | 0.00 | 20.00 | 0.00 | 10.00 | 0.00 |
| Nb | 4.29 | 0.15 | 3.78 | 0.02 | 3.76 | 0.05 | 5.35 | 0.24 |
| Ni | 7.50 | 0.50 | 5.50 | 0.50 | 4.00 | 1.00 | 6.50 | 0.50 |
| Pb | 7.50 | 0.50 | 13.50 | 0.50 | 3.00 | 0.00 | 7.50 | 0.50 |
| Rb | 2.60 | 0.20 | 4.40 | 0.00 | 9.30 | 0.10 | 20.20 | 0.20 |
| Sn | 1.25 | 0.25 | 2.40 | 0.20 | 0.85 | 0.05 | 1.30 | 0.10 |
| Sr | 76.35 | 1.05 | 286.50 | 0.50 | 635.00 | 6.00 | 549.50 | 4.50 |
| Ta | 0.20 | 0.00 | 0.20 | 0.00 | 0.20 | 0.00 | 0.30 | 0.00 |
| Th | 2.04 | 0.05 | 1.89 | 0.01 | 1.84 | 0.01 | 2.69 | 0.10 |
| Ti | 0.29 | 0.01 | 0.27 | 0.01 | 0.26 | 0.00 | 0.30 | 0.01 |
| U | 0.72 | 0.01 | 0.48 | 0.02 | 0.48 | 0.01 | 0.76 | 0.02 |
| V | 499.00 | 1.00 | 377.00 | 1.00 | 396.50 | 4.50 | 364.50 | 7.50 |
| W | 0.95 | 0.35 | 0.95 | 0.05 | 0.65 | 0.15 | 1.10 | 0.00 |
| Zn | 85.50 | 0.50 | 90.50 | 2.50 | 81.50 | 0.50 | 82.50 | 0.50 |
| Zr | 126.50 | 0.5.0 | 109.00 | 1.00 | 109.00 | 1.00 | 187.00 | 2.00 |

Table 2: Trace elements mean concentrations (ppm) of Al-rich smectite and their standard deviation (SD) values.

| Element | Unreacted SAz-1 | SD | SAz-1_8hrs | SD | SAz-1_120 hrs | SD | SAz-1_504 hrs | SD |
|---|---|---|---|---|---|---|---|---|
| Ba | 291.00 | 8.00 | 837.00 | 6.00 | 1905.00 | 15.00 | 1575.00 | 10.00 |
| Co | 1.00 | 0.00 | 1.00 | 0.00 | 1.00 | 0.00 | 1.00 | 0.00 |
| Cr | 7.00 | 1.00 | 7.00 | 0.00 | 9.00 | 0.00 | 7.00 | 1.00 |
| Cs | 0.67 | 0.02 | 0.76 | 0.02 | 1.21 | 0.01 | 1.54 | 0.04 |
| Cu | 11.50 | 1.50 | 5.50 | 0.50 | 2.50 | 0.50 | 108.50 | 3.50 |
| Ga | 18.75 | 0.45 | 18.95 | 0.45 | 19.95 | 0.45 | 17.55 | 0.05 |
| Hf | 7.14 | 0.14 | 7.32 | 0.10 | 7.50 | 0.10 | 7.03 | 0.08 |
| Li | 220.00 | 0.00 | 230.00 | 0.00 | 240.00 | 0.00 | 210.00 | 0.00 |
| Nb | 21.65 | 0.45 | 21.45 | 0.35 | 21.45 | 0.15 | 19.10 | 0.60 |
| Ni | 2.50 | 0.50 | 3.00 | 0.00 | 2.00 | 0.00 | 2.50 | 0.50 |
| Pb | 28.00 | 1.00 | 27.50 | 0.50 | 26.50 | 0.50 | 32.50 | 0.50 |
| Rb | 5.60 | 0.30 | 8.15 | 0.25 | 10.40 | 0.10 | 11.60 | 0.20 |
| Sn | 2.60 | 0.20 | 2.75 | 0.15 | 2.95 | 0.05 | 9.90 | 3.80 |
| Sr | 285.50 | 9.50 | 508.50 | 2.50 | 707.50 | 2.50 | 526.00 | 8.00 |
| Ta | 1.30 | 0.10 | 1.35 | 0.05 | 1.45 | 0.05 | 1.30 | 0.10 |
| Th | 24.05 | 0.85 | 24.20 | 0.30 | 25.50 | 0.20 | 22.10 | 0.50 |
| Ti | 0.12 | 0.00 | 0.13 | 0.01 | 0.13 | 0.00 | 0.12 | 0.00 |
| U | 1.70 | 0.10 | 1.66 | 0.04 | 1.74 | 0.04 | 1.42 | 0.00 |
| V | 67.50 | 2.50 | 68.50 | 1.50 | 71.00 | 0.00 | 60.00 | 2.00 |
| W | 1.00 | 0.00 | 0.90 | 0.10 | 0.90 | 0.20 | 0.95 | 0.25 |
| Zn | 56.50 | 0.50 | 54.00 | 0.00 | 56.00 | 1.00 | 69.50 | 3.50 |
| Zr | 264.00 | 4.00 | 265.50 | 3.50 | 271.50 | 0.50 | 260.00 | 8.00 |

Table 3: Rare earth elements mean concentrations (ppm) of Fe-rich smectite and their standard deviation (SD) values.

| Element | Unreacted SWa-1 | SD | SWa-1_8hrs | SD | SWa-1_120 hrs | SD | SWa-1_504 hrs | SD |
|---|---|---|---|---|---|---|---|---|
| Ce | 43.05 | 2.05 | 36.75 | 0.75 | 38.35 | 0.25 | 41.85 | 0.25 |
| Dy | 4.04 | 0.05 | 3.63 | 0.06 | 3.55 | 0.10 | 4.53 | 0.02 |
| Er | 1.99 | 0.04 | 2.06 | 0.02 | 1.83 | 0.07 | 2.72 | 0.03 |
| Eu | 1.45 | 0.07 | 1.72 | 0.03 | 1.57 | 0.11 | 2.11 | 0.07 |
| Gd | 5.17 | 0.06 | 4.83 | 0.11 | 4.10 | 0.06 | 5.57 | 0.04 |
| Ho | 0.85 | 0.02 | 1.11 | 0.06 | 0.90 | 0.10 | 1.53 | 0.04 |
| La | 20.20 | 0.20 | 17.85 | 0.15 | 18.70 | 0.10 | 20.90 | 0.40 |
| Lu | 0.40 | 0.01 | 0.70 | 0.10 | 0.48 | 0.06 | 1.10 | 0.10 |
| Nd | 27.65 | 0.25 | 23.65 | 0.35 | 25.15 | 0.05 | 26.85 | 0.45 |
| Pr | 6.01 | 0.07 | 5.64 | 0.00 | 5.73 | 0.05 | 6.72 | 0.14 |
| Sc | 25.85 | 0.05 | 24.60 | 0.40 | 22.75 | 0.45 | 23.25 | 0.15 |
| Sm | 6.24 | 0.06 | 5.87 | 0.03 | 5.85 | 0.01 | 6.53 | 0.04 |
| Tb | 0.85 | 0.04 | 1.12 | 0.05 | 0.10 | 0.10 | 1.53 | 0.08 |
| Tm | 0.43 | 0.01 | 0.74 | 0.08 | 0.51 | 0.06 | 1.13 | 0.07 |
| Y | 16.25 | 0.45 | 13.10 | 0.10 | 13.75 | 0.25 | 16.60 | 0.20 |
| Yb | 1.95 | 0.08 | 1.89 | 0.06 | 1.69 | 0.06 | 2.64 | 0.06 |

Table 4: Rare earth elements mean concentrations (ppm) of Al-rich smectite and their standard deviation (SD) values.

| Element | Unreacted SAz-1 | SD | SAz-1_8hrs | SD | SAz-1_120 hrs | SD | SAz-1_504 hrs | SD |
|---|---|---|---|---|---|---|---|---|
| Ce | 138.75 | 5.75 | 136.25 | 2.75 | 145.50 | 0.00 | 120.75 | 2.75 |
| Dy | 4.97 | 0.23 | 5.02 | 0.00 | 5.45 | 0.14 | 4.57 | 0.05 |
| Er | 2.97 | 0.16 | 2.89 | 0.04 | 3.08 | 0.06 | 2.72 | 0.15 |
| Eu | 0.93 | 0.05 | 0.10 | 0.05 | 1.03 | 0.01 | 0.93 | 0.00 |
| Gd | 5.83 | 0.26 | 6.11 | 0.08 | 6.23 | 0.04 | 5.43 | 0.10 |
| Ho | 0.10 | 0.06 | 1.02 | 0.03 | 1.07 | 0.03 | 0.90 | 0.02 |
| La | 71.80 | 1.70 | 72.05 | 0.95 | 74.75 | 0.65 | 67.10 | 1.40 |
| Lu | 0.39 | 0.00 | 0.44 | 0.02 | 0.45 | 0.03 | 0.42 | 0.02 |
| Nd | 50.65 | 1.15 | 50.70 | 0.50 | 53.90 | 0.10 | 46.75 | 0.65 |
| Pr | 14.10 | 0.30 | 14.25 | 0.25 | 14.68 | 0.13 | 12.95 | 0.25 |
| Sc | 4.35 | 0.05 | 4.05 | 0.45 | 3.55 | 0.05 | 3.65 | 0.15 |
| Sm | 8.39 | 0.56 | 8.46 | 0.24 | 8.93 | 0.27 | 7.77 | 0.02 |
| Tb | 0.88 | 0.07 | 0.88 | 0.02 | 0.92 | 0.03 | 0.82 | 0.06 |
| Tm | 0.44 | 0.04 | 0.44 | 0.03 | 0.47 | 0.01 | 0.38 | 0.01 |
| Y | 27.35 | 1.25 | 28.40 | 0.40 | 30.45 | 0.25 | 25.10 | 0.50 |
| Yb | 2.81 | 0.13 | 2.80 | 0.11 | 3.01 | 0.10 | 2.65 | 0.06 |

## Dissertation Conclusions

This dissertation explores mineral reactivity in bulk and nanoscale phase in a modern euxinic spring. In chapter 1, the study of euxinic spring-impacted sediments shows that bulk sulfate and sulfide minerals can form and coexist in a modern euxinic environment, whether the fluid is in direct contact with the atmosphere or not. Furthermore, euxinic conditions do not change the clay mineralogy of sediments, whether at the surface in contact with the atmosphere, on the time scale of tens of thousands of years or at depth without direct contact with the atmosphere. Finally, Al-rich smectites responds to a modern euxinic condition by interlayer cation exchange with no influence on its morphology and immobilization of nanoprecipitates which reflect the chemistry of the surrounding aqueous solution. This implies that, Al-rich smectites would have responded to the widespread euxinia during the Proterozoic on early earth by cation exchange in their interlayer and by adsorption of available trace elements as sulfur minerals on their surface. However, the octahedral chemical compositions of smectite would have remained unchanged during ancient euxinic periods on Earth and possibly during the paleo-sulfidic period on Mars for 10's of thousands of years.

Chapter 2 detailed the morphological and color changes in Fe-rich smectite versus Al-rich smectite over a period of 504 hours of reaction with a modern euxinic spring. The progressive reductive dissolution of Fe-rich smectite shows that Fe-rich clay mineral would have been unstable on the early earth. Also, the dissolution was accompanied by color and morphological changes in the Fe-rich smectite. The precipitation Fe-S mineral phases as reductive dissolution progresses means, smectite edges would have served as nucleation sites for Fe-S minerals and pyrite would have been a sink for Fe and S on the early earth. Also, Fe-rich clay-sulfide reactions could have altered

Martian clay stability, explaining the partial dissolution/transformation of smectites observed by rover missions.

Chapter 3 focuses on trace element mobility in the presence of differing smectite octahedral sheet composition in a modern euxinic environment. Our result shows that reduced Fe-rich clay minerals may have acted as both temporary sinks and sources of trace elements including REEs. While this has a positive impact on trace element mining, it thus has a negative impact on biological communities who needs bio-essential metals (e.g., Cu, Zn) for survival. Also, the observed trend of multivalence trace elements (Cr, Ga, Hf, Nb, Ta, Th, Ti, U, W, and Zr) replacing divalent trace elements (Cu, Pb and Zn) in reduced Fe-rich smectite after some hours in this terrestrial euxinic spring could be an indication to redox gradients and a sign of potential habitability in Martian clay strata. However, the reverse trend observed in SAz-1 where Cu, Pb, and Zn are immobilized with longer exposure to euxinic condition could suggests that Al-rich smectites on the early earth and Mars may have sequestered bio-essential metals, possibly influencing nutrient availability for any potential microbial life.

In conclusion, this dissertation has added to our understanding of nanoscale mineral chemistry in a modern euxinic-oxic system, especially smectite clay reactivity, with potential applications in metal remediation and mining processes, understanding geochemical cycles on early Earth and habitability on Mars.